MODELLING FATIGUE CRACK PROPAGATION IN COPED BEAMS USING XFEM

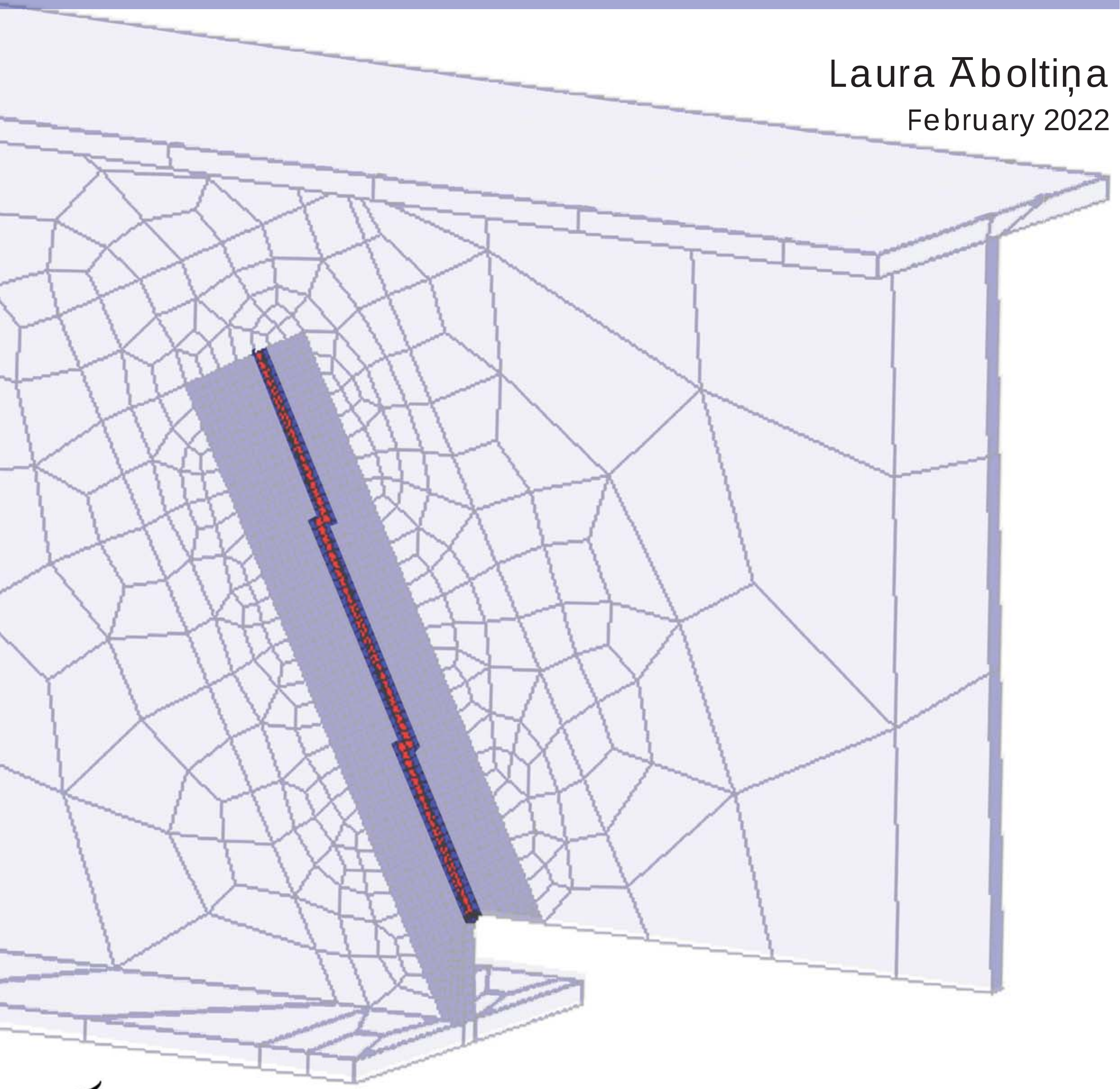

Laura Āboltiņa

February 2022

Modelling fatigue crack propagation in coped beams using XFEM

by

Laura Āboltiņa

to obtain the degree of Master of Science

at the Delft University of Technology,

Student number:	5163870	
Project duration:	April, 2021 – March, 2022	
Thesis committee:	Dr.ir. Marko Pavlović	TU Delft, Chair
	Dr.ir. Frans van der Meer	TU Delft
	Ir. David Malschaert	TU Delft, Daily supervisor
	Ir. Weikang Feng	TU Delft
	Prof.dr.ir. Johan Maljaars	TNO
	Ir. Stefan Verdenius	TNO, Daily supervisor

Preface

This report is the last chapter of my student life at the faculty of Civil Engineering at Delft University of Technology. It concludes an exciting journey that has undoubtedly been very difficult. However, it has also allowed me to grow both professionally as well as personally. I am proud of what has been achieved and feel encouraged to take up new challenges further in the future.

This achievement, however, is not only mine. I am extremely grateful for those people that have been around me through this journey. As Helen Keller has said:

"Alone we can do so little; together we can do so much." /Helen Keller/

Therefore, I have to give credit where it's due. And a large part of it goes to my graduation committee that has been composed of TU Delft and TNO personnel. I want to thank the chair of the committee Marko Pavlovic for setting a great example of what an excellent supervisor should be. To Frans van der Mee and Johan Maljaar for sharing all their knowledge and experiences with me. To Weikang Feng for keeping an eye on my progress. And special gratitude goes to my daily supervisors David Malschaert and Stefan Verdenius. I admire the passion you put into the work, I appreciate all brainstorms we have had, and truly thank you for guiding me through this process. I could not wish for better daily supervisors!

My dear friends, it is impossible to name you all in this chapter, but please know that each of you has been a crucial part of my life during these two and a half years. Do not underestimate a simple conversation in the corridors, the support that is given by just sitting and studying next to me, the endless hours that I have had with you on the phone, and just a simple dinner or a workout together to take my mind somewhere else. This all has led me to today and you all have a special place in my heart for that. I also know that the friendships created and sustained here will last very long.

Last, but definitely not lease. My family. My sisters, Ilze and Diāna, and my parents, Laila and Guntars. Without you, my graduation would have been just an unfulfilled dream. I'm beyond grateful for your pure love and unlimited support. You have thought me to work hard, do what I love and never give up. Thank you for always believing in me!

It is now time to close this chapter and, with excitement, look to the future. Thank you TU Delft, it has been an adventure!

Laura Āboltiņa
Delft, March 2022

Summary

In the past years, the safety of steel railway bridges has been questioned due to the coped beam connection sensitivity to fatigue and fatigue crack appearance. To ensure the safety of these railway bridges, the propagation of the fatigue crack needs to be analysed by performing regular inspection on the bridges. The frequency of these is required by the defined inspection intervals, which are based on the critical crack length and the number of loading cycles leading to this crack length. Laboratory tests and measurements on the bridges have been performed in the past to define inspection intervals, but had given only an approximation of the real situation. By creating a finite element model of a coped beam, a crack initiation and propagation analysis can be performed. This analysis provides an indication after how many loading cycles the crack will reach a critical length and guides towards revised inspection intervals.

In this thesis, the objective is to take the first steps towards the revised inspection interval by performing a finite element analysis of the crack propagation of steel railway bridges. More specifically, this means an finite element analysis of the coped beam with extended finite element method.

To achieve this goal, first, the location of the fatigue crack initiation has been investigated to understand where exactly in the cope the crack starts. This was performed by creating a local 3D linear elastic FE-model of the coped beam based on the boundary conditions, geometry, and loading from laboratory tests performed by Michael C.H. Yam and J.J. Roger Cheng. The the longitudinal stresses of the model were compared with stresses measured during the laboratory test to validate the crack initiation model. After the model was validated, the location of crack initiation was determined by identifying the location of the peak stresses.

After completion of the crack initiation analysis, the crack propagation analysis can commence. For this, the FE-model was transformed from the crack initiation to the crack propagation model. In the same manner as with the crack initiation model, the propagation model has been based on the boundary conditions, geometry, and loading from the laboratory test. Since no path of the crack was registered during these laboratory tests, and thus could not be implemented in the model, a method for crack propagation analysis called extended finite element method (XFEM) has been used. The accuracy of this method has been confirmed by validating the stress intensity factor (SIF) values obtained for stationary cracks with three different mesh topologies and comparing the results with results from two established methods; J-integral and VCCT.

After the validation of the crack propagation model, a sensitivity study was performed to understand the potential influence of modelling decisions on the number of load cycles versus crack length relation. With the mesh sensitivity analysis, a linear trend has been obtained for models with matching number of elements through the thickness. For the initial crack size sensitivity analysis, the effect of the number of elements through the thickness and the effect of mesh topology have been investigated. One element through the thickness and parallel mesh topology led to lower variation in the results.

Additionally, a new value for the previously assumed Paris law coefficient C has been obtained by calibrating the number of cycles versus the crack length curve from FE-model to match the laboratory test results.

In conclusion, this research provides recommendations for modelling crack propagation in a coped beam. The results are more reliable when keeping at least five finely meshed elements around the crack tip, using a parallel mesh topology, and using one element through the thickness. New value for the C coefficient from the Paris law has been suggested based on this research.

The next step in this research is a continuation of the crack propagation model analysis to reduce the variation in the results. Furthermore, different loading positions and expansion from a simply supported beam model to a model with multiple spans should be analysed to bring us one step closer to the ultimate goal of redefining the inspection interval for coped beam steel bridges based on the models.

Contents

1

Introduction

1.1. Problem Background

For a long time, steel structures have been designed without the knowledge of the fatigue limit state [46]. Fatigue was first mentioned in 1837 when the first fatigue test was performed by W. A. J. Albert [54]. Till then, the calculations only ensured that the applied load did not exceed the material yield stress limit. However, for some of the structures, cracks were detected when subjected to loads that were way below the load limit that they were designed for [27, 51]. In Canada, the United States, and Japan, even a full collapse of bridges has occurred due to fatigue cracks [18]. The described weakness introduction in the steel material by repeated loading that can lead to a fracture even under the allowed stress level is called steel fatigue [63].

When a structure is subjected to cyclic tensile stresses, microcracks can initiate and grow, resulting in a failure due to fatigue. These microcracks can also already be in the material due to the material flaws and due to the manufacturing processes.

Typical structures that are subjected to fatigue problems are bridges. The cars, trucks, and/or trains that pass the bridge every day cause the previously mentioned cyclic loading. Some parts of the bridge are sensitive to these stress ranges and that lead to fatigue problems.

As many research papers indicate [27, 35, 44, 67], coped beams, that can be seen in figure 1.1, are susceptible to fatigue damage. The cope in the beam creates a geometrical discontinuity that results in a high stress concentration in the web at the rounding of the cope. Moreover, the strength and torsional stiffness are reduced at the ends of coped beams [52].

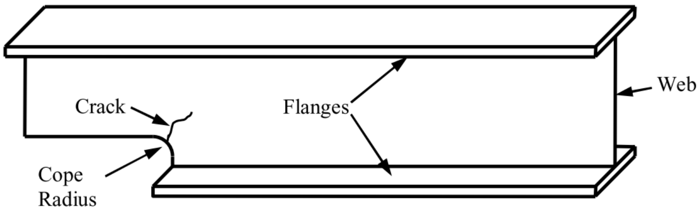

Figure 1.1: Coped beam [27].

In the past, beams needed to be coped to provide enough clearance for the connections. An example of such a connection is when two perpendicular beams with an I-shape cross-section are at the same elevation and need to be connected, as can be seen in figure 1.2. Then the flanges of one of the beams need to be cut away. In bridges, the ends of longitudinal beams are coped to connect them to the cross-beams. Nowadays, engineers are aware of the fatigue damage issue when using coped beams. Therefore, connections, like shown in figure 1.2, are not being used anymore.

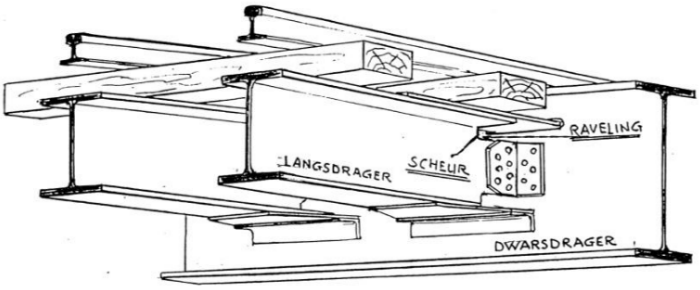

Figure 1.2: Coped beam connection [37] with notes in Dutch:
langsdrager - longitudinal beam
dwarsdrager - cross-beam
scheur - tear/ crack
raveling - coped part.

However, such a connection was often used in railway bridges in the past. These bridges are still functioning today, and to ensure the structural safety of the coped beam connection with respect to the fatigue life, inspections on the bridges are being performed. During these inspections, new cracks are being registered and existing crack lengths are measured and compared to earlier inspections. The size and location of the cracks determines the predicted remaining fatigue life.

Recurrence of inspection is based on the fatigue life estimation, which indicates after how many loading cycles a certain length of the crack should be obtained. By knowing the intensity of the traffic, inspections can be planned and the possible increase of crack length can be measured. Conservative results of the fatigue life estimation can lead to an insufficient number of inspections and introduce the risk of collapse of the bridge. Therefore, it is important to find an effective and reliable method for determining the fatigue life, and hence the inspection interval, of such a connection. However, too much inspection is also undesired due to time, costs, and traffic disturbance.

1.2. Research Question

In the 1980s and 1990s, a fatigue crack propagation analysis in the coped zone has been performed. Tests in laboratories were done by ProRail [37], Washington State Department of Transportation [51] and as a research for a Masters' thesis by Michael C. H. Yam [65, 66]. The simplified tests done in the laboratory gave only an approximation of the real situation on the bridge. ProRail also analysed measurements done on the existing railway bridges [37]. However, the test results from the coped zones differ strongly between measurements, as is explained in section 2.3, and additionally the data registered from the tests is incomplete.

In this thesis, the crack propagation in a coped beam connection has been analysed by performing a finite element analysis to take the first steps towards the goal of obtaining the inspection intervals of the coped beam connection. This particular research focused on the possibility of creating a finite element model for such a connection without the need of additional information, such as the crack path. The path is usually derived from the laboratory test, but since these are time consuming and expensive, an alternative way of determining the crack path is desired. To this end, the numerical technique within the FE-model called XFEM has been used, where the crack path can be unknown. The main question that has been answered is:

How to accurately model fatigue crack propagation for railway bridges with coped beam connections?

The process of answering the main research question has been divided into three sub-questions that have been answered subsequently. First, the location of the crack initiation has been found.

Sub-q. 1: *What is the location of the fatigue crack initiation?*

At this location, an initial crack has been modelled by transforming the initiation model into the propagation model. By making this transition, the most influencing factors for a crack propagation model in XFEM have been investigated, allowing to answer sub-q 2:

Sub-q. 2: *Which parameters dominate the crack propagation in Abaqus when using the XFEM method?*

And finally, sub-question 3 was answered by running analysis of the crack propagation model and obtaining the necessary relation between the crack length and the number of load cycles.

Sub-q. 3: *What is the relationship between the crack length and the accumulated number of loading cycles?*

A more in-depth explanation of each question is given in the following section, where the methodology and stepwise approach have been explained.

1.3. Methodology

This research has been based on the information that can be found in the literature in combination with the use of a commercial software called Abaqus. A literature review is presented to gather the necessary background information and observe already existing knowledge on the topic. Research paper containing laboratory test results has been used to validate the results obtained by the software for sub-question 1 and to calibrate the results for sub-question 3.

As stated in section 1.2, the main research question has been answered by subsequently answering the sub-questions. The flowchart in figure 1.3 schematically shows the steps taken to achieve the answer.

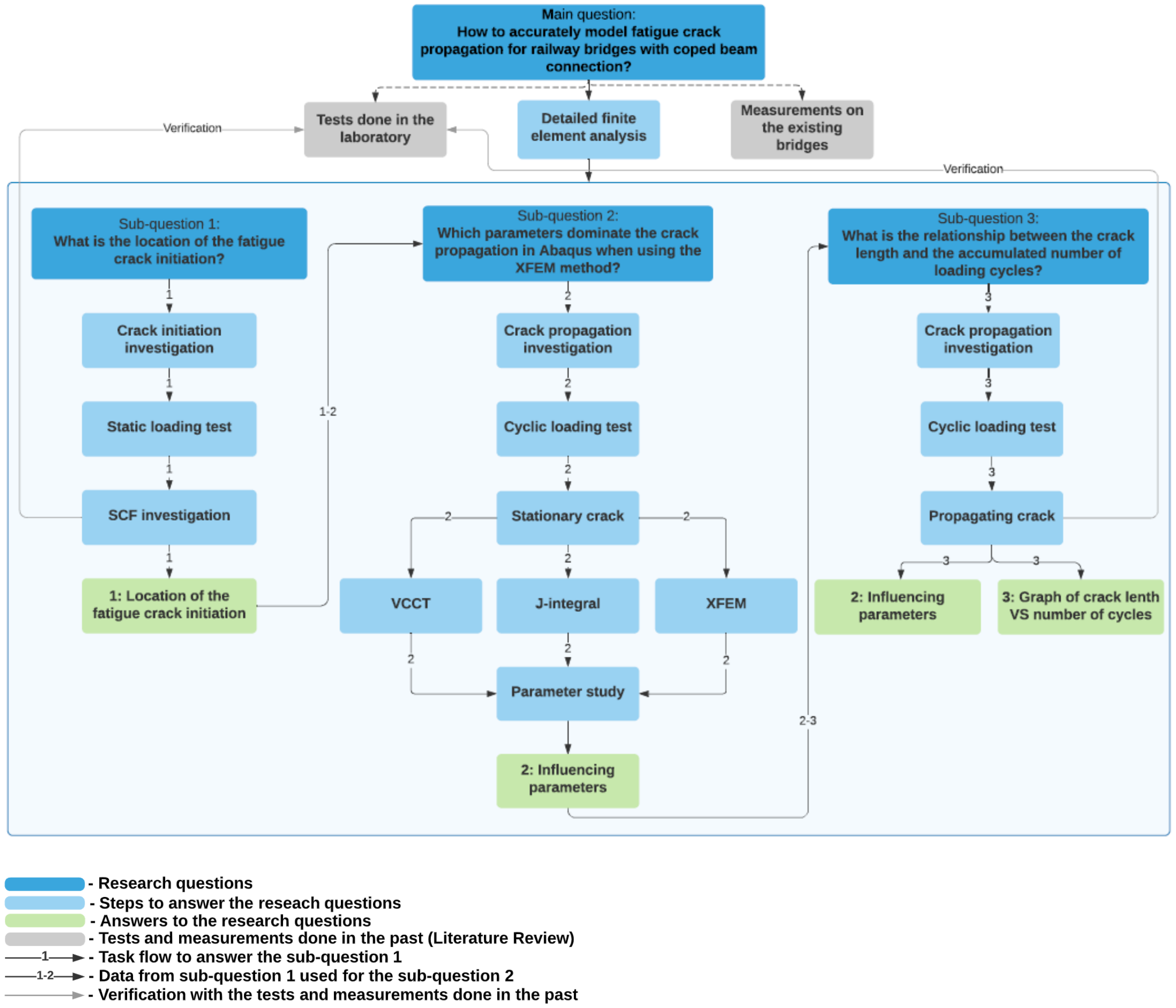

Figure 1.3: Flowchart to answer the main research question.

1.3.1. Research Sub-question 1

Before going into the fatigue crack propagation phase, it was necessary to determine the location of the crack initiation. Therefore, the first question that needed to be answered was:

Sub-question 1: *What is the location of the fatigue crack initiation?*

A 3D linear elastic FE-model of a simply supported, statically loaded beam has been made by using the computer software Abaqus. The boundary conditions, geometry and loading have been replicated from the laboratory test [67] to be able to validate the results. The laboratory test setup is described in section 3.1.

Validation of the model has been done by comparing the longitudinal stresses obtained from the FE-model with the values registered during the laboratory tests.

The location of the fatigue crack has been found by reading the results of the stresses on the curve of the cope from the FE-model. The location of the peak stresses indicates where on the curve the crack will initiate. This gives the answer to sub-question 1.

1.3.2. Research Sub-question 2

Constructing a successful propagation model has turned out to be dependent on certain parameters, such as the mesh of the model. To obtain a reliable propagation model, sensitivity analysis on the parameters has been performed and the influence of each of them has been discussed when answering the sub-question 2.

Sub-question 2: *Which parameters dominate the crack propagation in Abaqus when using the XFEM method?*

The fatigue crack initiation and propagation stage have very different characteristics, as is described in sections 2.2.1 and 2.2.2. Therefore, the transition from a FE-model where the crack initiation has been analysed for sub-question 1 to an XFEM model that allows to perform crack propagation simulation for sub-question 3 involved significant changes in the model. Some of these changes had a distinctive influence on the results, which have been described in detail in chapter 4.

To answer sub-question 2, the FE-model of a simply supported, statically loaded beam from sub-question 1 has been used and further adjusted. An initial crack has been implemented at the location found in sub-question 1 and cyclic loading has been applied.

Crack propagation has been then modelled by using the extended finite element method (XFEM). Herewith, a crack path has been obtained through numerical analysis by use of the enriched displacement-based approximation, see section 2.4.

Crack propagation is mainly dependent on the stress intensity factor (SIF). Therefore, to verify the results from XFEM and to indicate more influencing factors in the model, two well-known and reliable methods, J-integral and VCCT, briefly described in section 2.2.3 and 2.4.1, have been additionally used. With all three methods, stationary cracks of the same length have been modelled and the stress intensity factors at the tip of the crack have been compared.

Additionally, the sensitivity analysis has been performed to spot the inconsistencies in the results and to determine more influencing parameters to take into consideration when modelling a crack propagation model.

1.3.3. Research Sub-question 3

Sub-question 3: *What is the relationship between the crack length and the accumulated number of loading cycles?*

Sub-question 2 has provided a model that can perform a crack propagation analysis. From this model, a graph with crack length dependency on the number of load cycles has been obtained.

A comparison has been made between the numerical results from the XFEM analysis and the experimental results from the laboratory tests. The constants from the Paris law, i.e., C and m, see section 2.1.2, have been calibrated by using the experimental results from the laboratory tests. More information regarding the laboratory tests done in the past with cyclic loading can be found in section 4.1. Sub-question 3 has been answered with the calibrated FE-model. This model is an accurate tool to model fatigue crack propagation in a coped beam as it occurs in railway bridges, therefore, it answers the main research question.

1.4. Structure of the Report

Chapter 2 provides the necessary knowledge obtained by the literature review. It explains the relevance of this research by spotting the gaps in the literature. It provides theoretical knowledge for the reader to be able to follow and understand the progression of this research.

Chapter 3 contains information on the crack initiation under the effect of static loading. In section 3.1 laboratory tests done in the past are presented. Then the FE-model developed to reconstruct these tests is described. Finally, the comparison of the results of the FE-model and the laboratory tests is being discussed.

In chapter 4, similar to chapter 3, the details about the laboratory tests are first introduced, but this time for the crack propagation under the effect of cyclic loading. Then the modelling process in Abaqus is explained and the results presented.

Chapter 5 and 6 finalizes the paper by presenting conclusions, discussion and recommendations, respectively.

2

Literature Review

This chapter gathers information found in the literature that is relevant for this research. Each of the sections is referred to a certain part of the flowchart presented in figure 1.3 to create a clear transition from the literature towards this research.

Firstly, section 2.1 introduces the theory behind the fatigue cracks by presenting the fatigue life stages and the influencing parameters. Then, section 2.2 introduces the theory of Linear Elastic Fracture mechanics, which is the basic theory of fracture. These two sections are relevant for all parts of the flowchart.

Section 2.3 tells about the attempts to solve coped beam fatigue problems by analysing measurements on bridges and tests in the laboratory. It also indicates why the obtained results from these measurements and tests can be only used as an approximation. This section represents the two grey boxes in the flowchart in figure 1.3 and reasons why the third approach with detailed finite element analysis needs to be performed.

Lastly, section 2.4 explains an approach within the finite element software that allows to model crack propagation with no information about the crack path. This section refers to the sub-question 2 and 3 in the flowchart when the crack propagation has been modelled.

2.1. Fatigue cracks

The term fatigue comes from the Latin word ”fatīgāre” which in translation means ”to weary, to tire” [59]. Most of the time this term is associated with a physical and mental feeling of tiredness. In the engineering vocabulary, however, it describes a degradation mechanism in the material due to the cyclic loading and becomes visible in the form of cracks [46]. Even very small stress cycle from repeated loading or vibrations causes an incremental growth of the crack [60]. Fatigue crack growth can lead to a complete failure of the structure at the end of fatigue life called fracture [20]. Therefore, it is important to predict the number of load cycles that a structure can withstand before the fatigue life is reached.

It is important to distinguish two different periods in the fatigue life of a crack, which are crack initiation and crack propagation [22]. First, the crack initiation occurs. This phase has been investigated when answering the sub-question 1 and refers to the crack initiation investigation box in figure 1.3. In this stage, the crack growth has a slow pace. Crack initiation is based on the cyclic slip mechanism, explained in detail in section 2.1.1. When the crack grows further into the material, the cyclic slip is restrained by the surrounding material. The crack growth mechanism changes and the second period of the fatigue life begins, which is called crack propagation or crack growth and is introduced in section 2.1.2. Crack propagation is characterized by an increasing crack growth rate. Crack propagation investigation has been performed to answer sub-question 2 and 3, see figure 1.3. This period ends when the crack has grown such that fracture toughness has been reached and a brittle failure due to the fracture occurs [53], see section 2.1.3.

Figure 2.1 illustrates the fatigue life periods within a schematic graph of the crack length over time. This figure is a schematic presentation of the fatigue life since the crack length can increase or stay constant and the propagation rate can increase, stay constant, and even decrease depending on the detail.

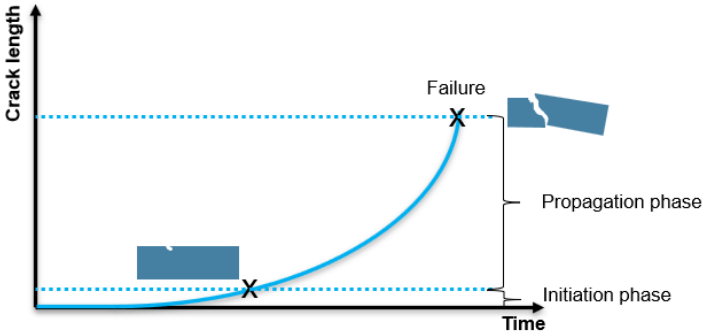

Figure 2.1: Fatigue life periods within a schematic graph of crack length dependency of the time.

The periods, also called phases, must be considered separately [54] because they depend on different properties, and additionally some properties have different effects on each of the periods [53]. For example, the crack initiation depends on the surface conditions like roughness [19], but the crack propagation depends on the material properties [28]. However, a corrosive environment will affect both periods but with a different magnitude of the effect [53]. Crack initiation is related to the stress concentration factor K_t, crack propagation to the stress intensity factor K, and the final failure is related to the fracture toughness K_{Ic}. Fracture and failure are used as synonyms in the remainder of the text. Figure 2.2 shows the fatigue life periods and the corresponding coefficients.

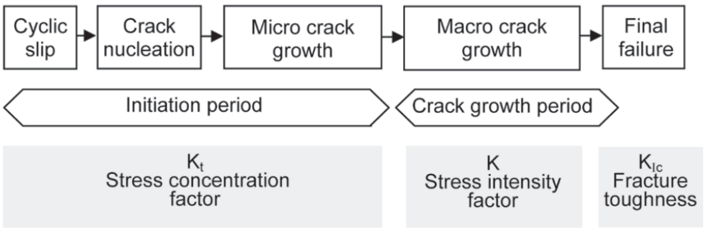

Figure 2.2: Periods of the fatigue life [53].

2.1.1. Crack initiation phase

In the material subjected to cyclic loading, a small number of grains are subjected to plastic deformation [53]. These are usually the grains that are located close to the surface and are restrained by the rest of the material only from one side. This plastic deformation phenomenon is called cyclic slip and occurs when the cyclic shear stress amplitude is lower than the yield stress of the material. The result of a cyclic slip is a slip step that can initiate a microcrack in the surface of the material. Other causes for crack initiation are surface roughness, damage and treatment, environmental effects like corrosion pits, etc. It is important to understand that the fatigue problem most of the time starts at the surface of the material and depends on the surface conditions.

The initiation stage can take a long time if there are no surface flaws in the material or a short time if there are already flaws present. This difference in initiation time exists because the surface flaws are geometric discontinuities that increase the stress value in the material. To obtain the actual maximum stress value σ_{max} at the discontinuity, the nominal stress σ_{nom} needs to be multiplied with the stress concentration factor (SCF) K_t, as can be seen in equation 2.1 [47] .

$$\sigma_{max} = K_t \sigma_{nom} \tag{2.1}$$

Different types of discontinuities have their own stress concentration factors. Some values are well known based on previous experiments and are reported in literature [58]. Other SCFs can be obtained by laboratory tests, measurements, or FE-model. An example of a discontinuity increasing the stress in the material, is the cope at the end of the beam considered in this thesis. FE-model has been used in sub-question 1 to obtain the maximum stress values along the cope of the beam to find the location of the crack initiation.

2.1.2. Crack propagation phase

When the crack continues to propagate further in the structure, more material will surround the crack tip and prevent the possibility of a cyclic slip in the original direction. The crack will change its direction to the one perpendicular to the applied loading and will continue propagating throughout the material. That is because the crack growth now is no longer dependent on the surface conditions, but depends on the material properties around the crack tip [53].

To define the crack growth rate in sub-question 2 and 3, the Paris law has been used, see equation 2.2 [26]. a is the crack length in mm, N the number of cycles, ΔK is the stress intensity factor in $MPa\, m^{-1/2}$, and C and m are empirical coefficients that are found experimentally [51]. Recommended values for coefficients C and m for common steels, aluminium, titanium and other metals are given in the British standard [57]. The Paris law assumes elastic crack growth even though minor yielding always occurs at the crack tip.

$$\frac{da}{dN} = C(\Delta K)^m \tag{2.2}$$

Figure 2.3 shows the relation between the crack growth and the stress intensity factor on a logarithmic scale. The previously described Paris law holds only for region II where the growth is linearly dependent on the stress intensity factor range on a log-log scale and is called the Paris region. If region I or III needs to be included in the analysis, there are additional formulas available in literature [2]. Region I describes a quick increase in the crack growth once the threshold stress intensity factor range ΔK_{th} is reached. Below this value, no crack growth occurs. Region III shows a steep increase in the crack growth as well, that will lead to the fracture of the material once the stress intensity factor reaches the critical stress intensity factor value of K_c [37].

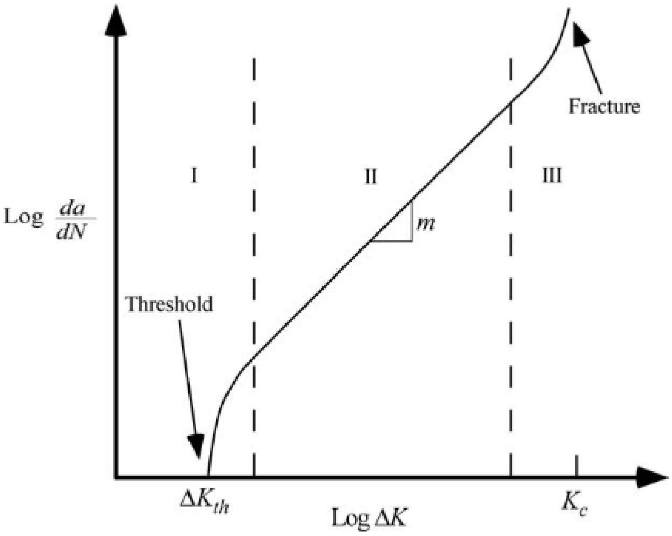

Figure 2.3: Crack growth representation on a logarithmic scale [2].

2.1.3. Failure due to fracture

The fatigue life of a material has been reached when the crack has weakened the structure so far that the fracture of the material occurs [20]. It happens when the stress intensity factor has grown to the level of critical stress intensity factor K_c, also known as fracture toughness [7]. The value of critical stress intensity factor is amongst others dependent on the type of material, the thickness of the member and the loading rate [20, 23]. Figure 2.4 presents that the thicker the member, the lower the critical stress intensity factor is observed [24]. Therefore, the most critical situation occurs under the plane strain condition with the critical stress intensity factor equal to the fracture toughness K_{Ic} and therefore in most of the cases this value is assumed to be the critical stress intensity factor K_c [7].

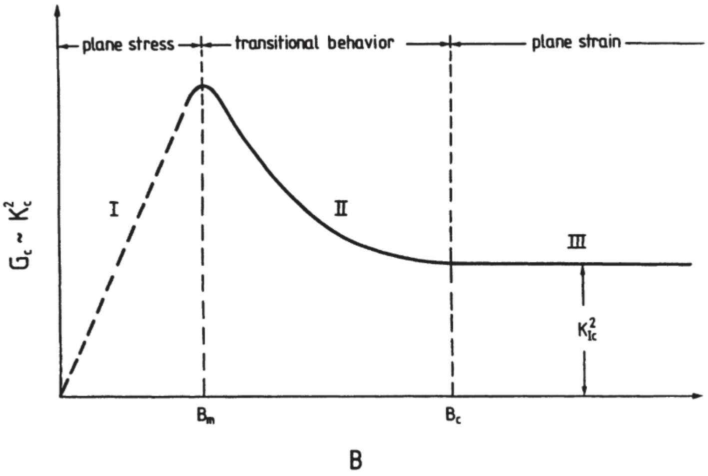

Figure 2.4: Critical stress intensity factor dependency on the thickness of the member [24].

2.2. Linear Elastic Fracture Mechanics

Linear Elastic Fracture Mechanics (LEFM) is a simplified basic theory of fracture [64] that defines the material's resistance to fracture. It characterizes the crack propagation starting from an initial crack size, but also allows to predict the moment of fracture. The investigation of crack propagation in sub-question 2 and 3 has been based on this theory. LEFM can be used in cases where an elastic global behaviour can be assumed. Elastic materials can be brittle or ductile. Brittle materials are fully elastic and no plasticity occurs. For ductile materials, however, relatively low yielding occurs at the tip of the crack, but that can be neglected [2]. Although elastic elements can be anisotropic, for simplicity, only isotropic materials will be further considered [41].

There are two approaches described in the LEFM to define the stress level at which the fracture occurs. One is through stresses and the other is through the energy balance.

2.2.1. Fracture due to the stresses

The fracture can be described by the atomic separation. The material undergoes fracture when the applied stress σ_A is larger than the material's cohesive strength σ_c and breaks the bond between the atoms. The cohesive strength is equal to equation 2.3 [2], where E is Young's modulus, x_0 is spacing between the atoms and γ_s is the surface energy per unit area. This surface energy is only half of the fracture energy because two new surfaces are created by the crack.

$$\sigma_c = \frac{E}{\pi} = \sqrt{\frac{E\gamma_s}{x_0}} \tag{2.3}$$

However, laboratory test results have proven that the material will undergo fracture before the fracture stress σ_f from the applied load reaches the limit of cohesive stress σ_c [58]. That is due to the flaws in the material [2]. Inglis did a research on an elliptical holes in a flat plate with the crack length of $2a$ and the crack width of $2b$ [29]. He proved that the material flaws create high stress concentrations, therefore, less stresses can be applied on the material. This relation was already stated in equation 2.1 of this report, when introducing the stress concentration factor K_t, but now is elaborated in the equation 2.4 with the geometrical parameters a and b of the crack.

$$\sigma_A = \sigma_f K_t = \sigma_f \left(1 + \frac{2a}{b}\right) \tag{2.4}$$

In the case of a longer crack with $a > b$ and a sharp crack tip, the stress level at the crack tip will go to infinity. However, in real material, there will always be a rounding of the crack tip ρ . The smallest value of the radius of the crack tip is close to the radius of the atom, therefore equality between $\rho = x_o$ can be assumed. Equation 2.4 can now be rewritten as follows:

$$\rho = \frac{b^2}{a} \tag{2.5}$$

$$\rho = x_o \tag{2.6}$$

$$\sigma_A = \sigma_f K_t = \sigma_f \left(1 + \frac{2a}{\sqrt{a\rho}}\right) = \sigma_f \left(1 + 2\sqrt{\frac{a}{\rho}}\right) = \sigma_f \left(1 + 2\sqrt{\frac{a}{x_o}}\right) \tag{2.7}$$

This is true for very brittle materials that have no plasticity properties. However, ductile materials will first experience yielding at the crack tip, also known as crack tip blunting.

Equation 2.7 needs to be adjusted when the crack length becomes much longer than the width $a >> b$:

$$\sigma_A = 2\sigma_f \sqrt{\frac{a}{x_o}} \tag{2.8}$$

As stated in the beginning of section 2.2.1, fracture will occur when the applied stresses in the material will reach the cohesive stresses $\sigma_A = \sigma_c$. To find an approximation of the stress value from the applied load that will cause the fracture, equation 2.3 and 2.8 have been set equal [2] and the fatigue stresses have been obtained.

$$\sigma_f = \sqrt{\frac{E\gamma_s}{4a}} \tag{2.9}$$

2.2.2. Fracture due to the energy balance

Another method to obtain the fracture stresses is through Griffith's energy balance [25]. This model states that for the fracture to occur, the potential energy Π coming from the internal strain energy and external force needs to be at a level equal or greater than the surface energy W_s.

$$-\frac{d\Pi}{dA} = \frac{dW_s}{dA} \tag{2.10}$$

Further elaboration leads to equation 2.11 for the calculation of the fracture stress.

$$\sigma_f = \left(\frac{2E\gamma_s}{\pi a}\right)^{1/2} \tag{2.11}$$

Results of the stress intensity and energy balance method for a sharp crack tip case in a brittle material give less than 40% difference, therefore they are comparable [2]. This is not the case when the radius of the crack tip ρ is significantly larger than the atomic radius x_0. In the case of the Griffith's energy balance, the radius of the crack tip ρ is not influencing the calculation and thus underestimates the fracture stress. However, in the case of the Inglis stresses model, the inclusion of ρ overestimates the fracture stress. Therefore, the true value is in between these two models. Irwin and Orowan modified the equation 2.11 from Griffith to account for the additional energy dissipation. The new term γ_p is included to add the plastic work per unit area to the previously prescribed surface energy per unit area γ_s.

$$\sigma_f = \left(\frac{2E(\gamma_s + \gamma_p)}{\pi a}\right)^{1/2} \tag{2.12}$$

2.2.3. Elastic stress field

Stresses in the body close to the crack tip with a finite radius, that follow a linear elastic material behaviour, can be obtained by defining a polar coordinate system as shown in figure 2.5.

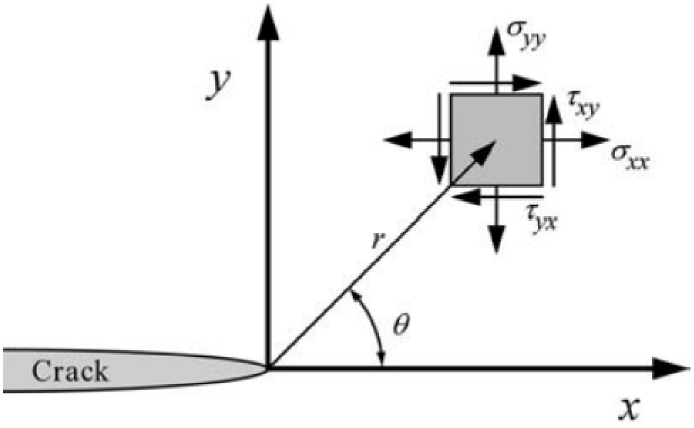

Figure 2.5: Polar coordinate axis defined at the crack tip [2].

Furthermore, a distinction between the three loading types needs to be made with the help of figure 2.6. Mode I is loading normal to the crack plane, mode II and III are the shear modes where mode II is the in-plane shear loading and mode III is the out-of-plane shear loading. In engineering practice, mode I is the most common, however, there can also be mixed-mode cases with two or even three of the modes combined.

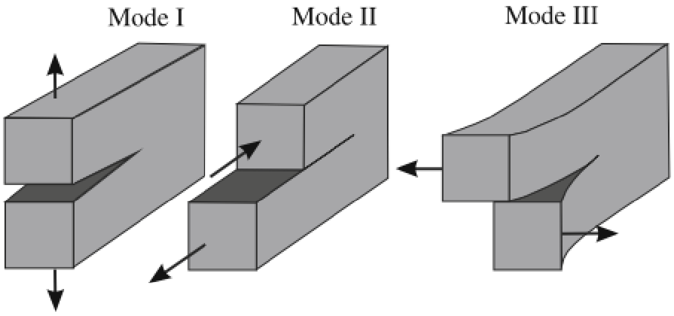

Figure 2.6: Three modes of the loading of the crack [41].

For each of the loading modes, Creager and Paris [12] have derived equations 2.13 till equation 2.20 for the elastic stress field at the tip of the crack.

Mode I:

$$\sigma_x = \frac{K_I}{\sqrt{2\pi r}} cos\frac{\theta}{2}[1 - sin\frac{\theta}{2} sin\frac{3\theta}{2}] - \frac{K_I}{\sqrt{2\pi r}} \frac{\rho}{2r} cos\frac{3\theta}{2} \tag{2.13}$$

$$\sigma_y = \frac{K_I}{\sqrt{2\pi r}} cos\frac{\theta}{2}[1 + sin\frac{\theta}{2} sin\frac{3\theta}{2}] + \frac{K_I}{\sqrt{2\pi r}} \frac{\rho}{2r} cos\frac{3\theta}{2} \tag{2.14}$$

$$\tau_{xy} = \frac{K_I}{\sqrt{2\pi r}} sin\frac{\theta}{2} cos\frac{\theta}{2} cos\frac{3\theta}{2} - \frac{K_I}{\sqrt{2\pi r}} \frac{\rho}{2r} sin\frac{3\theta}{2} \tag{2.15}$$

Mode II:

$$\sigma_x = -\frac{K_{II}}{\sqrt{2\pi r}} sin\frac{\theta}{2}[2 + cos\frac{\theta}{2} cos\frac{3\theta}{2}] + \frac{K_{II}}{\sqrt{2\pi r}} \frac{\rho}{2r} sin\frac{3\theta}{2} \tag{2.16}$$

$$\sigma_y = \frac{K_{II}}{\sqrt{2\pi r}} sin\frac{\theta}{2} cos\frac{\theta}{2} cos\frac{3\theta}{2} - \frac{K_{II}}{\sqrt{2\pi r}} \frac{\rho}{2r} sin\frac{3\theta}{2} \tag{2.17}$$

$$\tau_{xy} = \frac{K_{II}}{\sqrt{2\pi r}} cos\frac{\theta}{2}[1 - sin\frac{\theta}{2} sin\frac{3\theta}{2}] - \frac{K_{II}}{\sqrt{2\pi r}} \frac{\rho}{2r} cos\frac{3\theta}{2} \tag{2.18}$$

Mode II:

$$\tau_{xz} = -\frac{K_{III}}{\sqrt{2\pi r}} sin\frac{\theta}{2} \tag{2.19}$$

$$\tau_{yz} = \frac{K_{III}}{\sqrt{2\pi r}} cos\frac{\theta}{2} \tag{2.20}$$

In these equations ρ and θ are the polar coordinates. Factor $\sqrt{2\pi r}$ in the denominator shows that the stress field has a singular nature, meaning that with decreasing size of the radius of the crack tip ρ, stress values approach infinity. K_I, K_{II} and K_{III} are the stress intensity factors for the loading mode I, II and III. Stress intensity factor K is the characteristic parameter for the stress field that is around the tip of the crack [37] and is a very important parameter in the fracture mechanic calculations. The stress intensity factor is dependent on the local stresses and the structural and crack dimensions, therefore this factor has units of $Pa\sqrt{m}$.

There are two terms that need to be presented to obtain the stress intensity factor K. Those are the energy release rate $\mathcal{G}$ and J-Integral.

Energy release rate

In 1956, Irwin created a definition of the energy release rate $\mathcal{G}$ [31], also known as crack extension or driving force. He based his approach on Griffith's model but made it more suitable for engineering problems. Energy release rate $\mathcal{G}$ measures the energy needed to grow an increment of the crack as shown in the equation 2.21.

$$\mathcal{G} = -\frac{d\Pi}{dA} \tag{2.21}$$

If the energy release rate is known, the stress intensity factors for all three loading modes can be expressed by equations 2.22, 2.23 and 2.24 [41], where ν is the Poisson's ratio and E' is the Young's modulus. Different Young's modulus values for plain stress and plain strain situations are presented in equation 2.25 [13].

$$\mathcal{G}_I = \frac{K_I^2}{E'} \tag{2.22}$$

$$\mathcal{G}_{II} = \frac{K_{II}^2}{E'} \tag{2.23}$$

$$\mathcal{G}_{III} = \frac{K_{III}^2(1+\nu)}{E'} \tag{2.24}$$

$$E' = \begin{cases} E \text{ for plane stress} \\ \frac{E}{1-\nu^2} \text{ for plane strain} \end{cases} \tag{2.25}$$

If one of the loading modes is many times larger than the rest, it can be assumed that only this one mode is active. In the rest of the cases, the loading mode combines all three of the modes. This mixed mode behaviour can be analysed with one of the three formulas [4, 8, 15, 48]:

- the BK law

$$\mathcal{G}_{equivC} = G_{IC} + (G_{IIC} - G_{IC}) \left(\frac{G_{II} + G_{III}}{G_I + G_{II} + G_{III}} \right)^{\eta} \tag{2.26}$$

- the Power law

$$\mathcal{G}_{equivC} = \frac{G_{equiv}}{\left(\frac{G_I}{G_{IC}}\right)^{a_m} + \left(\frac{G_{II}}{G_{IIC}}\right)^{a_n} + \left(\frac{G_{III}}{G_{IIIC}}\right)^{a_o}} \tag{2.27}$$

- or the Reeder law

$$\begin{aligned}\mathcal{G}_{equivC} = G_{IC} + (G_{IIC} - G_{IC})\left(\frac{G_{II}+G_{III}}{G_I+G_{II}+G_{III}}\right)^{\eta} \\ + (G_{IIIC} - G_{IIC})\left(\frac{G_{III}}{G_{II}+G_{III}}\right)\left(\frac{G_{II}+G_{III}}{G_I+G_{II}+G_{III}}\right)^{\eta}\end{aligned}$$

G_{IC}, G_{IIC} and G_{IIIC} are critical energy release rates and a_m, a_n, a_o, η and n are the exponents that need to be defined when setting up the fracture criterion.

J-Integral

J-integral is a parameter in fracture mechanics, introduced by Chereoanov [11] and Rice [50]. It introduces a general approach for analysing the stress field around the crack tip. J-integral, also known as contour integral, is a line integral Γ calculated from the strain energy work W that is needed to cause a deformation per one unit of volume, the reaction vector T, the displacement vector u and ds that is an element of arch length along Γ [10], see equation 2.28 [50].

$$\mathcal{J} = \int_{\Gamma}\left(W dy - T\frac{\delta u}{\delta x}\,ds\right) \tag{2.28}$$

This equation presents an integral that is defined around the tip of the crack and has a counterclockwise positive direction. It starts from the lower crack surface, goes around the crack tip, and ends at the upper surface of the crack [10], as can be seen in figure 2.7. J-integral is path independent and should give the same value independently of the path that has been chosen. This characteristic gives freedom in the calculations to choose the most convenient path to obtain the value of the integral.

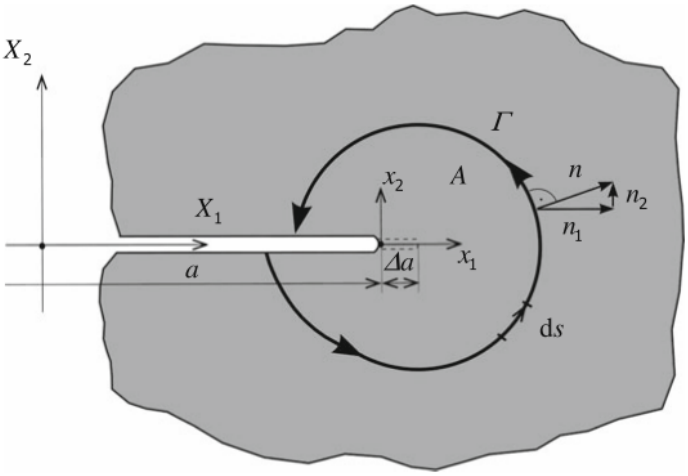

Figure 2.7: Visualization of the J-integral [41].

This parameter opens the possibility to extend the LEFM further to inelastic materials. However, in a simple case of elastic material, J-integral is equal to the energy release rate.

$$\mathcal{J} = \mathcal{G} = -\frac{d\Pi}{dA} \tag{2.29}$$

Once the value of the J-integral in an elastic material is evaluated, the stress intensity factor can also be obtained, which is the needed parameter for the crack growth investigation. Finite element analysis software like Abaqus can perform the calculation of the J-integral and provide the value of the stress intensity factor [16]. Therefore, this software is suitable for crack propagation analysis and will be used in this research.

2.3. Attempts to measure fatigue crack propagation

Existing steel bridges have longitudinal beams that support the rails. The longitudinal beams are coped at the joints with the cross-beams [27, 37, 51, 66]. These copes are prone to fatigue cracking [51]. As explained in the introduction, fatigue crack development in this connection due to dynamic loading by the passing trains could lead to a complete collapse of the structure [18].

Two ways to analyse the fatigue life of such a connection have been used in the past, being laboratory tests and measurements on bridges. They are marked with grey boxes in the beginning of the flowchart presented in figure 1.3. Both of these methods will be discussed in this section.

When performing measurements on bridges, strain gauges are being applied to the bridge to obtain measurements of the stresses due to normal traffic loads. Herewith, stress ranges are determined which can be used in fatigue analyses. However, in most cases, the locations of the connections are hard to reach, which makes the procedure costly. Additionally, this connection is located on both sides of each of the cross-beams, which are located at every end of every longitudinal beam. This leads to a great number of connections to be checked and explains the high expenses for such an approach. Despite these obstacles, ProRail has performed strain measurements on six existing bridges in the Netherlands in the 1980s and 1990s [37].

Another method to analyse the fatigue life and to get a better estimation of the stresses in the connection is by performing tests in a laboratory. These laboratory tests were performed by ProRail during their investigations in the 1980s and 1990s [37]. Also, master thesis research at the University of Alberta in 1988 [67] contains laboratory tests on a coped beam. Results of the latter of the two have been used as the validation material for the FE-models in this research. The report of the research done at the University of Alberta contains detailed information on their performed tests, as presented in the section 3.1 and 4.1. Therefore, this laboratory test setup has been chosen to reproduce the FE-model.

Based on the obtained results both from the measurements on the bridges and the tests in the laboratory by ProRail, advice for inspection intervals was established. However, these measurements and tests had some flaws that are described in section 2.3.1.

2.3.1. Flaws in the attempts

In 2014, TNO was asked to look into the laboratory tests done in the 1980s and 1990s by ProRail and evaluate the inspection advice for bridges. It was concluded that the performed tests only gave an approximation of the real situation [37]. The reasons for this conclusion were:

- Some of the tests had the tension plate and some did not, which changes the load path. Visualization of a connection with and without the tension plate can be seen in figure 2.8. The tension plate changes the load path. It transfers the moment present in the connection through this plate and then only shear forces need to be transferred through the coped area of the beam. Connection with or without the tension plate gives different stresses in the curve of the notch and therefore they cannot be compared.

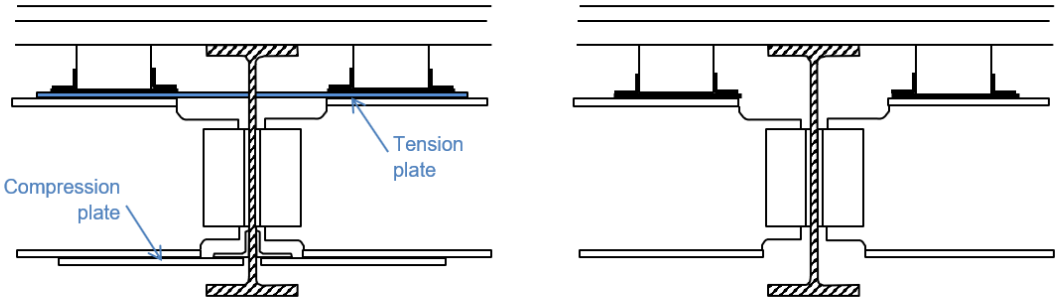

Figure 2.8: Cross-section of the connection with (left) and without (right) tension and compression plates [37].

- The load applied in the tests was a static load, while in reality, it is a dynamic load from the passing trains. Dynamic factors were calculated to convert the static loading to dynamic loading, but these are only an approximation of the dynamic factors in reality.

- Laboratory tests show that the stress level at the bottom cope is larger than the stress at the top cope. That opposes the data collected from the measurements on the bridge where the stress level at the top cope is larger. This difference was not explained in the report [37].

Apart from the limitations in the laboratory tests, there are also limitations in the measurements on bridges and in the reporting of it. Results can differ strongly per measurement [37] due to one or both the following reasons:

- The stress gradient at the curve of the cope is much higher than close to the cope. Therefore, the exact location of the strain gauge is essential. Unfortunately, the precise location of the strain gauges was not mentioned in the reports.
- If the rail is not located exactly on top of the longitudinal beam, torsion is introduced into the top flange. This creates different stress values on the two sides of the web of the longitudinal beam. Report [37] does not contain information on the rail location.

The conclusion of the paper written in 2014 [37] is that to ensure the safety of railway bridges with coped steel beam connections with respect to the fatigue life, a detailed finite element analysis should be performed for the connection between the coped longitudinal girders and the transverse supporting system. This finite element analysis model will give a revised relation between the crack length and the number of load cycles. Based on that, revised inspection intervals should be given to prevent fatigue failure. This is the main motivation behind this thesis research.

2.4. XFEM model

It used to be hard to capture moving discontinuities like cracks by the ordinary finite element method as the mesh needed to match the geometry of the crack after each step of its growth. Hence, a lot of remeshing was needed [43]. This complicated meshing can be seen in the left picture from figure 2.9.

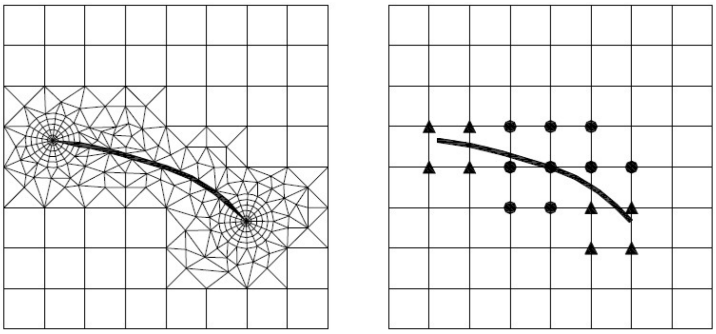

Figure 2.9: Visualization of the mesh with:
ordinary FEM on the left
eXtended Finite Element Method on the right side [49].

The discretization by ordinary FEM can be expressed with equation 2.30 [39] where u^h is a displacement vector function, u_i are degrees of freedom at the node $i \epsilon I$ and ϕ are the shape functions. Displacement in the finite element analysis software Abaqus is expressed in millimeter mm.

$$u^h = \sum_{i \epsilon I} u_i \phi_i \tag{2.30}$$

To fix the complicated mesh alignment problem and move from the left picture to the right one in figure 2.9, the partition of unity finite element method (PUFEM) is used in Abaqus. It allows modifying the information in the finite element space with the previously known analytical information that is known in advance and can ease the process of finding the solution for the software [42]. In the extended finite element method (XFEM) development process, it allows enriching the displacement-based approximation seen in the equation 2.30 by implementing additional functions. In other words, to include more knowledge about the crack. The only difference between PUFEM and XFEM is that the extended finite element method has only a local enrichment of the displacement field [1]. It is only applied in the area of cracks and others discontinuities.

First, Belytschko and Black suggested the implementation of the asymptotic function F_α at the crack tip [3] that deals with the singularity present at the crack tip. Later, this approximation was further improved with the discontinuous function, or “jump” function $H(x)$, introduced by Möes, Dolbow and Belytschko [43] that allows the crack to propagate through the elements and split them in two parts. Figure 2.10 has an arbitrary crack in the XFEM mesh. Tip enriched elements present those elements that will be enriched by the asymptotic function, and split elements by the jump function.

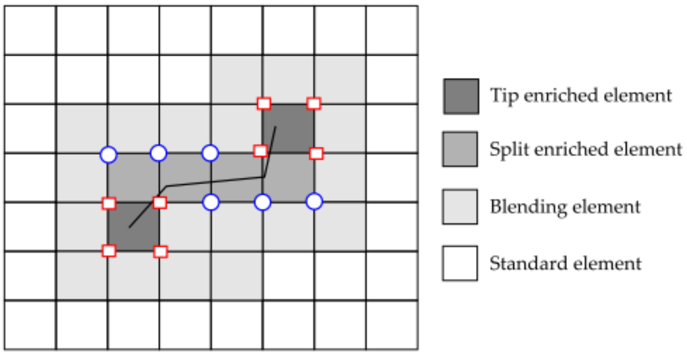

Figure 2.10: An arbitrary crack with the XFEM mesh [39].

After these adjustments, the discretization of XFEM in one dimension can be expressed with equation 2.31 [55], which applies only to isotropic and elastic materials [21].

$$u^h = \sum_{i\epsilon I} u_i\phi_i + \sum_{j\epsilon J} b_j\phi_j H(x) + \sum_{k\epsilon K} \phi_k[\sum_{l=1}^{4} c_k^l F_l(x)] \tag{2.31}$$

u_h is a displacement vector function, u_i, b_j and c_k are degrees of freedom at the node $i\epsilon I$, $j\epsilon J$ and $k\epsilon K$ respectively. j are the nodes that the crack surpasses and k contains the crack tip. ϕ are the shape functions. $H(x)$ and F_α are the previously described jump functions and asymptotic functions. I is the set of all nodes that contain J and K nodes. The crack goes through the J nodes but the crack tip is at the K nodes [55].

The “jump” functions $H(x)$, also known as the Heaviside functions, are applied to the fully cracked elements. The asymptotic function F_α however is needed for the partially cracked elements at the ends of the crack [38]. This function spots the singularity introduced by the tip of the crack with the $\sqrt{r}$ term, but is only considered when a stationary crack is modelled. The exact formulation of the asymptotic function F_α is given by equation 2.32 [5, 34, 38, 43, 55].

$$F_\alpha(r,\theta) = \left\{\sqrt{r}sin(\frac{\theta}{2}), \sqrt{r}cos(\frac{\theta}{2}), \sqrt{r}sin(\frac{\theta}{2})sin(\theta), \sqrt{r}cos(\frac{\theta}{2})sin(\theta)\right\} \tag{2.32}$$

The finite element analysis software Abaqus has incorporated these enrichment functions and enabled the possibility to model the crack propagation without the need for re-meshing. Therefore, this tool has been used when modelling crack propagation for sub-question 2 and 3.

2.4.1. Fracture criterion in Abaqus

In section 2.2 LEFM was introduced and in sub-section 2.2.1 and 2.2.2 the two approaches for obtaining the fracture criterion, through the stresses and through the energy balance, were presented. When the crack propagation analysis is being performed through the computer software Abaqus, these two approaches are further elaborated and a choice between six different fracture criteria can be made [56]. These six criteria are critical stress, critical crack opening displacement, crack length versus time, the Virtual Crack Closure Technique (VCCT), enhanced VCCT, and the low-cycle fatigue criterion. In this research, two of the possible options are used and therefore these are explained more in detail.

VCCT

The Virtual Crack Closure Technique (VCCT) has been used in this research when answering sub-question 2. It is one of the two methods for stationary crack modelling that were used to verify the results obtained by the XFEM. This method is also known as the crack closure method and has been developed based on the work done by Irwin [30]. He defined the crack closure integral, presented in equation 2.33, where strain energy release rate G_I is expressed though the virtual crack extension δa, normal stress distribution at the crack tip σ_y and the displacements for the crack opening $v(r)$ [17].

$$G_I = \lim_{\delta a \to \infty} \frac{1}{2\delta a} \int_0^{\delta a} v(r)\sigma_y(r)\,dr \tag{2.33}$$

Irwin's integral was later modified and currently the VCCT technique is based on the energy balance criterion. This technique states that there has to be an equality between the energy that is needed to be able to close a crack of a certain length and the strain energy that is released when the same length crack is being opened [33]. The first part of equation 2.34 shows the criterion for the fracture to occur for a simplified situation where only Mode I is taking place [15]. It presents that the energy release rate G_I for Mode I needs to be larger than the critical Mode I energy release rate G_{IC} for the crack to propagate.

$$f = \frac{G_I}{G_{IC}} = \frac{1}{2}\left(\frac{v_{1,6}F_{v,2,5}}{bd}\right)\frac{1}{G_{IC}} \geq 1,0 \tag{2.34}$$

Figure 2.11 helps to explain the second part of equation 2.34 where the energy release rate for Mode I, G_I, is further elaborated through the vertical force $F_{v,2,5}$ present between node 5 and 2, the distance $v_{1,6}$ between node 1 and 6 and width b and the length d of the element located at the tip of the crack [15]. This method is applicable when a brittle fatigue crack growth occurs.

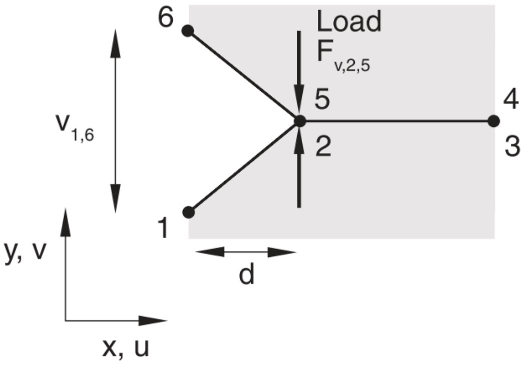

Figure 2.11: VCCT visualization for the Mode I [15].

Low-cycle fatigue criterion

The second analysis option from Abaqus, i.e., the low-cycle fatigue criterion, is used when a progressive damage needs to be investigated and the failure needs to be determined for bulk ductile materials by using a direct cyclic approach [15]. Since the coped beam connections are subjected to cyclic loading conditions and the aim is to analyse the crack propagation, the low-cycle fatigue criterion is used.

2.4.2. Prediction of the direction of crack propagation in Abaqus

There are many prediction methods to determine the angle in which the crack will propagate. Abaqus software has implemented three of them: maximum tangential stress, maximum energy release rate, and $K_{II} = 0$ criterion [15]. When using these criteria, the loading mode K_{III} is not considered since the generally accepted theory for the crack propagation when K_{III} is not equal to zero, which is still not developed in Abaqus [15].

Maximum tangential stress

In this research, the maximum tangential stress criterion has been used to predict the direction of the crack propagation in sub-question 2 and 3. It is based on the stress field description in front of the crack tip defined by Williams in 1957 [36] presented in the equation 2.35 [40].

$$\sigma_{\theta\theta} = \frac{1}{\sqrt{2\pi r}} cos\frac{\theta}{2}\left(K_I cos^2\frac{\theta}{2} - \frac{3}{2}K_{II} sin\theta\right) + T sin^2\theta \tag{2.35}$$

In this equation, K_I and K_{II} are the stress intensity factors for modes I and II. θ and r are the polar coordinates. θ is the crack propagation angle measured with respect to the crack plane and is derived by differentiating equation 2.35 with respect to θ, see equation 2.36.

$$\theta = cos^{-1}\left(\frac{3K_{II}^2 + \sqrt{K_I}^4 + 8K_I^2K_{II}^2}{K_I^2 + 9K_{II}^2}\right) \tag{2.36}$$

3

Fatigue crack initiation in a coped beam

The fatigue life of a crack starts with the crack initiation. In this chapter, FEM software, Abaqus, has been used to perform a static loading test of a coped beam to analyse the stress concentrations in the curve of the cope. The location with the highest stress level has been obtained and therefore the point where the crack starts initiating has been found. This location is the answer to sub-question 1. The model has been validated by comparing the longitudinal stresses along the web with laboratory test results.

First section 3.1 explains the details about the laboratory test performed by Michael C.H. Yam and J.J. Roger Cheng. Then section 3.2 describes the finite element model made in Abaqus software in more detail. This model is designed such that it best matches the laboratory test described in section 3.1. In section 3.3 the results of the FEM analysis have been compared to the laboratory test results performed by Michael C.H. Yam and J.J. Roger Cheng.

3.1. Reference data from the laboratory tests

In 1988, the fatigue strength of coped beams was investigated by Michael C.H. Yam and J.J. Roger Cheng [65, 67]. They performed static and cyclic loading tests in the laboratory to investigate the fatigue behaviour of coped beams and to compare the results with existing S-N curves in the Canadian design standard. The static loading test was done to remove the residual stresses near the cope and to ensure its elastic response for when the cyclic loading will be applied. During this static loading, longitudinal stresses along the web were registered. The tests as performed by Yam and Cheng are described in more detail in this section.

3.1.1. Test setup

Nine steel beams with a length of 4876 mm were prepared from three steel sections CB-1, CB-2, CB-3, and coped at both ends with a varying radius of 0 mm, 10 mm, 20 mm and 30 mm. These beams had a steel W410 x 54 CSA G40.21-M81 300W profile, where W410 x 54 indicates the geometrical parameters of the cross section, CSA G40.21 stands for Standard for Structural Steel Issued by Canadian Standards Association and 300W is the steel grade representing a weldable steels for general construction with the yield strength of 235 MPa [9]. Steel beam as an end product from a steel manufacturer always has a deviation from the intended geometrical parameters, therefore, measurements of the true beam's cross sections sizes were measured and are gathered in figure 3.1

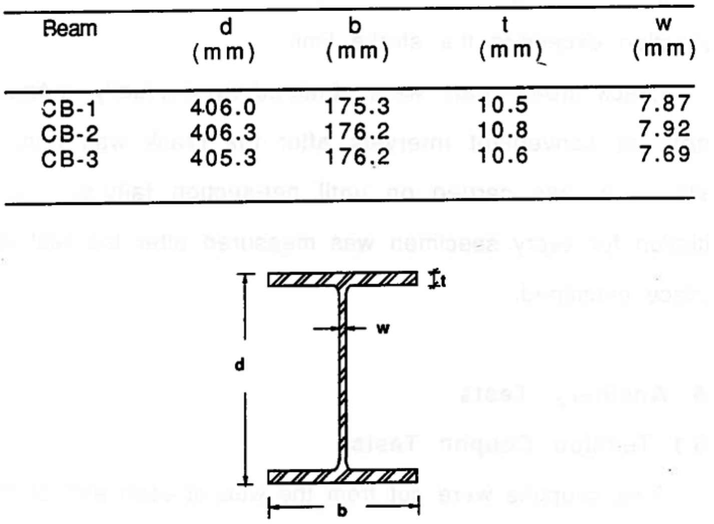

Beam	d (mm)	b (mm)	t (mm)	w (mm)
CB-1	406.0	175.3	10.5	7.87
CB-2	406.3	176.2	10.8	7.92
CB-3	405.3	176.2	10.6	7.69

Figure 3.1: Measured dimensions of the cross section for the three steel sections [67].

All specimens were simply supported with a rocker for free rotation and with rollers for no vertical movement. On the right side, the support is connected to the web of the beam by two bolted clip angles ensuring the load transfer to the support. The tested beams had a span of 3670 mm and they were loaded with a point load in the middle of the span, see figure 3.2.

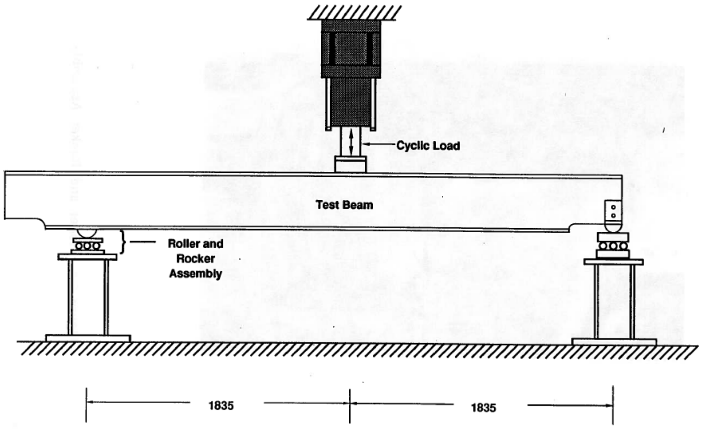

Figure 3.2: Laboratory test setup [67].

The lateral stability was obtained by the lateral constrain at the location of the load application to analyse the in-plane behaviour of the beam. Material properties (modulus of elasticity, yield, and ultimate strength) were obtained by the coupon tests performed on two coupons cut out of each end of the steel section.

The copes had a depth of 60 mm and a length of 230 mm, measured from the support, and these dimensions were kept constant in all specimens. The geometry of the cope can be seen in figure 3.3. Three different cutting techniques were used to cut the copes, flame cutting, smooth grinding after flame cutting, and hole drilling accompanied with tangent removal by flame cutting. However, in this thesis, no distinction between them has been made and all nine specimens with different cutting techniques have been analysed.

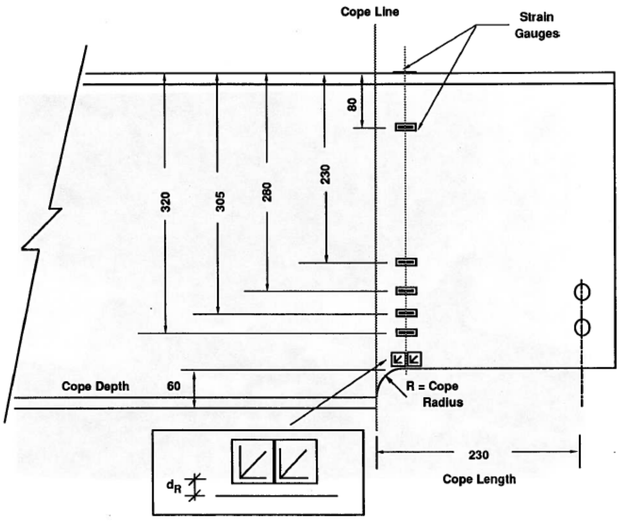

Figure 3.3: Location of rosettes and the strain gauges [67].

The static loading test was performed until the maximum load for the dynamic test was reached. However, the stress distribution for all specimens was measured and presented at 100 kN loading. Therefore, validation of the FE-model for the crack initiation analysis has been done based on the stress values at the rosettes from when the static load of 100 kN has been applied.

Two rosettes were located side-by-side next to the cope such that one of them was placed on the theoretical tangent of the cope radius. They were used to measure the introduced stresses in the steel due to the cope's geometry. The rosettes were located as close as possible to the edge of the cope, however, not exactly on the edge. This observation may be of importance when the data from the laboratory will be compared with the results from the FE-model made in this thesis. These distances from the rosettes to the geometry of the cope, d_R, can be seen in figure 3.3 and are gathered in table 3.1 together with the nominal and actual cope radii. Different letters in the specimen designations stand for different surface preparations. A, B, C and no letter stand for flame cutting (F in table 3.1), D for grounded smooth after flame cutting (FG), and E indicates hole drilling accompanied by the tangent removal with fire cutting (D). As previously stated, different surface conditions have not been considered in this thesis.

Strain measurements were obtained by strain gauges that were located on a vertical line starting between the two rosettes. The placement of the rosettes and strain gauges can be seen in figure 3.3. Two additional strain gauges were placed on the top and bottom flange of the beam 720 mm away from the cope line. This is the location with the least effect caused by the support and load application zones and can be used to measure and maintain the nominal mean stress during the laboratory test.

Specimen Designation	Nominal Cope Radius (mm)	Actual Cope Radius (mm)	Rosettes Location d_R (mm)	Cutting Technique
CB-0	0	0	3	F
CB-10A	10	15	4	F
CB-20B	20	25	5	FG
CB-20A	20	25	2	F
CB-30	30	32	3	F
CB-10B	10	15	4	F
CB-10C	10	15	3	F
CB-10D	10	15	3	FG
CB-10E	10	10	4	D

Table 3.1: Description of the specimens [67] with different cutting techniques:
F - flame cutting technique,
FG - grounded smooth after flame cutting,
D - hole drilling accompanied by the tangent removal with fire cutting.

3.1.2. Obtained results

The coupon test results for each steel beam, which was later cut into three separate specimens, are summarised in table 3.2. They provided the necessary material properties.

Beam	Static Yield Strength (MPa)	Ultimate Strength (MPa)	Modulus of Elasticity (MPa)	Percent Elongation at Rupture
CB-1	375	498	198600	33
CB-2	369	490	200600	32
CB-3	366	490	202300	31

Table 3.2: Material properties obtained by the coupon test [67].

At the location of the cope, stresses were measured throughout the height of the web of all nine beams. These results were presented in separate graphs. One of these is presented in figure 3.4, showing the stresses at different strain gauges when a constant load of 100 kN is applied. The other eight graphs can be found in appendix A. Exact stresses were not registered in the report, but approximate values can be extracted from the presented graphs. From these results, it was obtained that a smaller radius of the cope leads to higher stress concentrations. Accordingly, coped beams with smaller cope radius are more prone to crack initiation and is therefore the reason to choose the result with the smallest cope radius of 10 mm to be presented in figure 3.4.

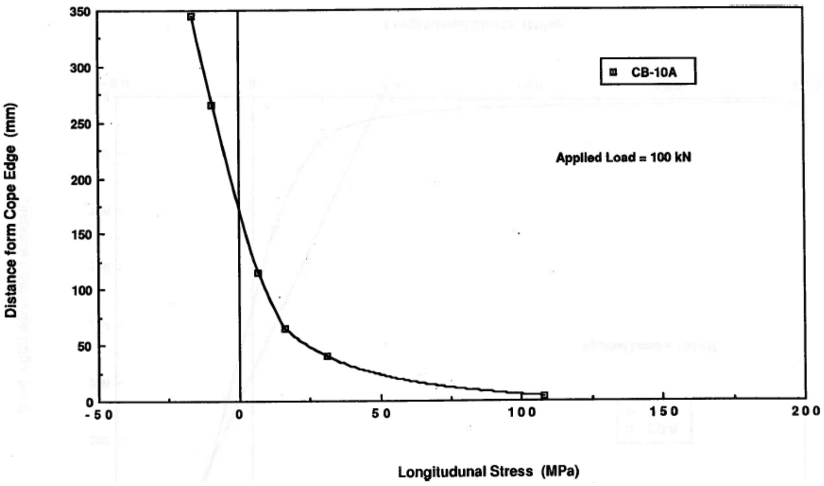

Figure 3.4: Stress distribution in the web of the beam above the cope under 100 kN loading for the specimen CB-10A [67].

After static loading, all nine specimens were further cyclically loaded to investigate crack propagation until full collapse of the beam. This data has been further used in section 4.1, when crack propagation is modelled.

After full collapse of the beam, it was possible to obtain the precise location of the crack initiation. In all nine samples, the crack initiated in the curve of the cope. To present the location of the crack initiation, a new variable F_d was introduced, which is the horizontal distance from the end of the curve until the location of crack initiation as shown in figure 3.5. The obtained location of the crack initiation is summarised in table 3.3. When analysing the results for the specimens with a 10 mm cope radius, it can be seen in table 3.3 that the location of the crack initiation for of 9.98 mm for specimen CB-10A is considerably larger than for the other samples. This result needs to be disregarded in the future analysis due to the discovery of a preexisting 1 mm deep notch in the surface. This surface damage enforces the crack to initiate at the location of the notch and therefore this result has been excluded from in the table 3.3.

With the information presented in this section, being the stress values along the height of the beam and the location of the crack initiation, FE-model has been validated in section 3.3.

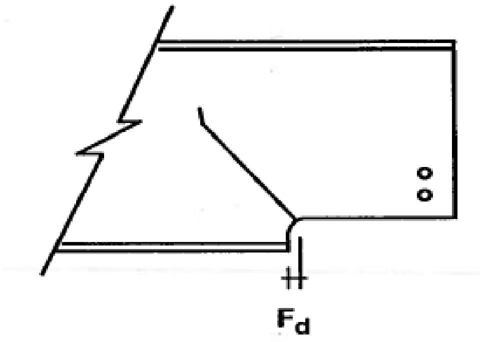

Figure 3.5: Location of the crack initiation [67].

Specimen Designation	**Crack Initiation** F_d **(mm)**
CB-0	at corner
CB-10A	~~9.98~~
CB-10B	4.81
CB-10C	6.47
CB-10D	7.53
CB-10E	4.00
CB-20A	16.23
CB-20B	12.09
CB-30	24.87

Table 3.3: Location of the crack initiation [67].

3.2. Test simulation with model in Abaqus

3.2.1. Geometry, material properties, and loading

To be able to compare the modelling results for the crack initiation point with the laboratory test results, a linear elastic 3D finite element model has been created according to the laboratory test setup by using the same geometry, material properties, boundary conditions, and loading parameters described in section 3.1.1 and visualized in figures 3.2 and 3.3. The chosen geometry of the cross section can be seen in figure 3.6 and has been obtained by averaging the measurements from the members used in the laboratory test that were presented in figure 3.1.

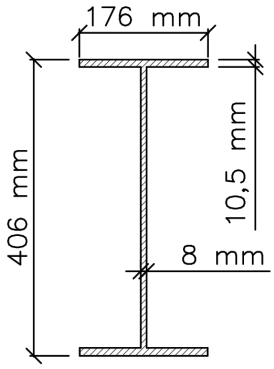

Figure 3.6: Geometry of the cross section in FE-model.

The geometry has been created with a solid extruded part. The rounding between the flanges and the web of the beam has been neglected for the simplicity of the model, but might have an influence for the cases when the cope has a large radius. The beam has been coped by removing part of the web and the bottom flange at both ends of the beam. The corner of the cope has been rounded to a radius that varies between 10, 20, and 30 mm.

Material properties have been defined by assigning the modulus of elasticity and the Poisson's ration for a linear elastic material. Based on the coupon test results presented in table 3.1, an average value of 200500 MPa for the modulus of elasticity has been used. The material has been defined to be isotropic with Poisson's ratio of 0.3 in an elastic stage [45].

Boundary conditions, described in section 3.1.1, represented a simply supported beam where both supports had a roller and rocker assembly. The right support additionally had two bolt clip angle. As presented in figure 3.7, these boundary conditions have been reproduced in the FE-model by fixing the displacement in all three directions at the right side support and keeping the movement in the x direction free at the left side support.

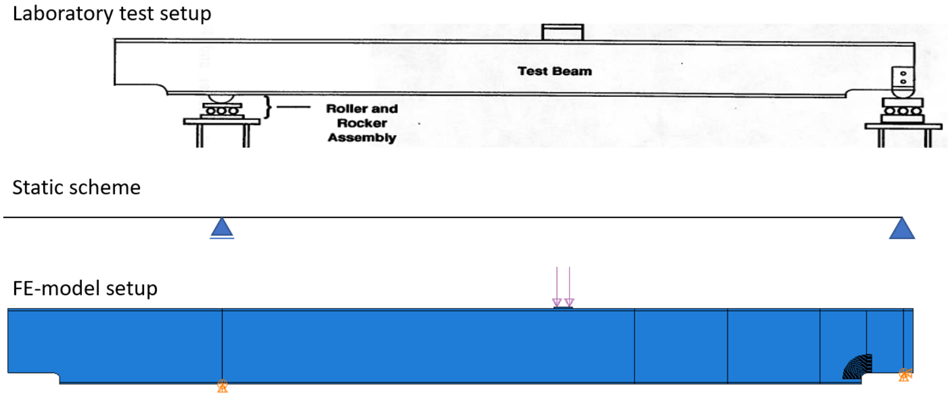

Figure 3.7: Boundary condition transition from the laboratory test setup to the FE-model explained through the static scheme. Laboratory test visualization is stretched to match the location of the supports and has no true dimensions.

A static load of 100 kN was applied to the beams during the laboratory tests when the longitudinal stresses over the height of the web were measured. To be able to compare the stresses in the FE-model with the stresses from the laboratory test, the same loading of 100 kN needed to be applied to the model. Load has been applied in the middle of the beam, 1835 mm away from each of the supports. Instead of a point load, an additional steel plate has been modelled to distribute the load over a 100 x 100 mm area to avoid singularities in the results [6]. Load has been applied under the static, general step in Abaqus.

Figure 3.8 summarizes the described geometry, loading, and boundary conditions of the model.

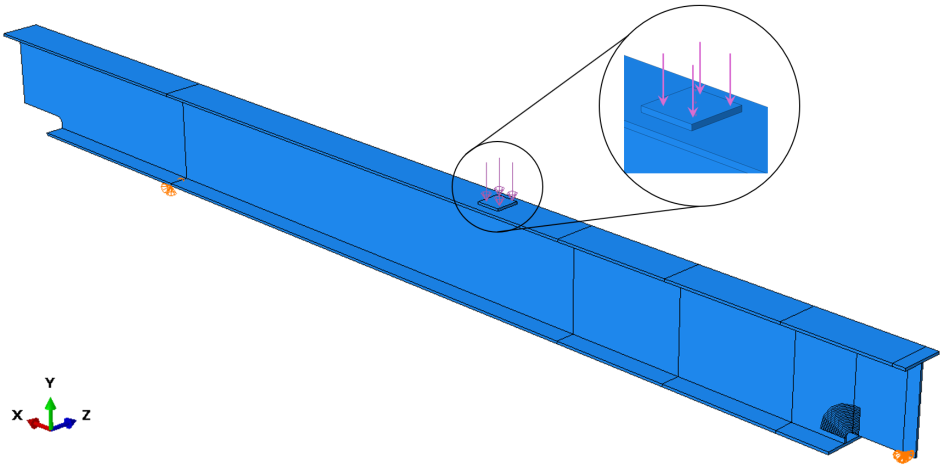

Figure 3.8: Geometry, loading and the boundary conditions of the beam from Abaqus.

3.2.2. Meshing

8-node linear brick elements C3D8 have been used to mesh the model. This choice of element type is not a mandatory requirement for the crack initiation analysis. However, this model has been further updated and used in chapter 4 for the crack propagation analysis. There it is required to have linear elements for the crack to propagate when using XFEM [62]. To save time on remodeling and to reduce the amount of changes needed during the transition from the crack initiation model to the propagation model, C3D8 elements have been already applied in the crack initiation model.

As can be seen in figure 3.9, mesh refinement has been applied at the area close to the cope radius, which is the area of interest. A quarter of a spider mesh has been sketched around the curve by partitioning the face of the web in Abaqus.

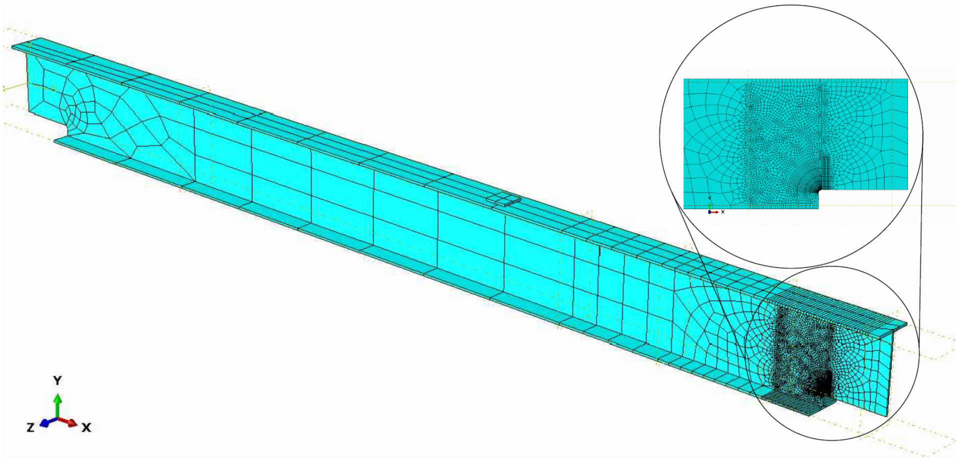

Figure 3.9: Meshing of the beam from Abaqus.

3.3. Comparison of the results

3.3.1. Longitudinal stresses

Comparison of the FE-model and laboratory test was done by comparing the longitudinal stresses along the height of the web of the beam that were registered during the laboratory tests in figure 3.4 and the appendix A, with the stresses that have been calculated by the finite element model. A vertical path starting from the tangent of the cope has been created in the model and is presented in figure 3.10. This path aligns with the location of the rosettes in the laboratory test setup that were presented in figure 3.3.

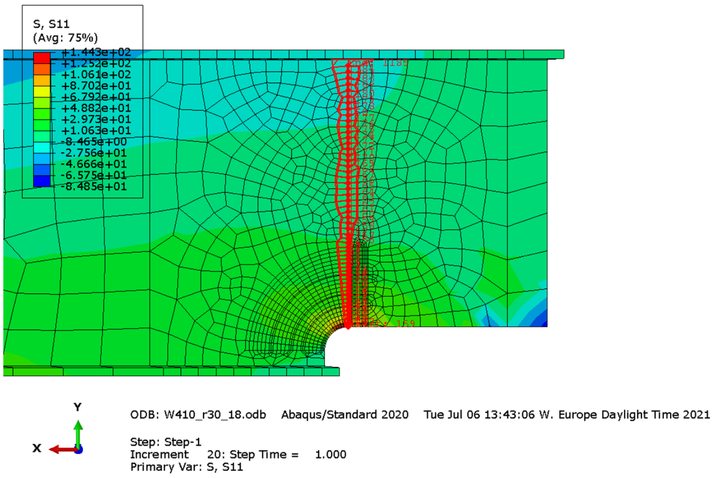

Figure 3.10: Visualization of the vertical path from the tangent of the cope. Additionally, the longitudinal stress values can be observed.

From this path, the principal stresses have been computed along the height of the web and are presented in the graphs of longitudinal stresses versus distance from the cope edge, see figure 3.11, figure 3.12 and figure 3.13 for 10 mm, 20 mm, and 30 mm cope radius, respectively. Results from the laboratory test results are plotted in the same figures.

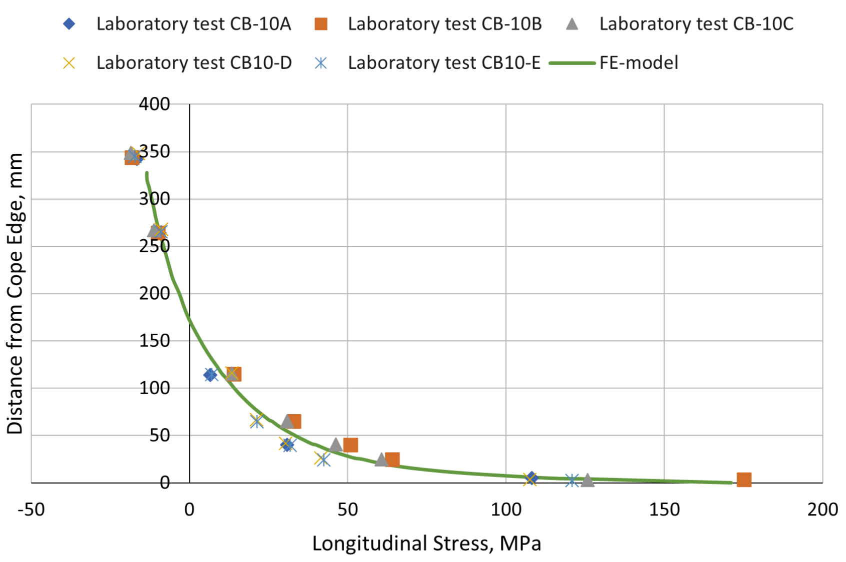

Figure 3.11: The longitudinal stress dependency on the distance from the cope edge for beams with cope radius of r = 10 mm.

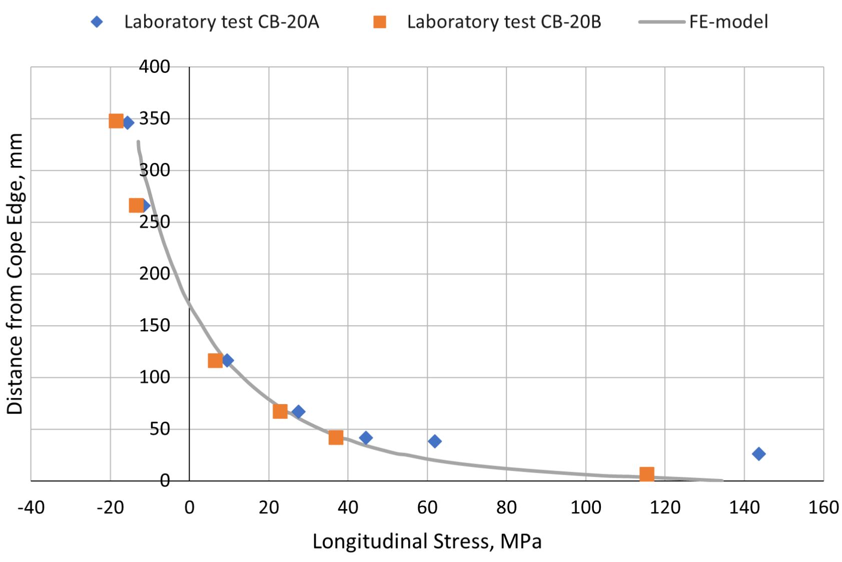

Figure 3.12: The longitudinal stress dependency on the distance from the cope edge for beams with cope radius of r = 20 mm.

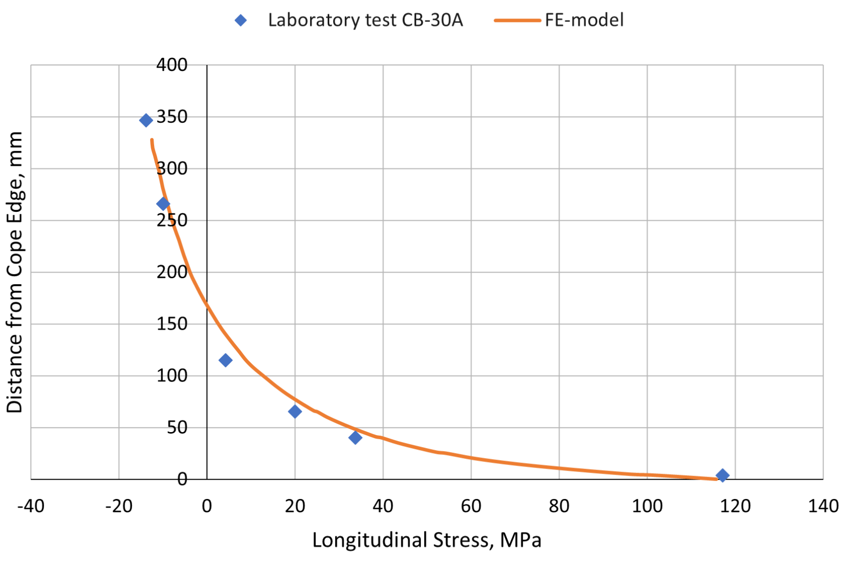

Figure 3.13: The longitudinal stress dependency on the distance from the cope edge for beams with cope radius of r = 30 mm. Only one laboratory test was performed with cope radius of 30 mm.

An option to reduce the computational time was investigated by using elements with reduced integration. However, the FE-model result curves were not as smooth as the curves presented in figures 3.11 up to 3.13. Therefore, it has been decided to continue working with elements without reduced integration.

Figure 3.14 shows the difference between the obtained longitudinal stress results from the FE-model and the data from the laboratory tests. Greater deviation has been observed closer to the edge of the cope, showing the large variation in the laboratory test results. The results from the FE-model lay in between the results from the laboratory tests. Hereby, the FE-model is validated and can be applied for further analysis.

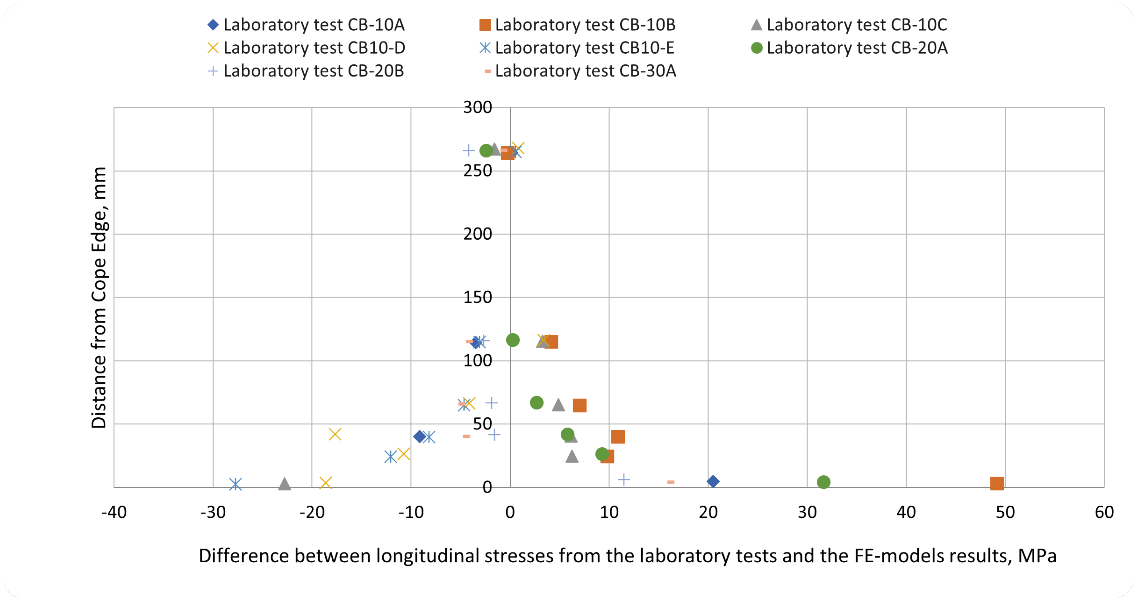

Figure 3.14: Difference between longitudinal stresses obtained from the laboratory test and the FE-model for the cope radius of 10 mm, 20 mm and 30 mm.

3.3.2. Location of the crack initiation

The location of crack initiation has been determined by looking at the stress levels at the rounding of the cope when a 100 kN load has been applied and by identifying the location of the peak stresses measured from the cope line. This location has been compared to the measured crack initiation location from the test results and this comparison is presented in table 3.4 where A, B, and C stand for flame cutting technique, D for grounded smooth after flame cutting, and E indicates hole drilling accompanied by the tangent removal with fire cutting. As explained in section 3.1.2, results for for specimen CB-A have been disregarded due to a preexisting notch.

As explained in chapter 3.1, it has been expected to find some deviation between the laboratory test results and the results from the model due to the location of the stress measuring rosettes. Although the reported crack location from the laboratory tests is assumed to be the distance from the edge of the cope to the crack location, it is expected that in reality this is not exactly the distance to the edge of the cope therefore creating some mismatch in comparison to the FE-model. However, the analysis still shows comparable results as FE-model results lay in the range of the laboratory test results with 10 and 20 mm cope radius. Only one laboratory test has been performed with a cope radius of 30 mm, so there is no range within which the results should lay in, nonetheless the difference in the crack location from the laboratory test and the peak stress location from FE-model is only 3.61 mm for 30 mm cope radius.

F_d	**r=10mm**	**r=20mm**	**r=30mm**
Laboratory test CB-A	~~9.98~~	16.23	24.87
Laboratory test CB-B	4.81	12.09	
Laboratory test CB-C	6.47		
Laboratory test CB-D	7.53		
Laboratory test CB-E	4.00		
Range from lab. t.	**4.00 to 7.53**	**12.09 to 16.23**	**24.87**
FE-model	**7.09**	**14.18**	**21.26**
Withing the range	✓	✓	
Difference in %			14.52
Difference in mm			3.61

Table 3.4: Location of the crack initiation F_d measured from the cope line both from the laboratory tests and the FE-model

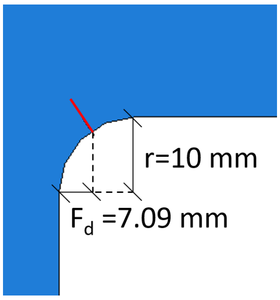

Figure 3.15: Example of FE-model results for F_d and r from table 3.4.

The result shows a good comparison between the laboratory test results and the results from the FE-model. That shows that the FE-model with the assumed boundary conditions, load application, and the chosen mesh is a reliable model for coped beam analysis when a static load has been applied. The location of the crack initiation has been obtained, therefore, sub-question 1 has been answered.

3.4. Conclusions for the crack initiation

The crack initiation investigation presented in chapter 3 has provided a starting point for the crack propagation analysis described in chapter 4.

Firstly, a verified FE-model has been created in section 3.2 and 3.3.1 and further has served the purpose of a base model. By implementing the changes described in section 4.2, it has been transformed into a crack propagation model.

And secondly, the location of the crack initiation has been determined and is presented in table 3.4. Based on this information, an initial crack has been modelled at a distance of 7.09 mm from the cope line when the cope radius is 10 mm as is described in section 4.2.

4

Fatigue crack propagation in a coped beam

In chapter 3, the crack initiation phase of the fatigue life was investigated to find the location where the crack starts to initiate. Chapter 4 presents the investigation of the next phase of the fatigue life which is crack propagation.

The FE-model that has been created for the crack initiation, has been further modified by applying an initial crack and, instead of static loading, cyclic loading has been applied. This model has been calibrated to match the results from the laboratory tests performed by Michael C.H. Yam and J.J. Roger Cheng regarding cyclic loading [65, 67]. The path of the crack was not registered during the tests, therefore, the extended finite element method (XFEM) has been used to propagate the crack without predefining the path of the crack.

4.1. Reference data from the laboratory tests

4.1.1. Test setup

The geometry parameters of the laboratory test, presented in this section, are the same as described in section 3.1. However, now a cyclic loading has been applied, instead of a static load of 100 kN, to investigate the crack propagation in the web of the beam. During the tests, a nominal mean stress of 70 MPa has been maintained at the location of the cope that is marked with a red dot in figure 4.1.

Due to the incomplete explanation of the load applied in the laboratory test report [67], an extensive analysis is given in this section on the load applied to the beam. Here, the bending moment distribution for a simply supported beam with a force applied at the middle of the span is presented in figure 4.1. This distribution is presented to show the calculation of the force that needs to be applied to maintain the nominal mean stress value of 70 MPa at the location of the cope.

Firstly, it is determined what load needs to be applied to reach this nominal stress of 70 MPa at the cope. Hereto, the moment M_3 at the location of the cope line should be obtained by using equation 4.1. In this equation, cross-sectional properties, I_3 and y_3, of the incomplete cross section of the beam have been considered due to the cope of the beam. This cross-section is visualized in the figure 4.1 with the section A-A.

$$M_3 = \frac{\sigma_3 I_3}{y_3} = \frac{70MPa * 5,79 * 10^7 mm^4}{238,3mm} = 17kNm \tag{4.1}$$

I_3 stands for the second moment of area. y_3 is the distance from the elastic neutral axis to the physical outer fibre, calculated as shown in equation 4.2.

$$y_3 = \frac{\sum y_j A_j}{\sum A_j} = 238,3mm \tag{4.2}$$

A is the cross-sectional area and y the distance from the elastic neutral axis to the physical outer bottom fibre of each j-th cross-sectional element ($j = 1$ the web and $j = 2$ top flange).

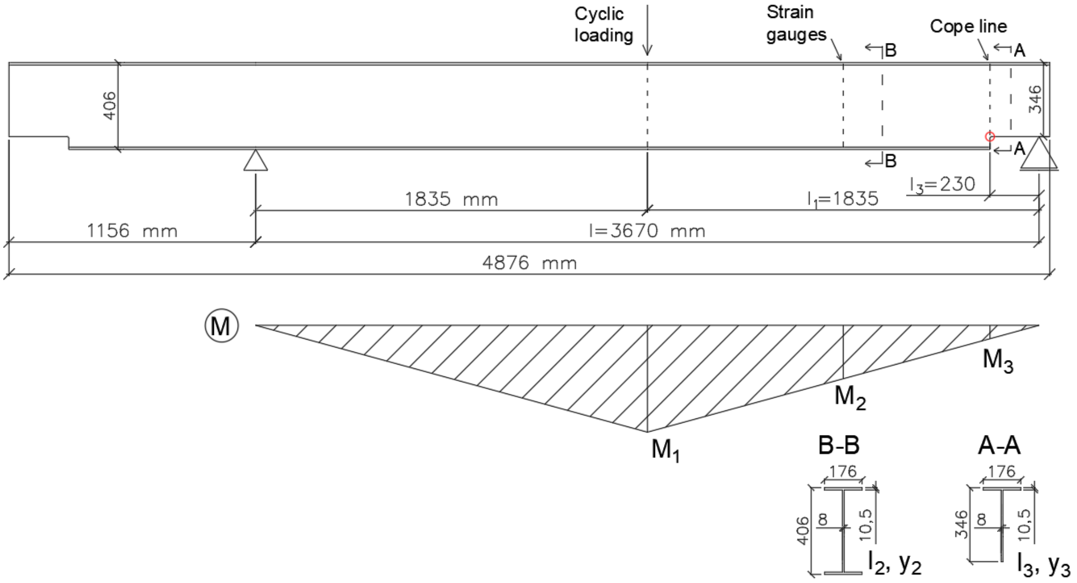

Figure 4.1: A scheme of a simply supported coped beam together with it's static scheme of moment distribution. Section A-A and B-B presents the cross sections of the beam at two locations indicated in the scheme.

After obtaining the bending moment value at the location of the cope, and knowing that the bending moment at the support of a simply supported beam is equal to 0 kNm, the complete bending moment diagram for the beam has been illustrated. From this diagram, the moment values at the load application point M_1 have been obtained, see equation 4.3.

$$M_1 = \frac{M_3 l_1}{l_3} = \frac{17kNm * 1.835m}{0.23m} = 136kNm \tag{4.3}$$

Furthermore, the load that needs to be applied in the middle of the beam has been calculated by using equation 4.4, where l is the span of the simply supported beam. With this calculation, all necessary loading information for the FE-model has been obtained.

$$F = \frac{4M_1}{l} = \frac{4 * 136kNm}{3.67} = 148kN \tag{4.4}$$

To complete the story of how the applied load was measured during the laboratory tests, forces at the strain gauge location needed to be investigated. Strain gauges were used to monitor the load application during the laboratory tests and to ensure correct stress values at the cope [67]. They were placed on the top and bottom flanges of the beam 720 mm away from the cope line. This location was chosen to register the strains with the least disturbing influence from the point load and the support. Therefore, the moment values at the strain gauge location M_2 have also been obtained from the moment diagram, see equation 4.5.

$$M_2 = \frac{M_3 l_2}{l_3} = \frac{17kNm * 0.720m}{0.23m} = 53kNm \tag{4.5}$$

The determination of the strains is similar as the method described above but includes the Hook's law to determine the strains from the stresses, see equation 4.6 and 4.7.

$$\sigma_2 = \frac{M_2 y_2}{I_2} \tag{4.6}$$

$$\epsilon_2 = \frac{\sigma_2}{E} \tag{4.7}$$

In [67] it is defined that the stress range at the location of the cope hole differed per test between 40, 50, and 70 MPa. Following the same analogy as above, the forces applied at the middle of the beam were determined to reach the desired stress range at the location of the cope.

The beams were cyclically loaded until complete failure due to fatigue crack propagation.

4.1.2. Laboratory test results

Results of the crack propagation phase have been obtained by manually measuring length of the crack at convenient intervals and have been presented by depicting the relation between the crack length and the number of load cycles. They have been grouped in three graphs to present the outcome of different cope cutting methods (figure 4.2); the different radius of the cope (figure 4.3) and different stress ranges (figure 4.4). Similar as in section 3.1, the exact numbers of load cycles or the length of the crack have not been mentioned in the laboratory test report [67]. Approximate numbers have been extracted from the graphs from figure A.9 to A.11, see appendix A, and the new data has been presented in figure 4.2, 4.3 and 4.4.

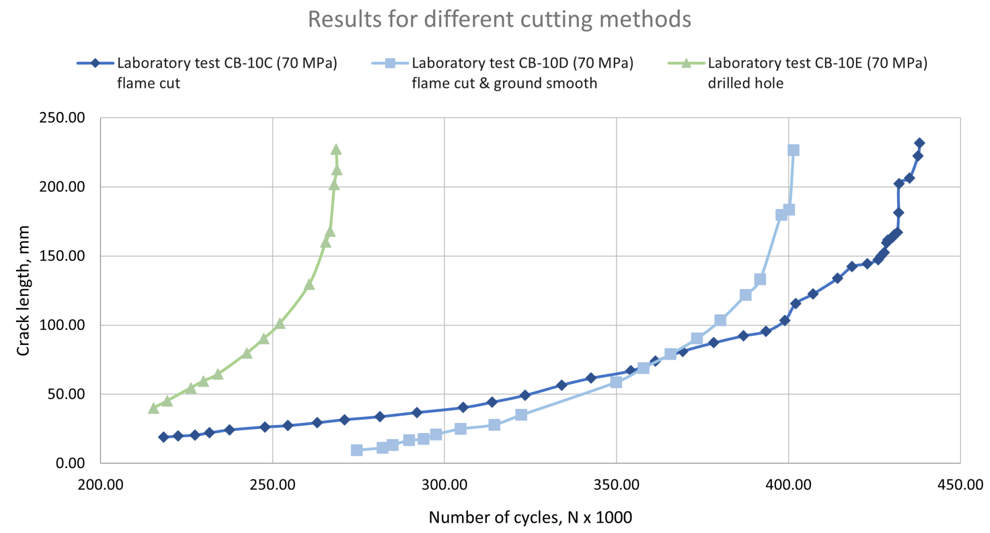

Figure 4.2: Crack length dependency of the number of the load cycles for different cope cutting methods [67].

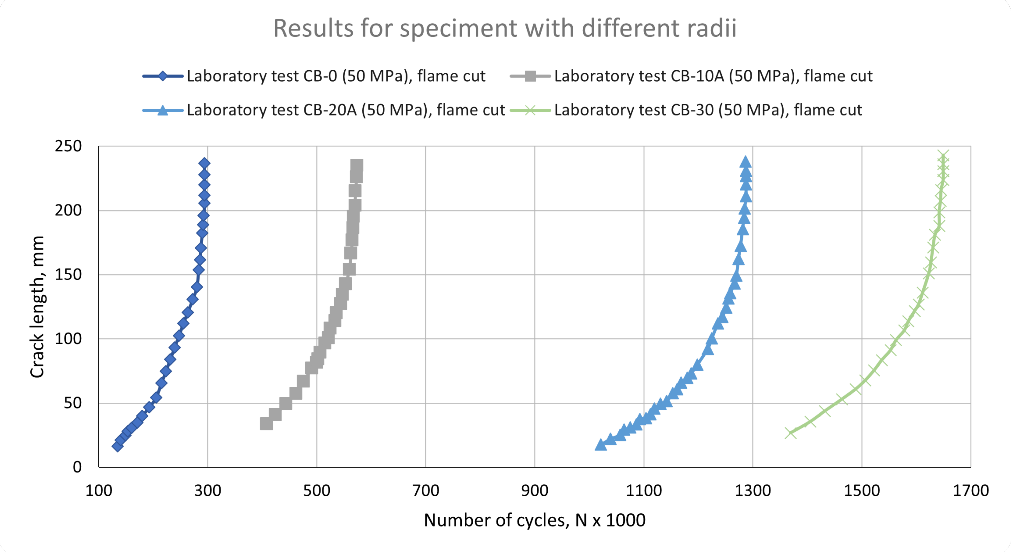

Figure 4.3: Crack length dependency of the number of the load cycles for different cope radius of the cope [67].

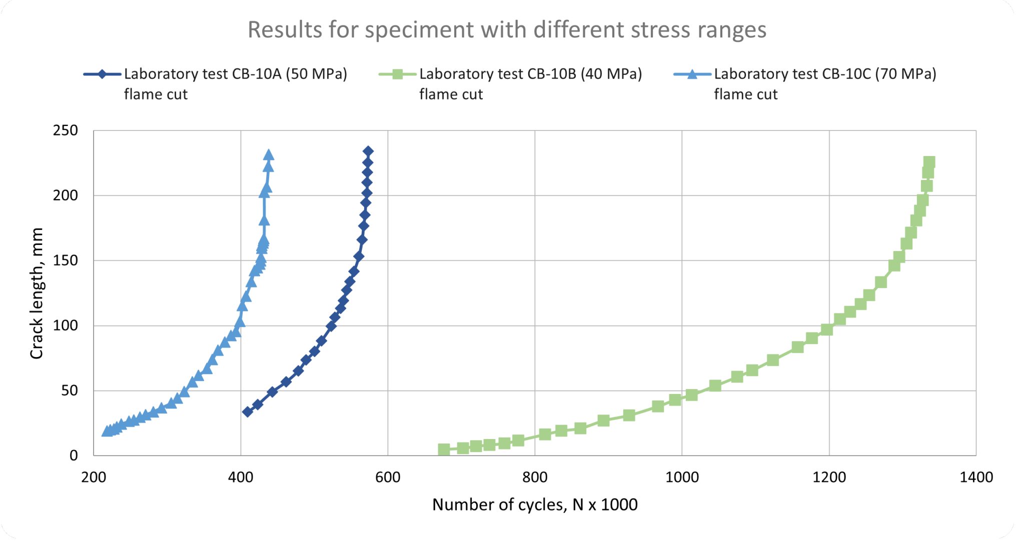

Figure 4.4: Crack length dependency of the number of the load cycles for different stress ranges [67].

Unfortunately, the path of the crack propagation was not registered during the testing in the laboratory and remains unknown. Only a few low quality pictures as shown in figure 4.5 have been presented in the laboratory test report that can not be used for detailed analysis.

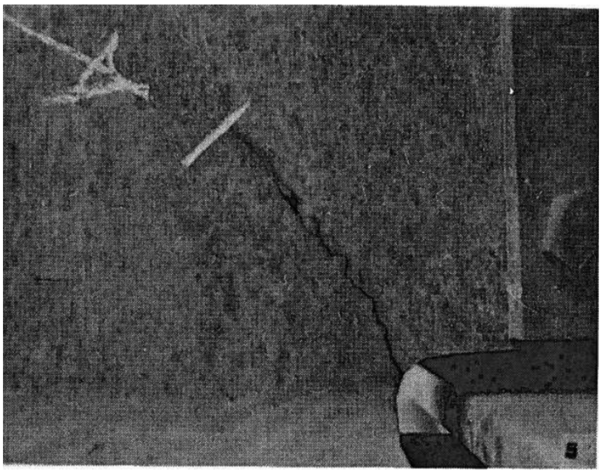

Figure 4.5: Path of the crack propagation [67].

4.2. Transition from crack initiation model to propagation model

In chapter 3 the crack initiation model was introduced and delivered reliable results for the location of the crack initiation. In this section, this statically loaded crack initiation model has been modified to replicate the laboratory test described in section 4.1 and to perform crack propagation analysis with cyclic loading. The transition from a statically loaded crack initiation model to a crack propagation model with cyclic loading includes multiple essential changes that will be described in this section.

Results for the laboratory tests in section 4.1 were obtained for three types of stress ranges, 40 MPa, 50 MPa, and 70 MPa, but the crack propagation analyses have only been investigated for the test with the highest stress range of 70 MPa to sharpen the scope. In a similar manner, only one size of radius of the cope has been analysed. The size of a 10 mm radius has been chosen based on the findings from the laboratory test described in section 3.1 stating that a smaller radius of the cope leads to higher stress concentrations and is therefore more prone to crack initiation.

The following sections describe different aspects of the crack propagation model.

Initial crack

First, a separate part has been modelled to represent the initial crack from which the propagating crack would further grow. This part has been modelled as a 3D extruded shell. This extruded part has been added to the assembly and has been located 7.09 mm away from the cope line based on the results from the crack initiation model for the 10 mm cope radius presented in table 3.15. Orientation of the part has been based on observations from the laboratory test [67] when the crack was propagating with a 35 degree angle from the vertical. An initial crack size of 8 mm x 10 mm (width through thickness x length) has been chosen, and the crack plane additionally sticks 2 mm out of the model at all three sides of the web as has been recommended by multiple authors [32, 34, 38]. Implementation of the recommendation leads to the final geometry of the initial crack part of 12 mm x 12 mm, see figures 4.6 and 4.7.

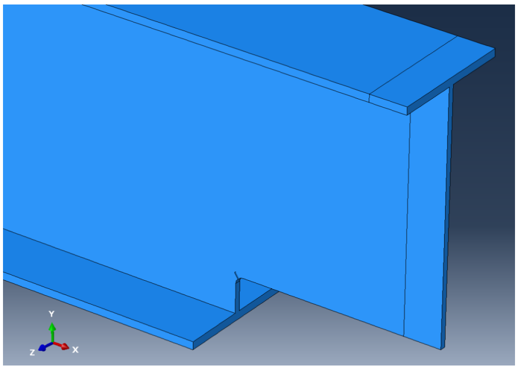

Figure 4.6: Initial crack in the assembly.

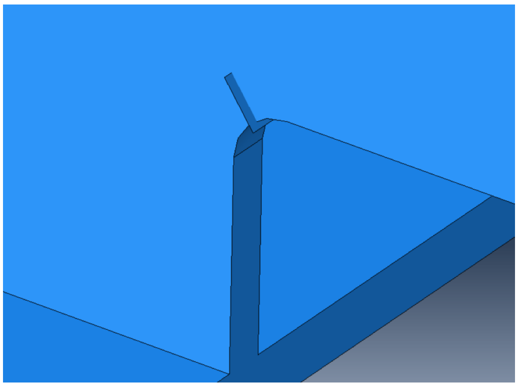

Figure 4.7: Initial crack zoomed in.

XFEM crack

After the initial crack has been successfully modelled with preferable dimensions and orientation, the crack has been assigned as XFEM crack with certain contact properties between the initial crack and the web of the beam. Contact properties have been created under the Interaction Property Manager in the Interaction module in Abaqus. Contact property allows to define the fracture criterion based on which the crack will propagate through each of the mesh elements. The chosen fracture criterion VCCT is described in section 2.4.1. The direction of crack growth has been analysed with the maximum tangential stresses as introduced in section 2.4.2 and the mixed mode behaviour has been captured with the Power law as described in section 2.2.3. Critical energy release rates for modes I, II, and III have been assigned to be $G_I = G_{II} = G_{III} = 100$ and the exponent parameters for the mixed mode behaviour have been assigned to be $a_m = a_n = a_o = 1$.

Once the contact properties have been created, the initial crack can be assigned to propagate as XFEM crack through the web based on the contact properties by selecting Special/ Crack/ Create. Important condition for the crack to propagate is the box that needs to be ticked to allow the crack growth. Without this setting, the analysis on a stationary crack will be performed.

Periodic loading

When performing the loading condition transition from the crack initiation model to crack propagation, first, the 100 kN loading used in section 3.2.1 needs to be changed. Laboratory tests for crack propagation kept the nominal stress at 70 MPa at the cope. Load that would guarantee this condition in the FE-model has been calculated in section 4.1.1 and therefore a loading of 148 kN has been applied as a distributed load over a 100 x 100 mm area.

Furthermore, the transition from the crack initiation model to the crack propagation model includes the change of the loading type from static loading to cyclic loading. The step module in Abaqus needs to be changed from ”Static, General” to ”Direct cyclic”. This change enabled the possibility of using low-cycle fatigue analysis described in section 2.4.1. With this option, it is possible to analyse a model with applied periodic loading with a certain number of cycles, while still performing static stress analysis instead of a more complicated dynamic stress analysis.

Once the cyclic loading has been enabled by changing the step module, a sinusoidal loading amplitude can be created in Abaqus to implement the stress range of 70 MPa. A stabilized response is obtained for the structure by using the Fourier series in combination with time integration of the nonlinear material behavior [14]. This is the most appropriate approach in Abaqus when the goal is to obtain a graph of the number of cycles versus the crack length based on the Paris law, described in section 2.2.2. When assigning a periodic amplitude, Fourier series equation 4.8 [56, 61] can be used, where a is the amplitude, A_0 is the initial amplitude, N is the number of terms, ω is the circular frequency, t is time, t_0 is the starting time, and A_n and B_n are the amplitudes for cos and sin function respectively.

$$a = A_0 + \sum_{n=1}^{N} [A_n cos n\omega(t - t_0) + B_n sin n\omega(t - t_0)] \tag{4.8}$$

For the cyclic loading applied in this test, the amplitude has been assigned by using $N = 1$ as only one loading cycle has been created, by having $A_n = 0$ to create the sinusoidal loading amplitude and by having circular frequency equal to $\omega = 2\pi$ to account for one cyclic loading. No initial amplitude has been assigned ($A_0 = 0$). However, this periodic loading will fluctuate on top of the previously implemented 148 kN loading that ensured 70 MPa nominal stress at the cope. This loading can be considered as an arbitrary initial amplitude and in the plot of the amplitude by Abaqus in figure 4.8 has the magnitude equal to 1. If the 70 MPa nominal stress at the cope is represented with a magnitude of 1, then to achieve the stress range of 70 MPa the load needs to fluctuate from a magnitude of 0.5 to 1.5 (from 35 MPa to 105 MPa). Sinusoidal amplitude of Fourier series has been set to vary between these limits by assigning the coefficient B_n equal to 0.5.

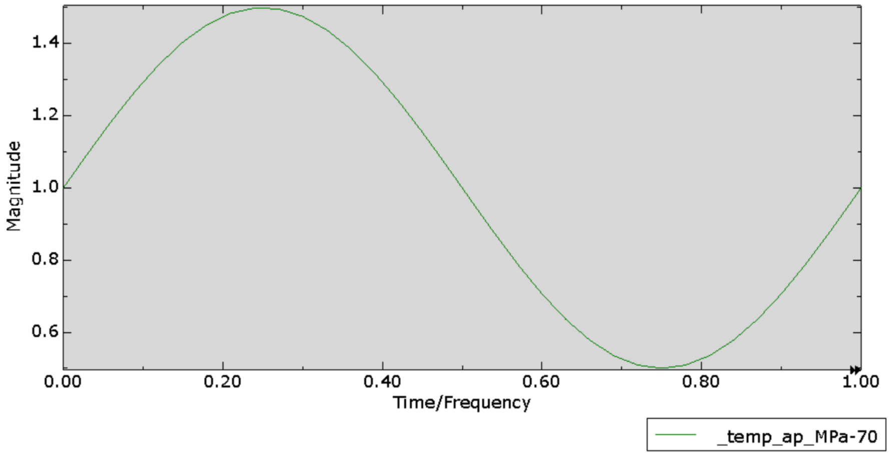

Figure 4.8: Applied loading amplitude of 70 MPa starting from 70 MPa nominal stress.

Load application by using amplitude has been chosen to be able to visualize the cyclic loading in the result tab and make sure that the model is undergoing the intended loading. However, this model is linear and no plasticity occurs, therefore, a simple point load could have also been modelled and repeatedly applied to simulate the cyclic loading.

Paris law parameters

For the crack to propagate through the web, there are two fracture criteria that need to be assigned. The first criterion is the VCCT criterion for the fracture of each of the elements. It was already assigned when defining the XFEM crack.

The second criterion, called Paris law, determines the rate at which the crack would propagate through the elements. Theory about this criterion was described in section 2.1.2 and the crack growth rate was expressed by equation 2.2. Abaqus software uses a different notation for this equation and expresses C and m coefficients with different constants c_3 and c_4, see equations 4.9, 4.10 and 4.11 [5, 15] where a is the crack length, N the number of cycles, ΔK the stress intensity factor, ΔG is the relative fracture energy release rate and E' is the Young's modulus from equation 2.25.

$$\frac{da}{dN} = C(\Delta K)^m = c_3(\Delta G)^{c_4} \tag{4.9}$$

$$c_3 = CE'^{m/2} \tag{4.10}$$

$$c_4 = m/2 \tag{4.11}$$

$$\Delta G = \frac{\Delta K^2}{E'} \tag{4.12}$$

To implement Paris law in the model, the coefficients c_3 and c_4 need to be predefined. It is not yet implemented in Abaqus to define these coefficients in the user interface, but it can be done through the keywords of the program. Keywords is the location where all actions performed while modelling the structure are being saved and can be viewed under the Model tab and the Edit Keywords option. Not only the keywords save the actions requested during the modelling, but they also allow to script these actions straight into the keywords sheet. This option allows to script additional lines in the keywords and include the c_3 and c_4 coefficients that are essential for the XFEM to propagate through the web of the beam. Lines that have been added to the keywords under the interaction properties section contain the following information [32]:

```
*Fracture Criterion, type=fatigue, mixed mode behavior=POWER
<c1>,<c2>,<c3>,<c4>,<r1>,<r2>,<GIc>,<GIIc>
<GIIIc>,<eta1>,<eta2>,<eta3>
```

Nominal values for the coefficients $C = 3.98 * 10^{-13}$ and $m = 2.88$ have been chosen from the British standard [57] and have been kept constant through all models to make comparisons between the results without the influence of the Paris law. Corresponding coefficients that have been implemented in the model are $c_3 = 1.717622715 * 10^{-5}$ and $c_4 = 1.44$.

Meshing

When using XFEM for crack propagation, it is required to assign linear mesh elements. This requirement has been already fulfilled in section 3.2.2 when creating the crack initiation model and using the 8-node linear brick elements C3D8. Therefore, no changes of the element type need to be made.

Topology of the mesh was initially kept the same as for the crack initiation model where a quarter of the spiderweb-like mesh has been used to mesh the area next to the cope, see figure 4.9.

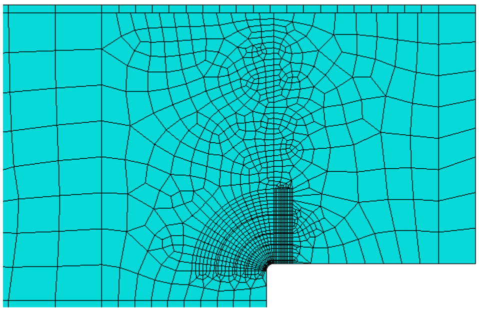

Figure 4.9: Combination of the spiderweb like mesh and the unstructured mesh.

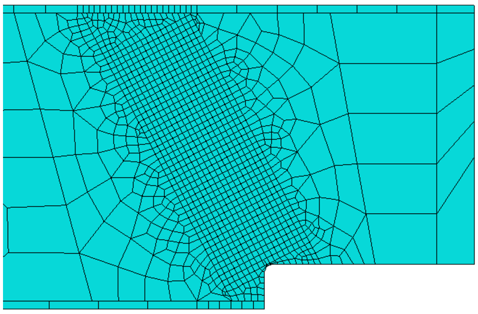

Figure 4.10: Structured mesh perpendicular to the initial crack.

However, when plotting the result of crack length dependency on the number of loading cycles for a model with the spiderweb-like mesh, it was obtained that the curve flattened at a crack length of ca. 200 mm, resulting in a shift in the number of cycles of ca. 50.000. These results are presented in figure 4.11 with the blue curve. The crack length where the curve flattens coincides with the location where the mesh topology changes from the spiderweb-like mesh to the unstructured mesh, therefore such a change needs to be avoided. To solve this influence on the crack propagation, a zone with a structured mesh perpendicular to the initial crack has been created (see figure 4.10). The grey curve in figure 4.11 shows that this change to a consistent mesh topology has improved the results, leading to a more fluid curve.

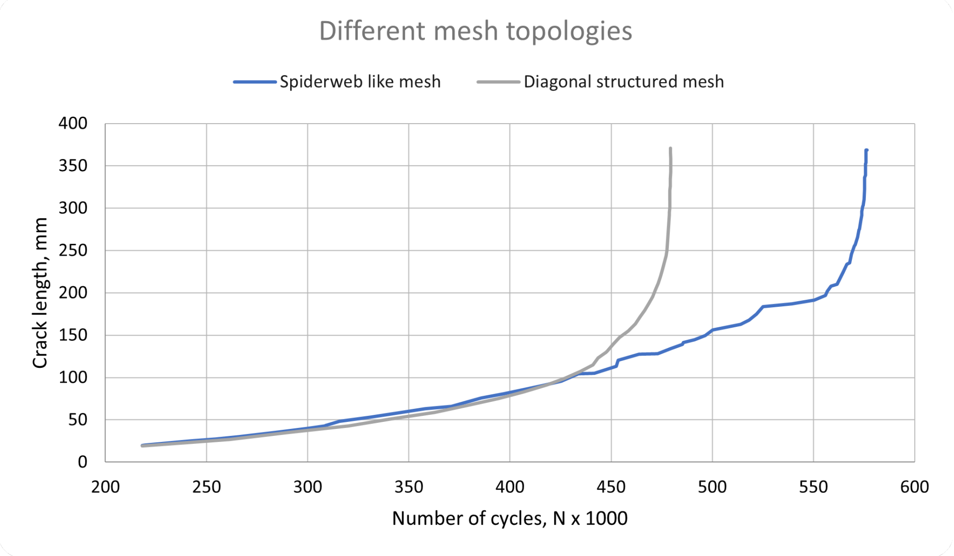

Figure 4.11: Crack length dependency of the number of loading cycles when spiderweb like mesh and a diagonal structured mesh has been used.

Additionally, this rectangular zone has been modelled as a separate part connected to the rest of the beam with tie constraints. This division has allowed to assign more elements through the thickness for the rectangular part (see figure 4.10) while keeping one element through the thickness for the rest of the beam, and therefore avoid a large increase of the number of elements for the whole model.

Results

Another difference between the crack initiation and the crack propagation model is the procedure to obtain results. For the crack initiation, longitudinal stresses were the necessary output. Abaqus contains a well-developed output for stresses where results can be both visualized and quantified.

When investigating crack propagation, the main data that needs to be obtained from the software is the crack length dependency on the number of loading cycles. There is an available output for half of the necessary information which is the number of load cycles per incremental crack growth that can be found under Results/ Step/ Frame tab.

However, when using XFEM method for crack propagation, Abaqus users face some difficulties when trying to obtain the incremental length of the XFEM crack. There is only one output available for the XFEM crack that can only visualise the crack path as shown in figure 4.12 and is called STATUSXFEM. The necessary incremental length of the crack can not be obtained also by measuring the length manually, as no coordinates of the crack path can be plotted. Abaqus' help-desk has suggested to either manually query the coordinates or do some scripting. However, only the coordinates of the mesh nodes can be queried.

While Abaqus is working on implementing an output for the incremental XFEM crack length, a temporary solution has been found and used in this thesis by using AutoCAD computer software and Microsoft Excel. Figure 4.13 shows the step-wise procedure performed in AutoCAD.

First, as only the mesh nodes can be queried in Abaqus, the coordinates of the mesh element nodes that have been affected by the XFEM crack have been replicated in AutoCAD, see the left part of figure 4.13. The next step, shown in the middle part of figure 4.13, has been to create screenshots from STATUSXFEM output containing the crack path and to place them in AutoCAD to match the mesh element node coordinates from the first step. This has been done to be able to perform the third step, presented on the right part of figure 4.13 which is to replicate the crack path in AutoCAD by drawing a polyline based on the crack path in the screenshots. By using LIST command, the coordinates of each increment of the path can be obtained and postprocessed in Microsoft Excel to obtain the incremental length of the XFEM fatigue crack.

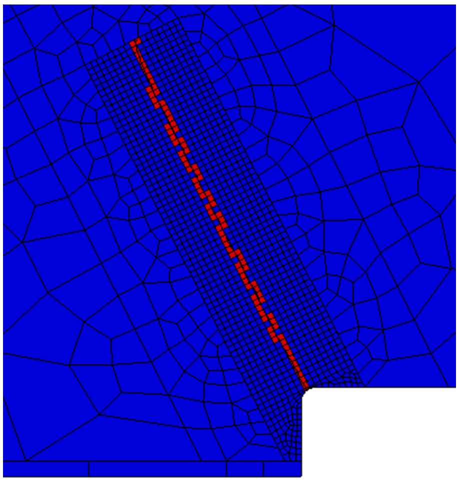

Figure 4.12: Visualization of the STATUSXFEM results from Abaqus.

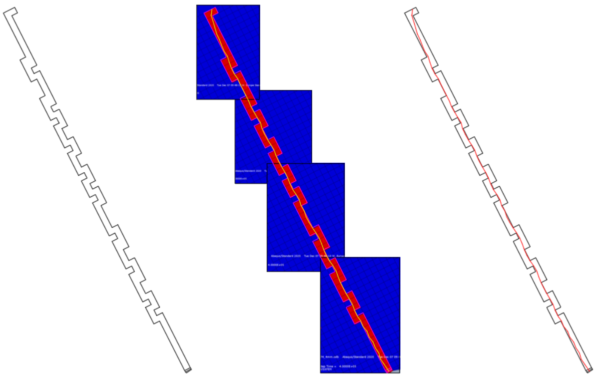

Figure 4.13: Procedure in AutoCAD to obtain incremental length of the XFEM crack:
left - coordinates of the mesh nodes
middle - alignment of the screenshots form STATUSXFEM output
right - obtained XFEM crack path

This postprocessing technique is a time-consuming procedure that requires manual work. Therefore, a higher possibility of inaccuracy in the results is obtained when compared to an automated procedure.

After obtaining the incremental length of the XFEM crack, crack length dependency of the number of loading cycles can be plotted. When using Abaqus data for the number of cycles, it does not include the loading cycles that are needed to initiate the crack, since the crack propagation analysis starts from the tip of the predefined initial crack. Therefore, additional loading cycles need to be added. Table 4.1 shows results from the laboratory test for a cyclically loaded coped beam CB-10C with a flame cut cope radius of 10 mm. These results have been used as the reference for the additional loading cycles that need to be added for the crack propagation analysis.

FE-models have been modelled with different initial crack sizes and in-plane mesh sizes, therefore, leading to crack paths that have different incremental growth. To account for this variate, table 4.1 contains four crack lengths from the laboratory tests and allows to choose the closest crack length in different FE-models to which the additional number of cycles have been added. After this adjustment, all data for presenting a graph of crack length dependency on the accumulated number of loading cycles have been prepared.

Crack length, mm	**Number of cycles, N x 1000**
18.95	274.53
19.87	282.03
20.50	284.04
24.29	285.00

Table 4.1: Number of cycles that are necessary to initiate a crack of a certain length [67].

4.3. SIF with stationary cracks

Chapter 4.2 presented many changes that need to be implemented in the crack initiation model for the transition to crack propagation model. These procedures present the complexity of the model and emphasize the importance of sub-question 2 where investigation of the most dominant parameters has been required. Section 4.3 and 4.4 present the parameters investigated during this thesis and quantify the variety that they create, and therefore answer sub-question 2.

One of the dominant parameters is the SIF. When looking at the Paris law (equation 2.2), the crack growth rate depends on three parameters, being the C and m coefficients, and the SIF. As stated in section 4.2, C and m coefficients have been set constant for all models in this thesis. Therefore, the only variable in this Paris law equation that influences the crack growth rate and therefore the crack propagation is the SIF.

To ensure that the crack propagation is being modelled correctly, SIFs have been obtained for the stationary cracks when using XFEM. Additionally, the comparison with two well-known methods, VCCT and J-integral, has been made to determine the variation in the results of these three methods.

4.3.1. SIF with XFEM

When creating the crack propagation model described in section 4.2, under Interaction module, it is important to select the option Special/ Crack/ Create that allows the crack to grow. This option, however, excludes the SIF output since this output is available only for stationary XFEM cracks. To compute a SIF with XFEM, a separate model for stationary crack analysis has been created.

First, a crack propagation analysis has been performed with a 5 mm in-plane (structured) mesh size, two elements through the thickness, and an 8 mm long initial crack to obtain the path of the crack. By postprocessing the results through AutoCAD, as described in section 4.2, coordinates of each incremental step of crack growth have been found. Based on these coordinates, the originally modelled initial XFEM crack has been extended till a crack length of 50 mm, 100 mm, 150 mm, 180 mm, and 200 mm, as can be seen in figure 4.14.

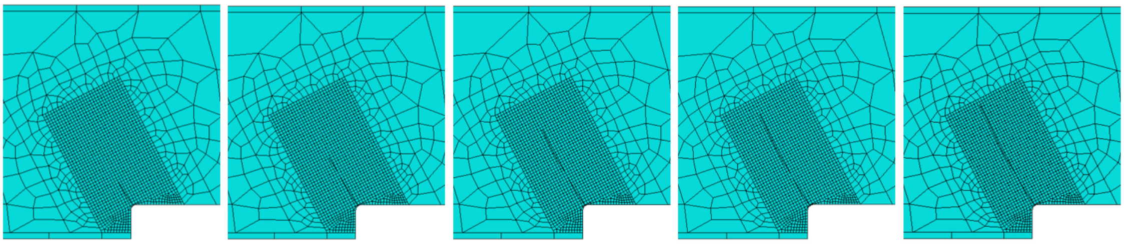

Figure 4.14: Stationary XFEM cracks with 50 mm, 100 mm, 150 mm, 180 mm and 200 mm length.

Furthermore, a direct cyclic loading analysis, described in section 4.2, has been performed for each of these five stationary crack lengths and the SIF at the crack tip has been obtained from the Data File. An example of the SIF output from Abaqus can be seen in figure 4.15 and the way how to subtract the necessary information from this SIF output is explained next.

From figure 4.15 it has been observed that the stress intensity factors for loading modes 2 and 3 are relatively small in comparison with mode 1. Therefore, this crack propagated in the dominant mode 1 (see figure 2.6). Columns 1 to 5 show that the SIF has been calculated from five contour integrals. From the example in figure 4.15, it can be seen that the first contour integral for loading mode 1 shows deviation from the rest of the results. This inaccurate first contour integral has been observed by various researchers [62] and is therefore neglected and only an average of the second till the fifth contour integral has been considered. Sections $XFEM\_1$, $XFEM\_2$ and $XFEM\_3$ present the SIF results for each element node through the thickness at the tip of the crack and an average of these results has been calculated.

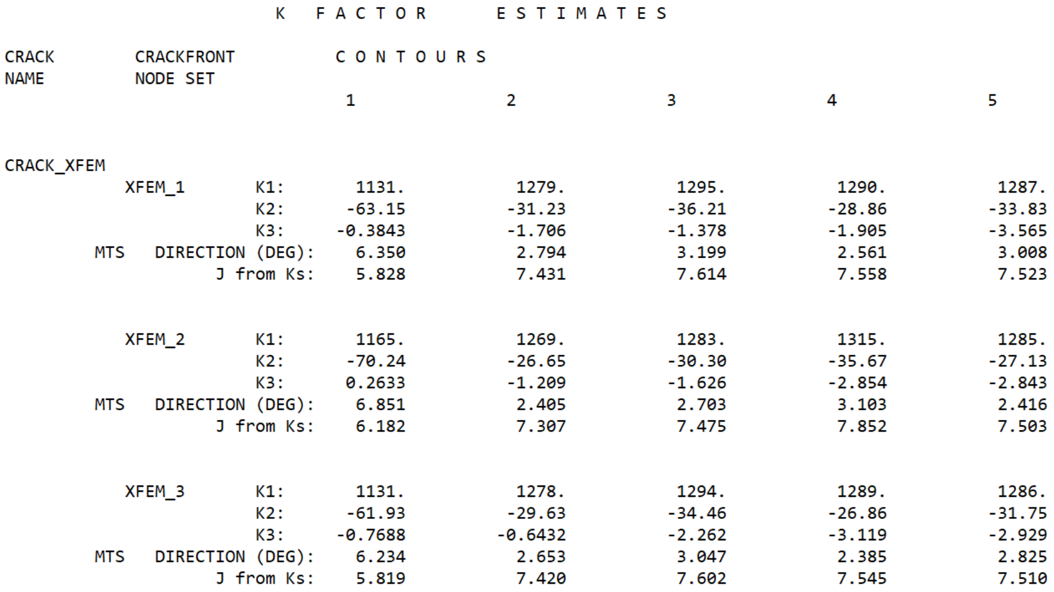

```
                          K   F A C T O R     E S T I M A T E S

CRACK        CRACKFRONT          C O N T O U R S
NAME         NODE SET
                                  1               2               3               4               5


CRACK_XFEM
            XFEM_1        K1:       1131.           1279.           1295.           1290.           1287.
                          K2:      -63.15          -31.23          -36.21          -28.86          -33.83
                          K3:     -0.3843          -1.706          -1.378          -1.905          -3.565
         MTS    DIRECTION (DEG):    6.350           2.794           3.199           2.561           3.008
                      J from Ks:    5.828           7.431           7.614           7.558           7.523


            XFEM_2        K1:       1165.           1269.           1283.           1315.           1285.
                          K2:      -70.24          -26.65          -30.30          -35.67          -27.13
                          K3:      0.2633          -1.209          -1.626          -2.854          -2.843
         MTS    DIRECTION (DEG):    6.851           2.405           2.703           3.103           2.416
                      J from Ks:    6.182           7.307           7.475           7.852           7.503


            XFEM_3        K1:       1131.           1278.           1294.           1289.           1286.
                          K2:      -61.93          -29.63          -34.46          -26.86          -31.75
                          K3:     -0.7688         -0.6432          -2.262          -3.119          -2.929
         MTS    DIRECTION (DEG):    6.234           2.653           3.047           2.385           2.825
                      J from Ks:    5.819           7.420           7.602           7.545           7.510
```

Figure 4.15: SIF output for 100 mm long stationary crack from the first set of in-plane mesh topology.

After the SIF has been subtracted from Abaqus, the stationary crack length dependency of the SIF has been plotted in figure 4.17. Results from the first set of stationary cracks show a sharp increase of the SIF at the crack length of 200 mm. By looking at the most right picture from figure 4.14, it was observed that the crack tip for the 200 mm stationary crack has been located very close to the end of the finely meshed zone. As the SIF has been calculated by using five contour integrals around the crack tip, but in this case only two of the integrals can be calculated within the finely meshed area, an inaccurate result of SIF at 200 mm crack length has been obtained.

This assumption of the cause of the SIF increase has been checked by two other sets of stationary cracks with modified in-plane mesh topology. A second dataset has been created with reduced width of the finely meshed area for 25 mm from the left side and 35 mm from the right side and with increased length of the finely meshed area for 50 mm. For the third set of stationary cracks, the width of this area has been reduced even further when an additional 10 mm has been removed from both the left and the right side of the finely meshed area. Adjustment of the in-plane mesh topology has been presented in figure 4.16 for the crack length of 200 mm.

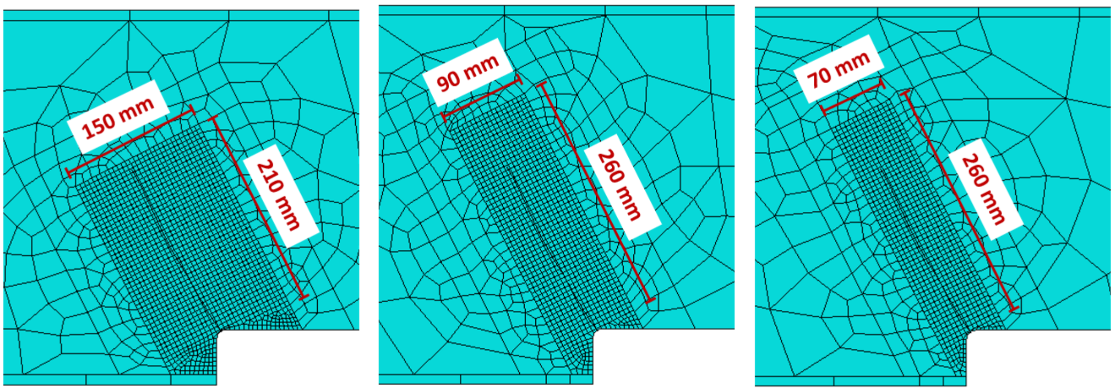

Figure 4.16: Stationary 200 mm long XFEM crack with different geometry of the fine mesh zone:
left - set one with wide and short zone
middle - set two with 25 mm and 35 mm narrower and 50 mm longer zone
right - set three with 20 mm narrower zone zone than in the middle figure

From figure 4.17 it has been concluded that the extension of the finely meshed zone has improved the results and a gradual increase of the SIF is now being obtained for the second and the third set of in-plane mesh topologies. Therefore, when modelling stationary cracks with XFEM method, it is important to have at least five fine size mesh elements around the crack tip when evaluating five contours for accurate SIF estimation.

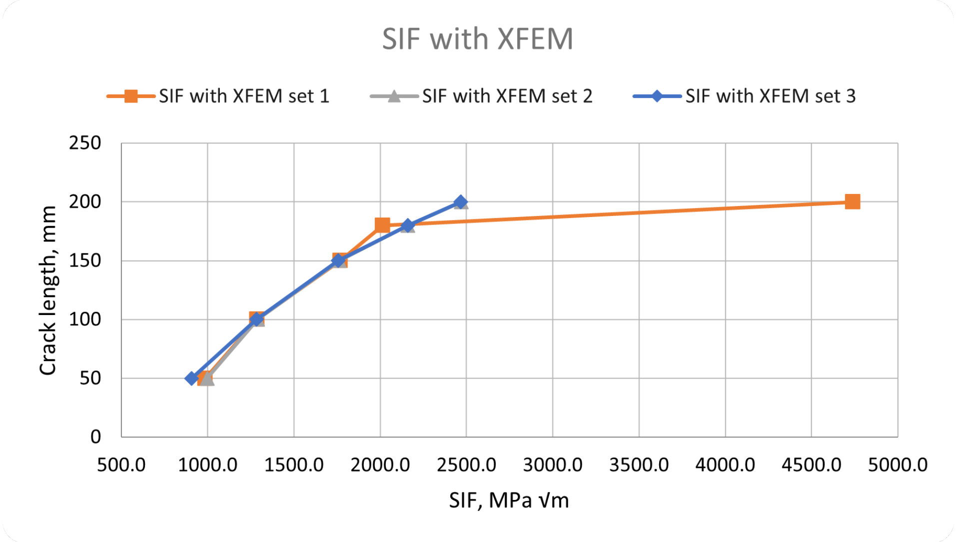

Figure 4.17: Results of SIF by using XFEM method for three different in-plane mesh topologies visualized in figure 4.16.

4.3.2. SIF comparison with different methods

In this section, the results from mesh topology set 2 have been compared with two other well-known methods, J-integral and VCCT. With this comparison, it can be shown that the SIF's found using all methods are similar and all methods can thus be used.

Both methods, J-integral and VCCT, have been applied to set one of the mesh topologies from figure 4.16 with in-plane mesh size of 5 mm, two elements through the thickness, and an 8 mm long initial crack. At this moment in the research, only results from set 1 of XFEM were performed, and the inaccuracy of this set was yet unknown. However, already from set 1 results for J-integral and VCCT methods conclusions were made, therefore, the analysis with sets 2 and 3 has not been performed.

For both methods, adjustments to the Abaqus model need to be implemented and these changes are described in the upcoming subsections.

J-integral

J-integral does not require a separate part in the assembly to define the crack path as in the XFEM method. Instead, the obtained crack path from the propagation analysis has been implemented as the partition of the finely meshed zone. Partitioning is a function in Abaqus that allows dividing parts into regions. Additionally, rings of 5 mm radius have been partitioned at the tip of the stationary cracks, as can be seen in figure 4.18, to indicate the region of the first contour integral. All partitions have been performed through the thickness of the web. Same as for the XFEM method, the crack length of 50 mm, 100 mm, 150 mm, 180 mm, and 200 mm has been modelled.

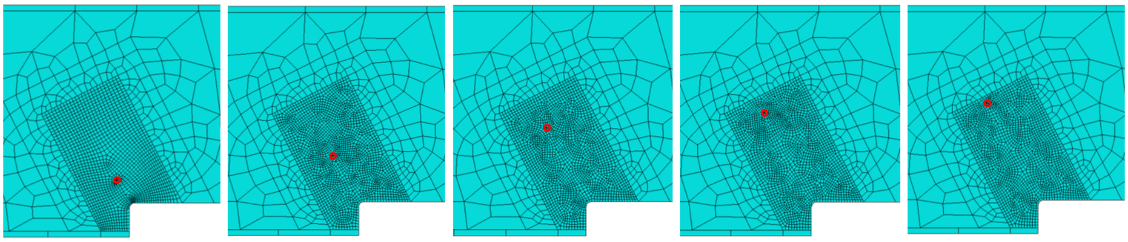

Figure 4.18: Stationary J-integral cracks with 50 mm, 100 mm, 150 mm, 180 mm and 200 mm length.

The crack type definition of contour integral has been set under the interaction module when creating the crack definition under Special/ Crack/ Create. The crack extension vector, that indicates the direction of further crack propagation, has been assigned to the q vector and aligns with the direction of the last increment of the crack path.

Values for the SIF have been obtained by using the same SIF output as for the XFEM method described in section 4.3.1 and the obtained SIF dependency on the length of the crack can be seen in figure 4.24.

VCCT

VCCT method can be applied when the crack path is created by two separate parts in Abaqus model. Therefore, coordinates of the crack path have been used to split the finely meshed zone into two parts, as can be seen in figure 4.19.

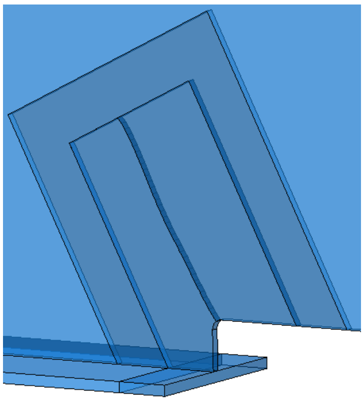

Figure 4.19: Finely meshed zone split in two separate parts.

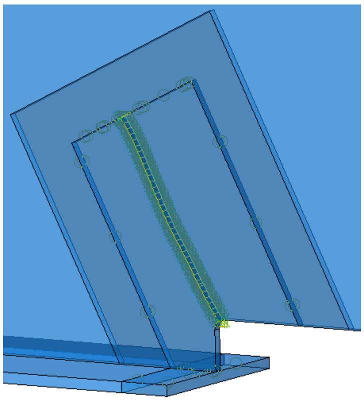

Figure 4.20: Interaction zone between the two new parts.

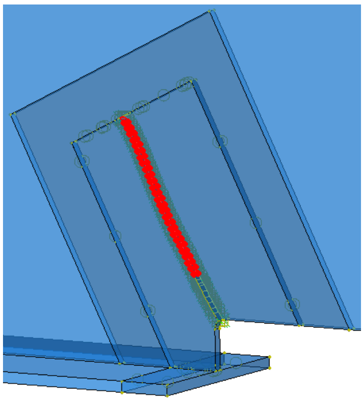

Figure 4.21: Bonded zone for 50 mm long stationary crack.

Previously defined tie constraints between the finely meshed zone and the rest of the beam have been revised to account for the newly created parts. At the location of the crack path, highlighted in figure 4.20, interaction between the two new parts has been assigned under Interaction Manager in Abaqus. Surface-to-surface interaction has been implemented by defining the master and slave surfaces and by applying VCCT fracture criterion between the parts.

To obtain a SIF for certain lengths of the crack, bonding has been assigned to the part of the crack path that needs to say bonded. Figure 4.21 shows an example of SIF determination for a 50 mm long crack where the rest of the crack path, marked in red, has been assigned to stay bonded.

Same as for XFEM and J-integral methods, the analysis of 50 mm, 100 mm, 150 mm, 180 mm, and 200 mm long stationary cracks has been performed.

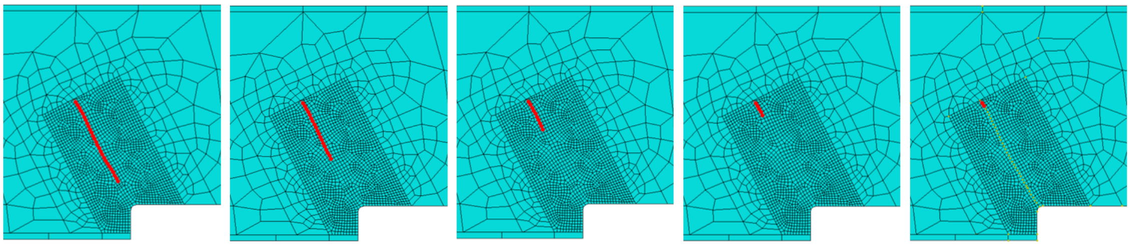

Figure 4.22: Stationary VCCT cracks with 50 mm, 100 mm, 150 mm, 180 mm and 200 mm length.

The SIF is not a direct output in Abaqus, however, ENRRT field output has been used to compute the strain energy release rate. By using equation 2.22 for loading mode I, a SIF has been calculated. Results can be seen in figure 4.24.

Comparison

After obtaining SIF's with three different methods, a comparison between them has been made. Figure 4.23 shows the results from all three methods when the first set of in-plane mesh topology has been applied. Good alignment can be observed for the crack length of 50, 100, and 150 mm. Only a small variation of 2.2% is obtained for the crack length of 50 mm. A large variation in results has been obtained for the crack length of 180 and 200 mm. However, it is known from section 4.3.1 that the results from XFEM are not reliable at these crack lengths.

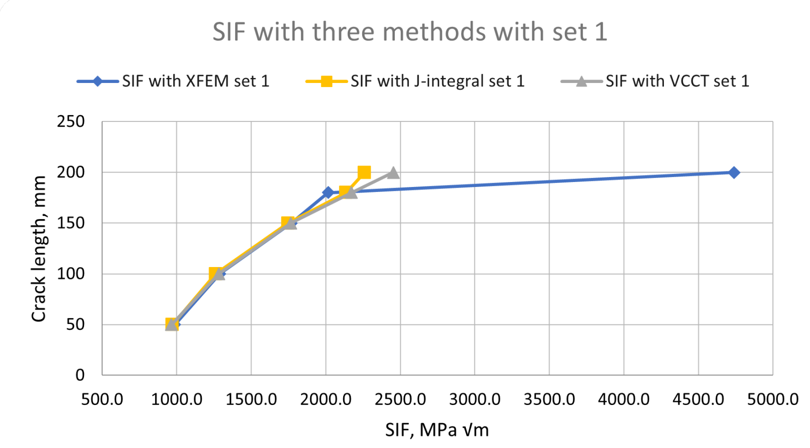

Figure 4.23: SIF comparison between XFEM, J-integral and VCCT method with the first set of mesh topology.

As stated in section 4.3.1, the results for SIF's with XFEM are more aligned with what is expected when using the second and third mesh topology. Therefore, in the previous comparison, the results from the XFEM method from the first set have been replaced with results from the second set of mesh topology, see figure 4.24. Analyses with J-integral and VCCT methods have been kept with the results from the first mesh topology, as it is already possible to draw conclusions from them. The comparison shows well-aligned results where only J-integral results for the crack length of 200 mm deviate from XFEM and VCCT results. The variation between the results at the crack length of 50 mm is 3.4% and 8.5% for 200 mm crack length.

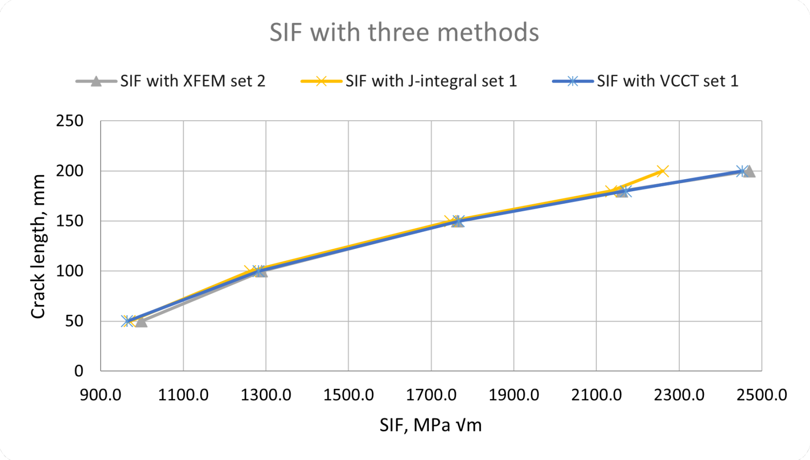

Figure 4.24: SIF comparison between J-integral, VCCT with the first set of mesh topology and XFEM with the second set.

This comparison has led to two conclusions. First, the XFEM method produces well-aligned results with the well-known J-integral and VCCT methods. And secondly, as the results from the XFEM method with the second set of in-plane mesh topology match the VCCT and J-integral results way better than when using the first set of mesh topology, it is recommended that, when evaluating five contours around the crack tip, at least five fine size mesh elements surround the crack path.

4.4. Mesh parameters

After the stationary crack analysis has shown a good comparison between the three methods, a study of the propagating crack has been performed to further investigate the most dominant parameters and their influence on the variability of the results.

Two sensitivity analysis, mesh sensitivity and initial crack size sensitivity analysis, have been performed and are described in section 4.4.1 and 4.4.2. Both of these analysis have shown a certain influence of mesh parameters on the variability of the results.

4.4.1. Mesh sensitivity analysis

Mesh sensitivity analysis is an often used verification procedure for the FE-model. When performing mesh sensitivity analysis, the mesh size is reduced stepwise, leading to a change in the number of cycles needed. At a certain point, further reduction of the mesh size does not lead to changes anymore. The gradual reduction of mesh size, presented in a graph showing the mesh size versus the number of cycles, is thus expected to have a parabolic decaying curve.

In this thesis, mesh sensitivity analysis has been performed on the second set of mesh topologies from figure 4.17, with an initial crack size of 8 mm. Mesh size has been varied both in plane and through the thickness at the same time. The performed variations have been gathered in table 4.2.

In-plane mesh size, mm x mm	Element size through the thickness, mm
8x8	8
6x6	8
5x5	4
4.5x4.5	4
4x4	4
3.8x3.8	2.7
3.6x3.6	4
3x3	2.7

Table 4.2: Variation of the in-plane and through the thickness mesh size for the mesh sensitivity analysis.

Results of the mesh sensitivity analysis have been presented in a graph for the crack length dependency on the number of cycles in figure 4.25. It was expected that the curve representing the largest size of the mesh would be placed on the right side of the graph, and the larger the decrease of the mesh, the further to the left the curve would shift.

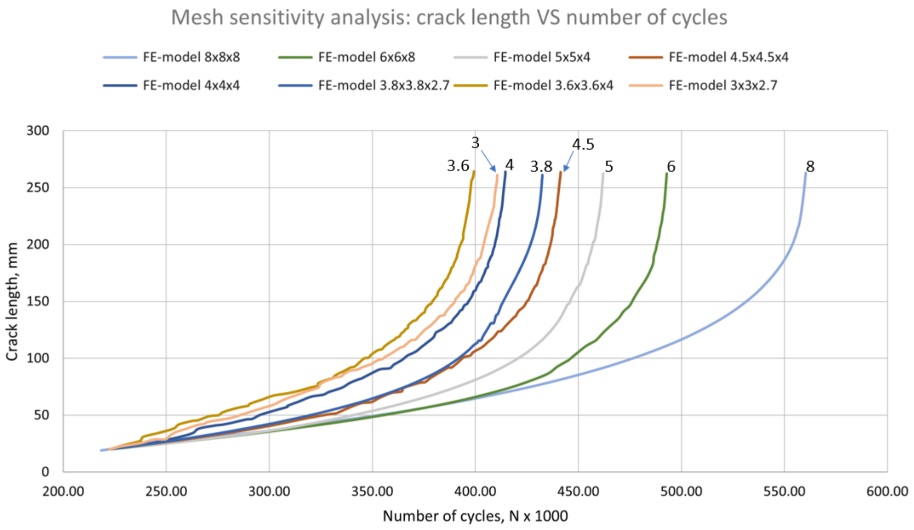

Figure 4.25: Mesh sensitivity analysis presented in crack length dependency on the number of cycles.

This expectation is true for a decrease up to 4.5 mm mesh size. However, the curve resulting from a mesh size of of 4x4x4 mm is placed more to the left than the curve belonging to a mesh size of 3.8x3.8x2.7 mm.

To have a better understanding of the convergence of the results, the in-plane mesh size has been plotted versus the number of cycles corresponding to a crack length of 200 and 250 mm in figure 4.26. It was expected to see a parabolic decaying curve. However, no parabolic shape has been observed and a decaying trend is present only for the mesh size from 8 to 4 mm.

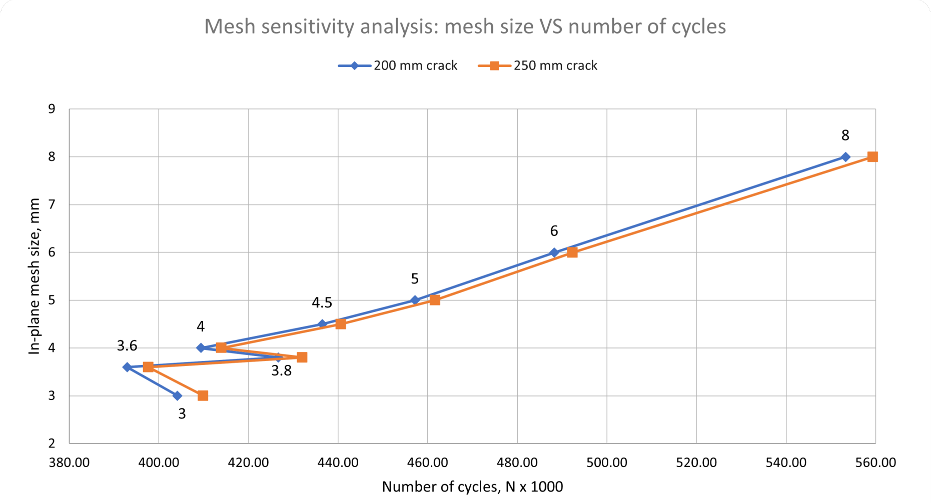

Figure 4.26: Mesh sensitivity analysis presented in in-plane mesh size dependency on the number of cycles.

However, a different observation has been made when dividing the data in results for a certain number of elements through the thickness. Results for two elements through the thickness have been presented in figure 4.27. The expected parabolic shape is not visible, however, a decreasing trend has been observed. Similar results have been obtained when plotting the results for one and three elements through the thickness, but the slopes of the trend lines are different.

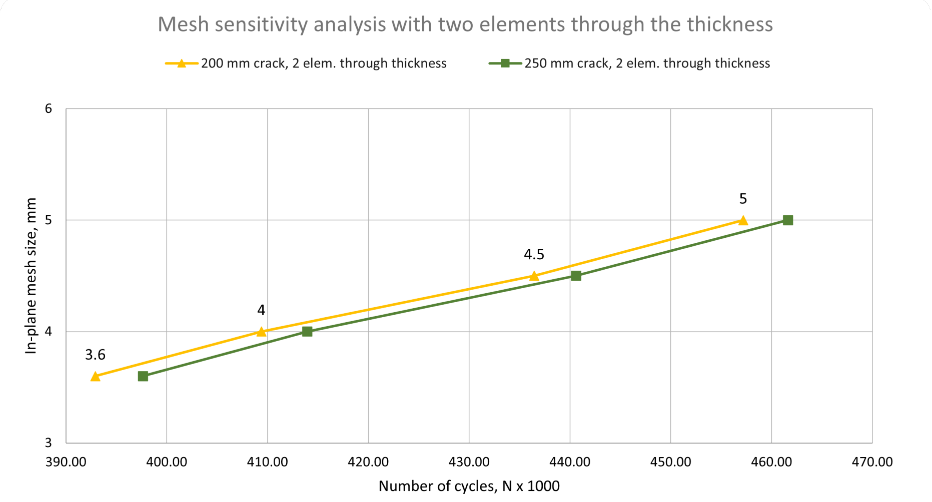

Figure 4.27: Mesh sensitivity analysis results for the models with two elements through the thickness.

To conclude section 4.4.1, the expected mesh convergence has not been obtained. However, a linear trend with different slopes has been obtained for models with matching number of elements through the thickness. As the decaying trend was observed until the in-plane mesh size of 4 mm and a clear linear relation has been observed with the two elements through the thickness, further sensitivity analysis has been based on a model with 4x4x4 mm mesh size.

4.4.2. Initial crack size sensitivity analysis

For the first crack propagation model, the initial crack was modelled to be 10 mm long, from which 2 mm was located outside of the web of the beam, leaving only 8mm for the initial crack in the beam. More detailed explanation can be found in section 4.2. However, way smaller initial cracks can be detected nowadays with advanced technologies. To check the applicability of the model for different sizes of the measured crack, it was decided to perform an initial crack size sensitivity analysis.

Initial crack size sensitivity analysis has been based on the model from the mesh sensitivity analysis in section 4.4.1 with the in-plane mesh size of 4x4 mm and two elements through the thickness. This choice has been based on section 4.4.1, figure 4.26 where the expected decaying trend for the mesh sensitivity analysis was observed until the mesh size of 4 mm. Initial crack size has been varied between 2 and 8 mm and the results (crack length versus number of cycles) can be seen in figure 4.28.

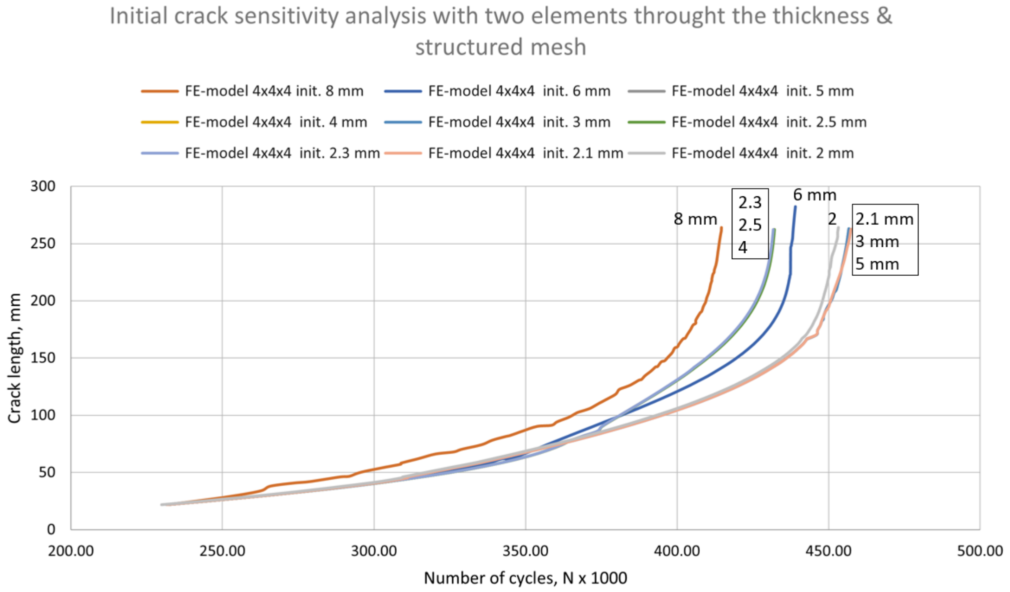

Figure 4.28: Number of cycle dependency on the crack length for different initial crack sizes with two elements through the thickness and parallel mesh topology.

Figure 4.28 shows an unexpected variation in results for the relation between the crack length and the number of cycles when different initial crack lengths have been modelled. Two distinct bundles of results have been observed for the initial crack size of 2, 2.1, 3, 5 mm and 2.3, 2.5, 4 mm. All results vary by 9.9% for the crack length of 50 mm and by 10.0% for the 200 mm crack.

Further sections describe the attempts to reduce the variation between the results by changing two mesh parameters, being the number of elements through the thickness and the mesh topology (unstructured mesh topology instead of parallel mesh topology).

Number of elements through the thickness

When searching for possible improvements of the model, to reduce the variation in the initial crack size sensitivity analysis results, the crack path has been investigated, as can be seen in figure 4.29. It was expected to see an incremental growth of the crack with changes in the direction of the path only at the boundaries of the mesh elements. However, changes of the path's direction have been found within the element boundaries. This change has created kinks in the crack path that can be seen in the left and middle part of figure 4.30.

When looking at figure 4.28, a pattern between the location of the curve and the size of kinks has been discovered. The most right located curves are for the initial crack size of 2.1, 3, 5, and 2 mm. The crack paths for these results contain large kinks with a sharp change of the crack propagation angle as shown in the left part of figure 4.30. The crack path of the model with an initial crack of 6 mm only has a medium size kink. Small kinks, as visualized in the middle part of figure 4.30, have been observed for the crack paths of the results with 2.3, 2.5, and 4 mm initial cracks, indicating one of the bundles of results in figure 4.28. The crack path of the model with an 8 mm initial crack contains no kinks as shown in the right picture of figure 4.30, and its curve is located the most left in figure 4.28. The observed pattern shows that the smaller the kinks that are present in the crack path, the more to the left the curve of the number of cycles versus crack length is.

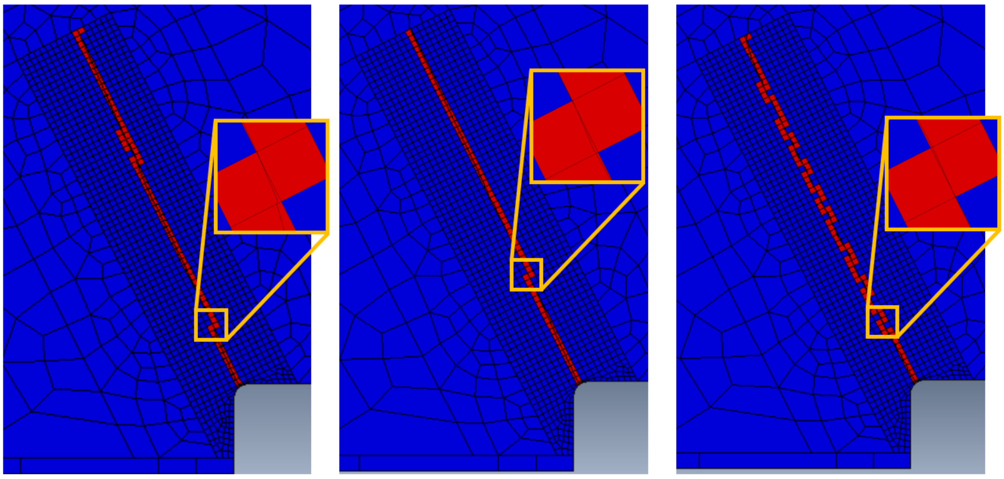

Figure 4.29: Visualization of the crack paths with locations of images from figure 4.30
left - crack path for FE-model with 2.1 mm initial crack
middle - crack path for FE-model with 2.3 mm initial crack
right - crack path for FE-model with 8 mm initial crack.

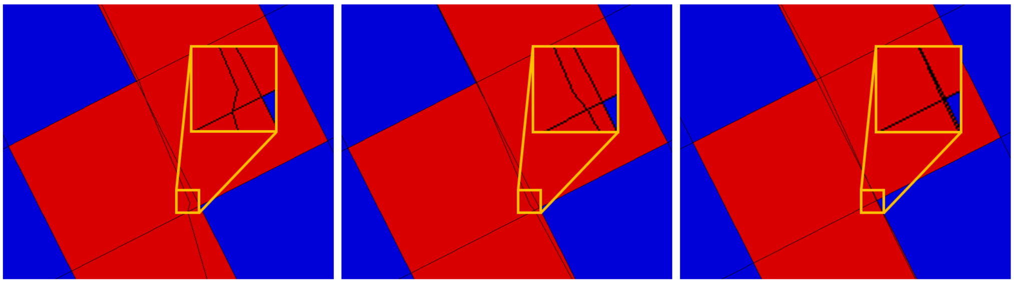

Figure 4.30: Visualization of the kinks within an element boundaries
left - large kink at 45 mm long crack from 2.1 mm initial crack path
middle - small kink at 45 mm long crack from 2.3 mm initial crack path
right - no kink at 45 mm long crack from 8 mm initial crack path.

When investigating the exact locations of the kinks, it has been observed that one location matches with the 45 mm crack length in figure 4.28 and 4.31, where eight of the nine curves stop having a matching result and start to deviate, and another location matches with the 170 mm crack length, where the bundle with results from 2.1, 3, and 5 mm initial crack size starts to spread. These locations and kinks are presented in figure 4.31.

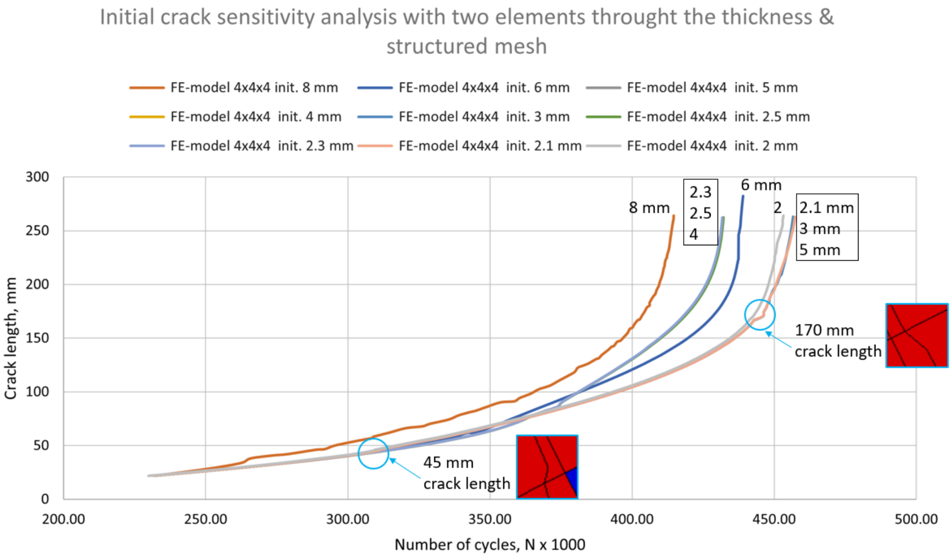

Figure 4.31: Location and visualization of the kinks:
first kink at 45 mm crack length
second king at 170 mm crack length.

When searching for the possible origin of kinks in the crack paths, a clear cause has not been found by looking only at the initial crack size sensitivity analysis. To have more data to base the assumptions on the crack paths from the mesh sensitivity analysis have been looked at. Conclusions of section 4.4.1 indicated that different number of elements through the thickness causes a different trend line. A similar relation has been found when looking at the crack paths: more kinks have been observed for the models with more elements through the thickness.

Based on this observation, it was expected that by reducing the number of elements through the thickness from two to one element for the initial crack size sensitivity analysis, the variation in the results would decrease. Figure 4.32 shows the results of the initial crack size sensitivity analysis for the in-plane mesh size of 4x4 mm and one element through the thickness. It can be seen that the variation of the results has decreased for the crack lengths above 100 mm and there are only three separate result branches while there were five before when analysis with two elements through the thickness has been performed.

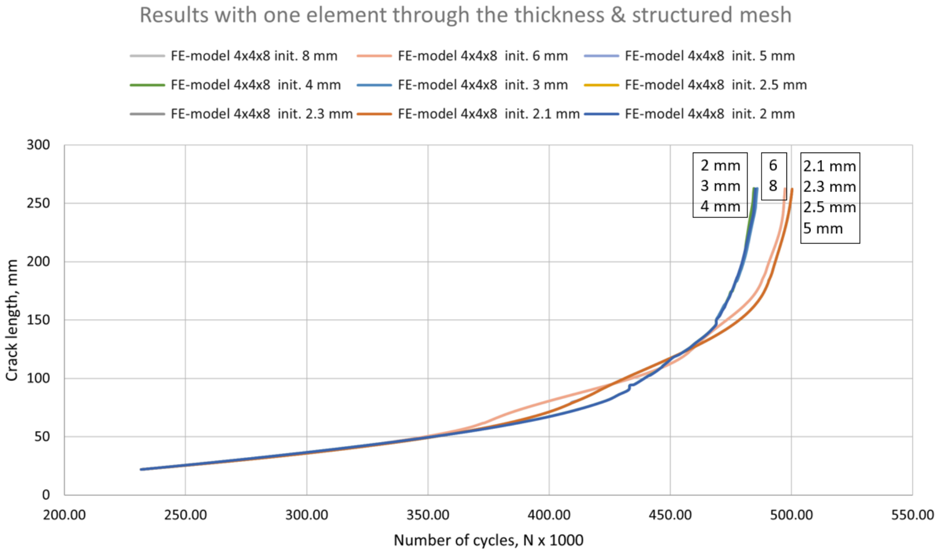

Figure 4.32: Number of cycle dependency on the crack length for different initial crack sizes with one elements through the thickness and parallel mesh topology.

To compare the results with two and one elements through the thickness, the variation of the number of cycles at certain crack lengths for different initial crack sizes has been plotted in figure 4.33. As the variation of the results is larger at every plotted crack length for two elements through the thickness than for one element, it has been concluded to recommend using one element through the thickness. The number of cycles varies by 1.0% for the crack length of 50 mm instead of 9.9% and by 2.8% for 200 mm crack length instead of 10.0%. It is important to note that this recommendation is only based on the reduction of the number of kinks along the crack path, however, it still remains unclear why these kinks appear and what is the best way to avoid them. The suggested recommendation to use one element through the thickness that improves the results of this model has been further used in this thesis.

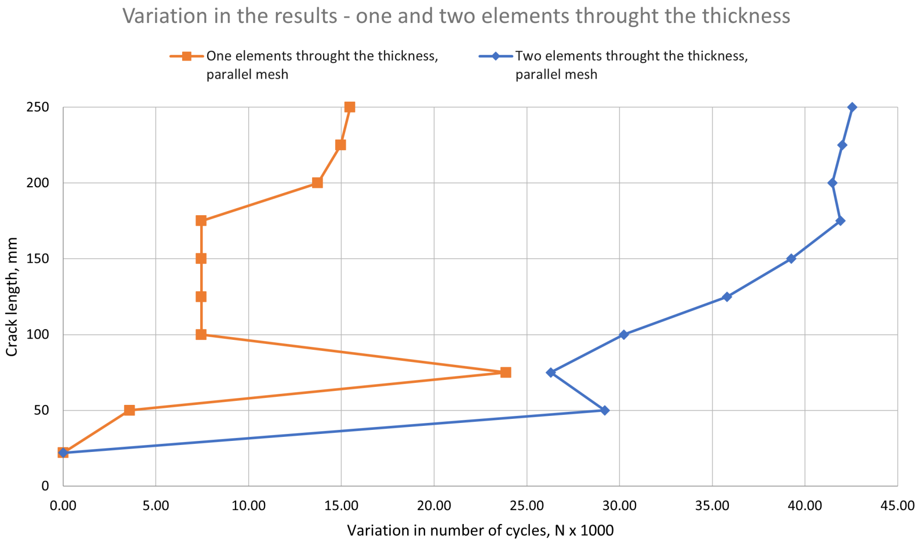

Figure 4.33: Variation of initial crack sensitivity analysis results with structured mesh topology for one or two elements through the thickness.

Parallel and unstructured mesh

The second attempt to reduce the variation of the initial crack size sensitivity analysis results has been realised by changing the in-plane mesh topology from parallel to an unstructured mesh. Both mesh topologies are presented in figure 4.34 and 4.35. The change to unstructured mesh has been applied to see if the variation of the results has been caused by the crack path's alignment with the structured mesh.

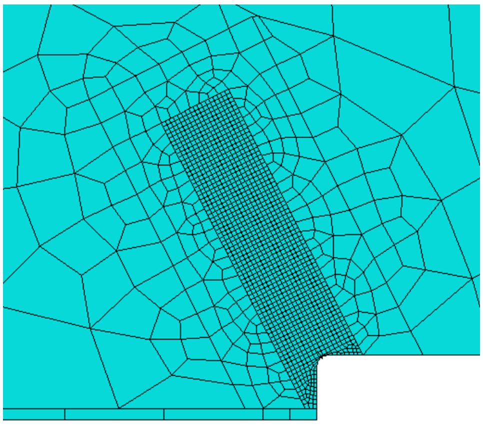

Figure 4.34: Parallel structured mesh topology.

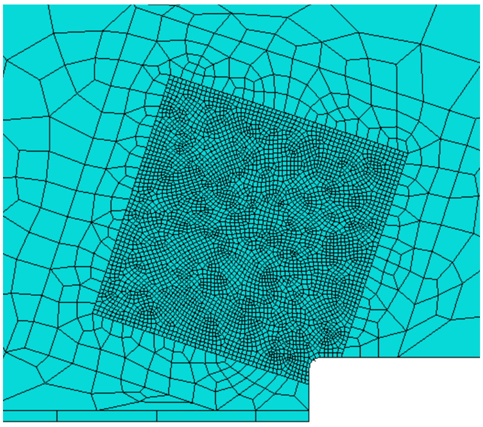

Figure 4.35: Unstructured mesh topology.

For the models run in the previous sections, the in-plane mesh topology of the parallel mesh contained a structured finely meshed zone. Based on the rectangular geometry of this zone, it has not been possible to assign the unstructured mesh topology. Therefore, this zone has been rotated at an angle of 45 degrees as shown in figure 4.35 and has been extended to ensure that the newly made zone covers the finely meshed area from the previous models. An unstructured mesh with a size of 4x4 mm has been assigned and the initial crack size sensitivity analysis has been performed. Results can be seen in figure 4.36.

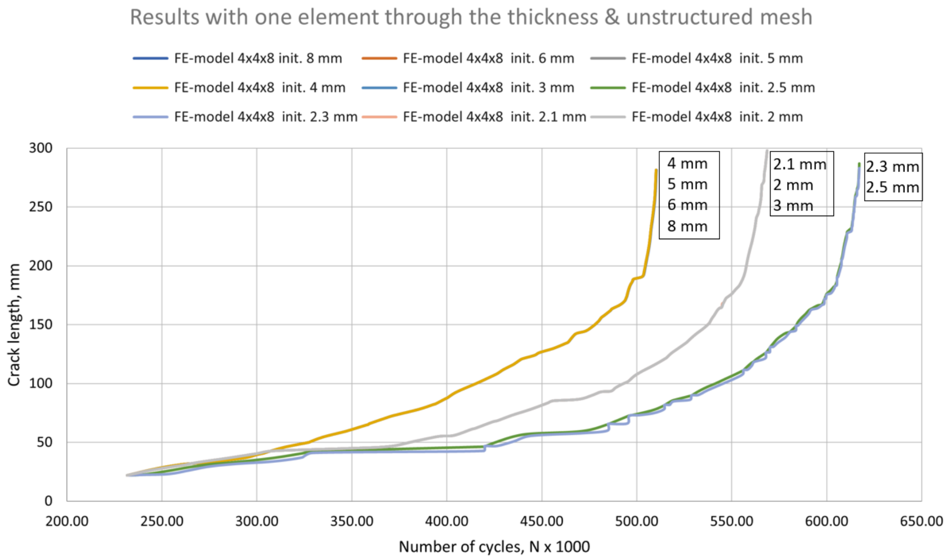

Figure 4.36: Number of cycle dependency on the crack length for different initial crack sizes with one elements through the thickness and unstructured mesh topology.

Same as with the parallel mesh topology, the results for the unstructured mesh topology are scattered and now lead to three bundles of results. However, unstructured mesh results have larger variation in the number of cycles than for the parallel mesh topology. It can be seen from figure 4.37, where the variation for the unstructured mesh is larger for at least 90000 number of cycles for any of the crack lengths larger than 45 mm. To give a comparison in percentage, the number of cycles obtained with parallel mesh topology varies by 1.0% and 2.8% for 50 mm and 200 mm long cracks, respectively, which in the case of unstructured mesh becomes 33.0% for the crack length of 50 mm and 20.5% for 200 mm crack.

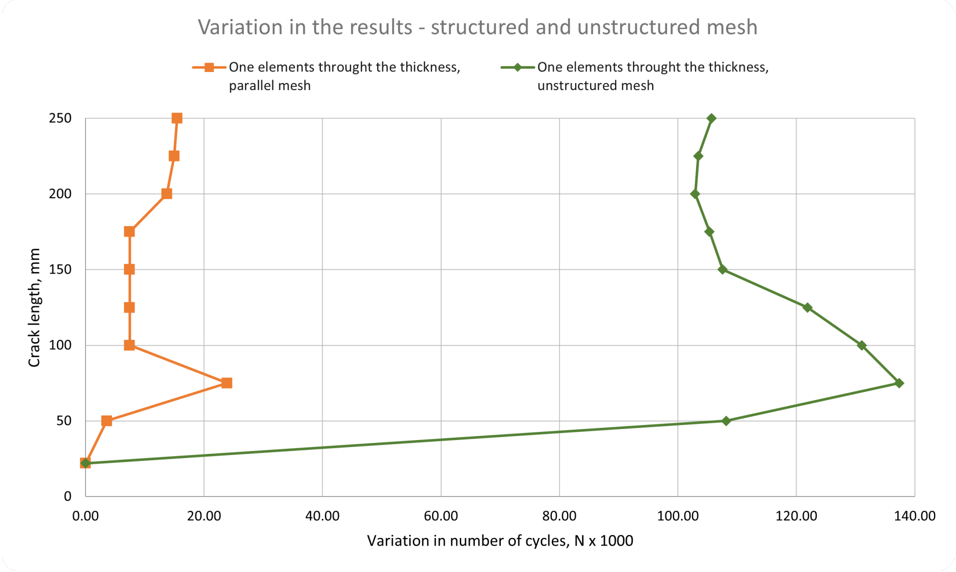

Figure 4.37: Variation of initial crack sensitivity analysis results with one element through the thickness for parallel and unstructured mesh topology.

To conclude this section, it is recommended to use the parallel mesh topology instead of unstructured mesh as it results in smaller deviation in the initial crack size sensitivity analysis results.

4.4.3. Conclusions from mesh parameters

From the mesh sensitivity analysis in section 4.4.1 and initial crack size sensitivity analysis in section 4.4.2 it has been concluded that the element size through the thickness and the in-plane mesh topology are one of the dominant parameters for the crack propagation. Based on the results from the analysis, it is recommended to use a parallel mesh topology instead of unstructured and to use one element through the thickness.

4.5. Crack propagation model comparison with the laboratory test results

In section 3.3.1 the crack initiation model has been compared with the laboratory test results to validate the FE-model. For the crack propagation, however, the results from the FE-model have not been validated with laboratory tests. Instead FE-model has been compared with the laboratory test results to calibrate the C coefficient from the Paris law. Two calibrations have been performed, one by keeping the coefficient m equal to the assumed 2.88 value, the second by changing it to a value of 3.00.

First, the choice of the most reliable model to use for the comparison has to be made. The model with the 4x4 in-plane mesh size has been chosen based on the mesh sensitivity analysis and the decaying trend of the results until the mesh size of 4 mm in section 4.4.1. Initial crack size sensitivity analysis in section 4.4.2 showed that it is recommended to use one element through the thickness and parallel mesh topology. When choosing the initial crack size, an initial crack size of 2.1 mm has been randomly chosen from figure 4.32. Results from the chosen FE-model can be seen in figure 4.38 as the most right-placed curve.

The choice of the laboratory test has been already made when the postprocessing of Abaqus results has been established through the AutoCAD and Excel in section 4.2, as it was needed to account for the number of cycles for the crack initiation. The beam with 10 mm radius has been chosen as in section 4.2 it has been explained that a smaller radius of the cope leads to higher stress concentrations and is therefore more prone to crack initiation. Instead of a cope that has been flame cut and grounded smooth or the one that has been drilled, the result from figure 4.2 form cope CB-10C with a flame cut cope hole has been chosen as it has been the most common cutting technique of these three. Results from the chosen laboratory test can be seen in figure 4.38 as the most left-placed curve.

After the FE-model and the laboratory test for comparison have been chosen, the C coefficient has been calibrated by using the Paris law (equation 2.2).

First, the postprocessed data (from AutoCAD and Excel) of the incremental crack length and number of cycles has been used to compute the crack growth rate da/dN. By dividing the crack growth rate with the assumed C value of $3.89 * 10^{-13}$, the stress intensity factor with the power of the assumed coefficient m has been obtained. This equality can be seen in equation 4.13 where coefficient m has been kept equal to the assumed value of 2.88.

$$\frac{da}{dNC_{assumed}} = (\Delta K)^{m_{assumed}} \tag{4.13}$$

Multiplying the result with the calibrated C coefficient, a new crack growth rate has been obtained, see equation 4.14. By using the same change of the crack length da, new changes in the number of cycles and therefore new crack growth curves have been obtained.

$$(\Delta K)^{m_{assumed}} * C_{calibrated} = \left(\frac{da}{dN}\right)_{new} \tag{4.14}$$

Calibration of the coefficient C has been performed by gradually increasing the assumed value of $3.89*10^{-13}$. Results for the intermediate coefficient C values of $4.25*10^{-13}$, $4.5*10^{-13}$ and $4.75*10^{-13}$ have been plotted in figure 4.38. The best alignment of the calibrated model with the laboratory test results when keeping the coefficient m to the assumed value of 2.88 has been observed at the value of $C_{calibrated} = 5.10 * 10^{-13}$.

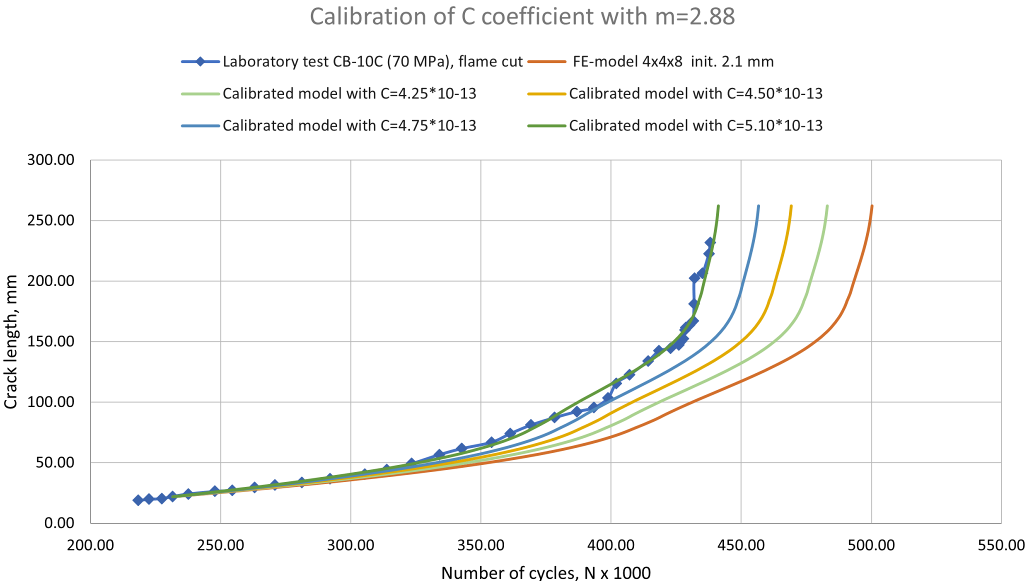

Figure 4.38: Crack length dependency from the number of cycles for the laboratory test of flame cut coped beam CB-10C, most reliable FE-model and for the calibrated models with m=2.88.

Second calibration has been performed by changing the coefficient m from the assumed value 2.88 to the new value of 3.00. This change has been performed to compare the calibrated value of the coefficient C with the values in the literature. The procedure of calibration is similar to the one described above. Except the equation 4.13 needs to be further elaborated as shown in equation 4.15 to change the assumed value of coefficient m to the new value of 3.00 as shown in equation 4.16.

$$\left(\frac{da}{dNC_{assumed}}\right)^{1/m_{assumed}} = \Delta K \tag{4.15}$$

$$\frac{da}{dNC_{assumed}} = (\Delta K)^{m_{new}} \tag{4.16}$$

After these additional changes, the calibration procedure continues similarly as described in equation 4.14, but now with the new value of the m coefficient, see equation 4.17

$$(\Delta K)^{m_{new}} * C_{calibrated} = \left(\frac{da}{dN}\right)_{new} \tag{4.17}$$

From figure 4.39 it can be seen that the change of the coefficient m from 2.88 to 3.00 has shifted the result curve to the far left side of the graph. Furthermore, a gradual decrease in the C coefficient has been performed, and results for the intermediate coefficient C values of $2.7 * 10^{-13}$ and $2.0 * 10^{-13}$ have been plotted, leading to a result curve that matches the laboratory test result the best with the value of $C_{calibrated} = 1.62 * 10^{-13}$.

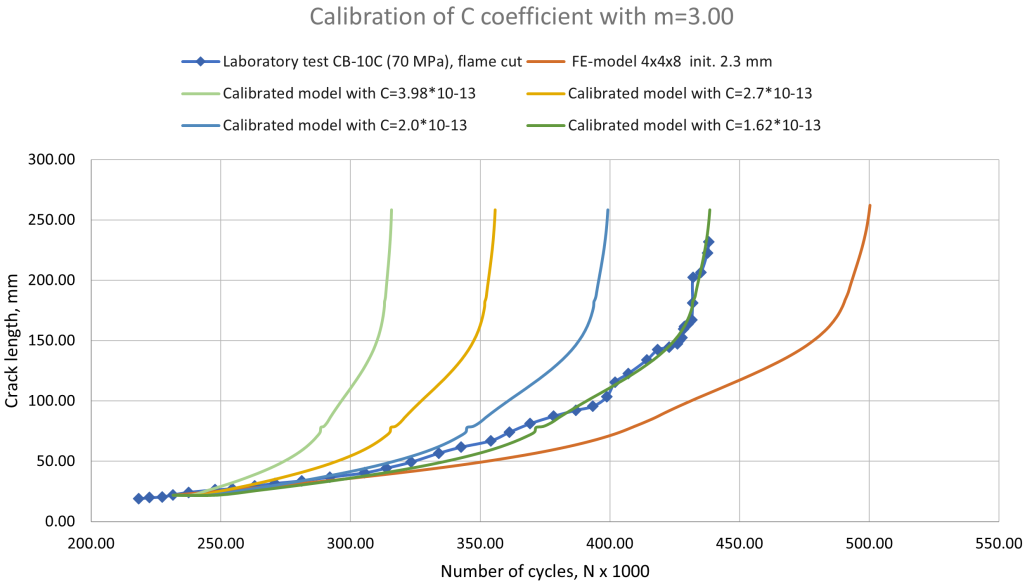

Figure 4.39: Crack length dependency from the number of cycles for the laboratory test of flame cut coped beam CB-10C, most reliable FE-model and for the calibrated models with m=3.00.

5

Conclusions

When determining fatigue crack inspection intervals, crack propagation analysis is of great importance. The reliability of the inspection intervals will depend on the variability of crack propagation. In this research, the variability of crack propagation analysis using XFEM with respect to mesh parameters and methods to determine stress intensity factors has been investigated.

Crack propagation analysis has been performed for the coped steel beam of 406 mm height with 8 mm thickness of the web and 10 mm radius of the cope by using the computer software Abaqus with regular XFEM, VCCT and J-integral methods. Location of the crack initiation has been determined by looking at the stress levels at the rounding of the cope and comparing them to the laboratory test results. In-plane mesh size has been varied between 3 to 8mm, two mesh orientations have been examined, being a mesh parallel to the crack propagation direction and an unstructured mesh, and the initial crack length has been varied between 2 to 8 mm. Crack growth has been based on Paris law using the recommended C and m coefficients of 3.98E-13 and 2.88 from the British Standard 7910.

Based on the performed propagation analysis, the following conclusions can be drawn:

- SIF's for stationary cracks found when using XFEM were compared to the SIF's found when using the VCCT and J-integral method. Results varied by 3.4% for a crack length of 50 mm and by 8.5% for a crack length of 200 mm when using a parallel mesh size of 5 mm. At least five fine size mesh elements need to be surrounding the crack tip to get reliable results. Using fewer elements increased the difference for the 200 mm crack to 52.3%.
- Mesh sensitivity analysis shows that, when keeping the number of elements through the thickness constant, decreasing the mesh size leads to a decrease in the number of cycles, as expected. The decreasing trend changes when a different number of elements through thickness is used.
- Initial crack size sensitivity analysis (using a parallel mesh of 4x4 mm) shows less kinks in the crack path and therefore a smaller variation in the number of cycles between different initial cracks when using one element through thickness than when using two elements through thickness. When using two elements through the thickness, the number of cycles corresponding to a crack length of 50 or 200 mm varies by 10% between a 4 and 8 mm initial crack. When using only one element, this percentage reduces to 1.0% between 5 and 8 mm and 2.8% between 2.5 and 4 mm, respectively.
- The parallel mesh topology gives less variability in the number of cycles than the unstructured mesh topology when varying the initial crack size. When using one element through thickness, the number of cycles with parallel mesh varies by 1.0% between 5 and 8 mm initial crack results and 2.8% between 2.5 and 4 mm initial crack results for 50 mm and 200 mm cracks, respectively, which in the case of unstructured mesh becomes 33.0% between 2.3 and 8 mm for the crack length of 50 mm and 20.5% between 2.3 and 6 mm for 200 mm crack.

Gathering the results together, the number of cycles can have a variation ranging from 5.4% to 46.3% for the crack length of 50 mm and from 14.2% to 39.0% for the crack length of 200 mm. Based on this research, when modelling crack growth in coped beams, the following is recommended:

- Keep at least five finely meshed elements around the crack tip
- Use parallel mesh topology
- And use one element through the thickness to reduce kinks in the crack path

A certain crack growth curve has been chosen by following the recommendations of using a parallel mesh topology and one element through the thickness, by choosing in-plane mesh size of 4x4 mm, based on the smallest element size with the decreasing trend of the mesh sensitivity analysis, and by randomly choosing the initial crack size of 2.1 mm. Based on this curve, two calibrations of the Paris law parameter C have been performed. While keeping the m-factor constant at the value of $m = 2.88$, a value of $C = 5.10^{-13}$ showed the best fit to the experimental data. When changing m-factor to a value of $m = 3.00$, a value of $C = 1.62^{-13}$ showed the best fit. Choice of different initial crack sizes, however, might have led to different C coefficients.

Suggested recommendations are the conclusions from this thesis that indicates steps to reduce variation of the results obtained by the computer software Abaqus. However, they do not guarantee the attainment of a reliable model. Results still show variation that has not been explained, therefore, further research is required for the achievement of a reliable model.

6

Discussion and Recommendations

During this thesis, the main research question that had to be answered was: *How to accurately model fatigue crack propagation for railway bridges with coped beam connections?*

When creating a FE-model, the validation needs to be performed. In this thesis this has been done with laboratory tests, however, there are very few tests performed on coped beams. This limitation led to validation of the model with laboratory tests with no data about the crack path. Thus, a method that does not need a predefined crack path needs to be used and thus XFEM method has been used.

From one side, many positive aspects of the XFEM method have been observed during this thesis. The XFEM method is capable of generating the crack path without any preknowledge about it. Furthermore, SIF evaluation for stationary cracks by comparing XFEM method results with well-known J-integral and VCCT method showed matching results, therefore, verifying how the XFEM method calculates the most important parameter for the crack propagation, SIF. In addition, the crack length dependency on the number of load cycles curve had a similar shape to the laboratory test results.

From the other side, the study of the dominant parameters for crack propagation, performed to answer sub-question 2, indicated a variation in the results of the number of cycles presented in chapter 5. Further research needs to be performed to try to reduce this variation in this crack propagation model. Suggestions for further actions are:

- As the variation of the results has been low for the first 45 mm of the crack length, the suggestion is to investigate the model around the crack length of 45 mm where the deviation has begun. Stationary crack analysis should be performed right before and right after the crack length of 45 mm to see if the SIFs are changing and causing the variation in results. Suggestion is to partition the crack path until the last increment of the crack and assign the XFEM crack only for this last increment.
- Speed of the further analysis can be greatly improved by optimizing the postprocessing procedure through AutoCAD and Excel.
- It is suggested to perform sensitivity analysis with different cope radius and stress range to have more insight in the variation of the results, as the laboratory test used for validation in this thesis has data for coped beams with 20 and 30 mm cope radius and stress ranges of 40 and 50 MPa.

Another discussion point is the C coefficient from Paris law. After calibration of the C coefficient, the FE-model curve matched well with the laboratory test curve. However, it is odd that the calibrated value is larger than the value suggested in the British Standard 7910 as all standard has been created on the safe side by using certain safety factors. A literature study could be performed to investigate C coefficients that have been obtained in different research.

This thesis has contributed to the ultimate goal of obtaining inspection intervals for the coped beam connection by setting the first step towards it and creating a simply supported beam model with one location of loading. While working on this model, some thinking has been done for possible further steps to achieve the inspection intervals. Recommended further actions are:

- Analysis of different loading positions should be performed to account for the moving train load.
- Expansion from a simply supported beam model to a model with multiple spans should be analysed to account for the global behaviour of the bridge.

References

[1] Awais Ahmed. *Extended finite element method (xfem) - modeling arbitrary discontinuities and failure analysis*. Tech. rep. Pavia University, 2009, p. 196.

[2] T L Anderson. *Comparison of varied specimen geometry for simplified VECD test with pulse-rest period*. CRC press, 2017, p. 610. ISBN: 9781420058215. DOI: `10.1007/s42947-020-0181-2`.

[3] T. Belytschko and T. Black. “Elastic Crack Growth in Finite Elements”. In: *International Journal for Numerical Methods in Engineering* 620 (1999), pp. 601–620.

[4] M.L. Bemzeggagh and M. Kenane. “Measuremet of mixed-mode delamination fracture toughness of unidirectional glass/epoxy composites with mixed-mode bending apparatus”. In: *Composite Science and Technology* 56 (1996), pp. 439–449. ISSN: 00034266.

[5] Niels van den Berg. *Effects of residual stresses on fatigue crack propagation of an orthotropic steel bridge deck*. Tech. rep. Delft University ofTechnology, 2021, p. 198. DOI: `10.1016/j.matdes.2020.109294`.

[6] Johan Blaauwendraad. *Plates and FEM, Surprises and pitfall*. 1. 2014, pp. 1–5. ISBN: 9780874216561.

[7] Fatih Bozkurt and Eva Schmidová. “Fracture toughness evaluation of S355 steel using circumferentially notched round bars”. In: *Periodica Polytechnica Transportation Engineering* 47.2 (2019), pp. 91–95. ISSN: 15873811. DOI: `10.3311/PPtr.11560`.

[8] P. P. Camanho, C. G. Dávila, and M.F. de Moura. “Numerical Simulation of Mixed-mode Progressive Delamination in Composite Materials”. In: *Journal of Composite Materials* 37.May 2014 (2003), pp. 1415–1438. DOI: `10.1177/002199803034505`.

[9] Canadian Institute of Steel Construction. *CSA G40.21 Standard for Structural Steels Issued by Canadian Standards Association (CSA)*. 1991.

[10] Paulo Chambel, Rui F. Martins, and Luís Reis. “Fatigue crack growth under mode I, II and III for plane-strain and plane-stress conditions”. In: *Procedia Engineering* 74 (2014), pp. 232–235. ISSN: 18777058. DOI: `10.1016/j.proeng.2014.06.254`. URL: `http://dx.doi.org/10.1016/j.proeng.2014.06.254`.

[11] G. P. Cherepanov. “Crack propagation in continuous media. PMM vol. 31, no. 3, 1967, pp. 476-488”. In: *Journal of Applied Mathematics and Mechanics* 31.3 (1967), pp. 503–512. ISSN: 00218928. DOI: `10.1016/0021-8928(67)90034-2`.

[12] M. Creager and P. C. Paris. “Elastic field equation for blunt cracks with reference to stress corrosion cracking”. In: 3 (4) (1967), pp. 247–252.

[13] Danilo D’Angela and Marianna Ercolino. “Finite Element Analysis of Fatigue Response of Nickel Steel Compact Tension Samples using ABAQUS”. In: *Procedia Structural Integrity* 13 (2018), pp. 939–946. ISSN: 24523216. DOI: `10.1016/j.prostr.2018.12.176`. URL: `https://doi.org/10.1016/j.prostr.2018.12.176`.

[14] Dassault Systèmes Simulia. “Abaqus 6.11 Analysis User’s Manual”. In: *Dassault Systémes Inc. Providence, RI, USA* I ().

[15] Dassault Systèmes Simulia. “Abaqus 6.11 Analysis User’s Manual”. In: *Dassault Systémes Inc. Providence, RI, USA* II (). ISSN: 15346080. URL: `http://www.ncbi.nlm.nih.gov/pubmed/21836536`.

[16] Dassault Systèmes Simulia. “Abaqus/CAE 6.13 User’s Guide”. In: *Dassault Systémes Inc. Providence, RI, USA* (), p. 1138.

[17] T. Denyse De Araújo et al. “Numerical estimation of fracture parameters in elastic and elastic-plastic analysis”. In: *European Congress on Computational Methods in Applied Sciences and Engineering, ECCOMAS 2000* September (2000).

[18] Cornelia E Demers, John W Fisher, and University Lehigh. “A survey of localized cracking in steel bridges: 1981 to 1988”. In: *ATLSS report ;89-01* 2.iii, 324 p. (1989), iii, 324 p. URL: `http://catalog.hathitrust.org/Record/009215130%5Cnhttp://hdl.handle.net/2027/coo.31924052947169`.

[19] Véronique Doquet et al. “Fatigue crack initiation and propagation”. In: *Mechanics - Microstructure - Corrosion Coupling: Concepts, Experiments, Modeling and Cases* (2019), pp. 65–90. DOI: `10.1016/B978-1-78548-309-7.50004-1`.

[20] Norman E. Dowling. *Mechanical Behavior of Materials - Engineering Methods for Deformation, Fracture and Fatigue*. Vol. 4. 2013, p. 954. ISBN: 9780131395060.

[21] Zhen-zhong Du. “Extended Finite Element Method (XFEM) in Abaqus.” In: *Dassault Systemes.* (2016), pp. 1–61. URL: `https://www.slideshare.net/nguyenbinh80/advanced-xfemanalysis?qid=2b0d4db3-76fc-4315-a253-bb9d10b6626f&v=&b=&from_search=7`.

[22] M. H. El Haddad, T. H. Topper, and T. N. Topper. “Fatigue life predictions of smooth and notched specimens based on fracture mechanics”. In: *Journal of Engineering Materials and Technology, Transactions of the ASME* 103.2 (1981), pp. 91–96. ISSN: 15288889. DOI: `10.1115/1.3224996`.

[23] D. Frómeta et al. “Identification of fracture toughness parameters to understand the fracture resistance of advanced high strength sheet steels”. In: *Engineering Fracture Mechanics* 229.December 2019 (2020), p. 106949. ISSN: 00137944. DOI: `10.1016/j.engfracmech.2020.106949`. URL: `https://doi.org/10.1016/j.engfracmech.2020.106949`.

[24] Emmanuel E. Gdoutos. “Critical Stress Intensity Factor Fracture Criterion”. In: *Solid Mechanics and its Applications* 263 (2020), pp. 131–165. ISSN: 22147764. DOI: `10.1007/978-3-030-35098-7{\_}5`.

[25] A.A. Griffith. “The Phenomena of Rupture and Flow in Solids”. In: *Philosophical Transactions* 221 (1920), pp. 163–198.

[26] Ravi Shankar Gupta. “Prediction of Fatigue Crack Propagation in Orthotropic Steel Decks using XFEM based on LEFM and VCCT”. In: (2019), p. 111.

[27] Theresa Anne Holden. “Fatigue Rehabilitation of Coped Steel Beams Using Carbon Fibre Reinforced Polymers”. In: 20.1 (2012), pp. 59–61. ISSN: 0709-5201. DOI: `10.3138/flor.20.015`.

[28] H. Homma and H. Nakazawa. “Effect of mechanical properties of material on rate of fatigue crack propagation”. In: *Engineering Fracture Mechanics* 10.3 (1978), pp. 539–552.

[29] C.E. Inglis. “Stresses in a Plate Due to the Presence of Cracks and Sharp Corners”. In: *Transactions of the Institute of Naval Architects* 55 (1913), pp. 219–241.

[30] G. R. Irwin. *Fracture. Handbuch der physik elastizitaet und plastizitaet.* 1958.

[31] G.R Irwin. “Onset of Fast Crack Propagation in High Strength Steel and Aluminum Alloys”. In: *Sagamore Research Conference Proceedings* 2 (1956), pp. 289–305.

[32] Nikita Kaminskyy. “Fatigue Crack Propagation in Friction Stir Welded Aluminium Alloy 5083 Experimental and Numerical Analysis”. In: January (2021).

[33] Ronald Krueger. “Virtual crack closure technique: History, approach, and applications”. In: *Applied Mechanics Reviews* 57.1-6 (2004), pp. 109–143. ISSN: 00036900. DOI: `10.1115/1.1595677`.

[34] Michael Levén and Daniel Rickert. “Stationary 3d crack analysis with abaqus xfem for integrity assessment of subsea equipment”. In: *ChalmersUniversity ofTechnology* (2012).

[35] AY Lindberg and AE Schultz. “Incorporation of fatigue detail classification of steel bridges into the Minnesota Department of Transportation database (Report No. MN/RC-2007-22)”. In: (2007), pp. 1–191. URL: `http://trid.trb.org/view.aspx?id=868584`.

[36] Lucie Malíková and Václav Veselý. “Williams Expansion Terms and their Importance for Accurate Stress Field Description in Specimens with a Crack”. In: *Transactions of the VŠB - Technical University of Ostrava, Mechanical Series* 59.2 (2013), pp. 109–114. ISSN: 12100471. DOI: `10.22223/tr.2013-2/1963`.

[37] Johan Maljaars. *TNO rapport: Interval vermoeiingsinspecties notches spoorbruggen. Phase 1: literature review, evaluation of current approach and proposal for follow-up*. 2014.

[38] David Malschaert. *Fracture Mechanics: Application on Orthotropic Steel Decks*. Tech. rep. Delft: Delft University ofTechnology, 2020, p. 149. DOI: `10.1115/1.3143689`. URL: `http://resolver.tudelft.nl/uuid:9cef6563-5e27-41a7-9b72-69c9036dd3d2`.

[39] E. Martínez-Pañeda, S. Natarajan, and S. Bordas. "Gradient plasticity crack tip characterization by means of the extended finite element method". In: *Computational Mechanics* 59.5 (2017), pp. 831–842. ISSN: 01787675. DOI: `10.1007/s00466-017-1375-6`.

[40] Yu G. Matvienko. "Maximum average tangential stress criterion for prediction of the crack path". In: *International Journal of Fracture* 176.1 (2012), pp. 113–118. ISSN: 03769429. DOI: `10.1007/s10704-012-9715-1`.

[41] K. Meinhard. *Finite Elements in Fracture Mechanics*. 10th ed. 2013. ISBN: 9789400766792.

[42] J. M. Melenk and I. Babuška. "The Partition of Unity Finite Element Method: Basic Theory and Applications". In: *Computer Methods in Applied Mechanics and Engineering* 139.1-4 (1996), pp. 289–314.

[43] N. Moës, J. Dolbow, and T. Belytschko. "A finite element method for crack growth without remeshing". In: *International Journal for Numerical Methods in Engineering* 46 (1999), pp. 131–150. ISSN: 15551792.

[44] Alireza Mohammadi and Walid S. Najjar. "Analytical Study of Fatigue Cracking in Coped Stringers of Steel Bridges". In: *Transportation Research Record* 2673.10 (2019), pp. 239–246. ISSN: 21694052. DOI: `10.1177/0361198119849065`.

[45] Nederlands Normalisatie-instituut. "NEN-EN 1993-1-1: Design of steel structures - Part 1 - General rules and rules for buildings". In: (2006).

[46] Alain Nussbaumer, Luis Borges, and Laurence Davaine. "Fatigue design of steel and composite structures. and concrete structures. ECCS, 2011." In: (2018).

[47] W. D. Pilkey. *Peterson's stress concentration factors Second edition*. John Wiley & Sons, Ltd, 1997, p. 57. ISBN: 0471538493.

[48] James R. Reeder. "An Evaluation of Mixed-Mode Delamination Failure Criteria". In: *NASA Technical Memorandum 104210* February (1992), pp. 1–57.

[49] K. Rege and H. G. Lemu. "A review of fatigue crack propagation modelling techniques using FEM and XFEM". In: *IOP Conference Series: Materials Science and Engineering* 276.1 (2017). ISSN: 1757899X. DOI: `10.1088/1757-899X/276/1/012027`.

[50] J. R. Rice. "A path independent integral and the approximate analysis of strain concentration by notches and cracks". In: *Journal of Applied Mechanics, Transactions ASME* 35.2 (1964), pp. 379–388. ISSN: 15289036. DOI: `10.1115/1.3601206`.

[51] C. W. Roeder et al. *Fatigue cracking of riveted, coped, stringer-to-floorbeam connections*. 2001.

[52] J. J. Roger Cheng. "Design of steel beams with end copes". In: *Journal of Constructional Steel Research* 25.1-2 (1993), pp. 3–22. ISSN: 0143974X. DOI: `10.1016/0143-974X(93)90049-X`.

[53] Jaap Schijve. *Fatigue and Scatter*. 2008, pp. 373–394. ISBN: 9781402068072. DOI: `10.1007/978-1-4020-6808-9{\_}12`.

[54] Walter Schütz. "A history of fatigue". In: *Engineering Fracture Mechanics* 54.2 (1996), pp. 263–300. ISSN: 00137944. DOI: `10.1016/0013-7944(95)00178-6`.

[55] Antonio Almeida Silva, Marco Antonio dos Santos, and Gabriel de Castro Coêlho. "The use of xfem for stress intensity factor estimation of surface cracks". In: (2017). DOI: `10.26678/abcm.cobem2017.cob17-0534`.

[56] Dassault Systèmes Simulia. "Abaqus 6.11 Theory Manual". In: *Dassault Systémes Inc. Providence, RI, USA* Dassault Systemes Simulia Corp., Providence, RI, USA. ().

[57] British Standards. "BS 7910: Guide to methods for assessing the acceptability of flaws in metallic structures". In: *BSI Standards Publication* 3.1 (2013), p. 306.

[58] E. Z. Stowell. "Stress and Strain Concentration At a Circular Hole in and Infinite Plate". In: *National Advisory Committee For Aeronautics* (1950).

[59] S. Suresh. *Fatigue of Materials, Second Edition*. Press Syndicate of the University of Cambridge, 1998, p. 669.

[60] John Taylor. “An Engineer’s Guide to Fabricating Steel Structures, Successful Welding of Steel Structures”. In: 2 (2003).

[61] Website. *Amplitude Curves*. 2017. URL: `https://abaqus-docs.mit.edu/2017/English/SIMACAEPRCRefMap/simaprc-c-amplitude.htm` (visited on 02/06/2022).

[62] Website. *Contour integral evaluation*. 2017. URL: `https://abaqus-docs.mit.edu/2017/English/SIMACAEANLRefMap/simaanl-c-contintegral.htm` (visited on 01/21/2022).

[63] Website. *Encyclopedia Britannica*. 2022. URL: `https://www.britannica.com/science/metal-fatigue` (visited on 01/05/2022).

[64] Website. *Total Materia*. 2010. URL: `https://www.totalmateria.com/page.aspx?ID=CheckArticle&site=kts&NM=295` (visited on 01/08/2022).

[65] Michael C H Yam, J J Roger Cheng, and Associate Member. *Fatigue Strength of Coped Steel Beams*. Tech. rep. 1990.

[66] Michael C H Yam et al. “Local failures of coped steel beams-A state-of-the-art review”. In: (2014). DOI: `10.1016/j.jcsr.2014.07.002`. URL: `http://dx.doi.org/10.1016/j.jcsr.2014.07.002`.

[67] Michael C. H. Yam and J. J. Roger Cheng. *Fatigue Strength of Coped Steel Beams*. Tech. rep. Univeristy of Alberta, 1988, p. 101. DOI: `10.1061/(asce)0733-9445(1990)116:9(2447)`.

A

Figures from lab report [67]

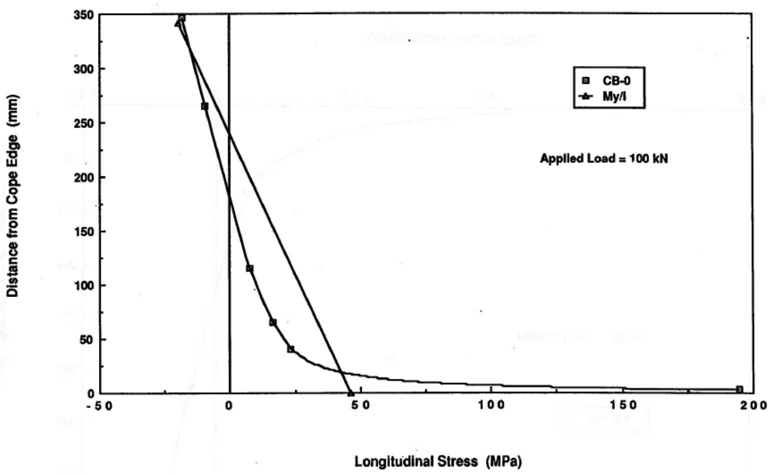

Figure A.1: Stress distribution in the web of the beam above the cope under 100 kN loading for the specimen CB-0 [67].

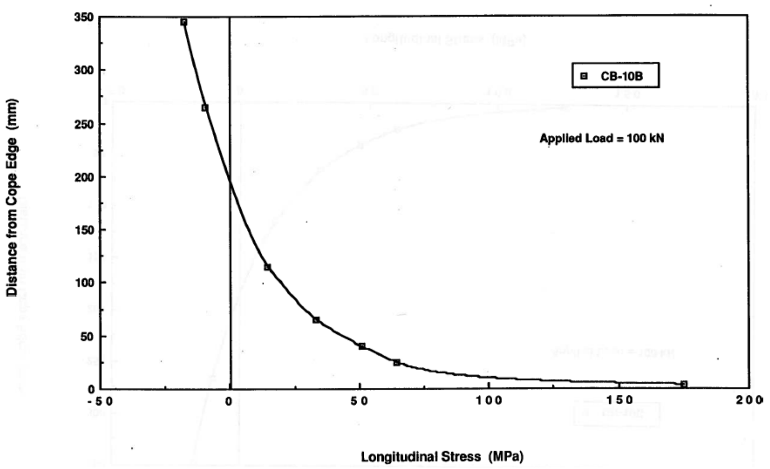

Figure A.2: Stress distribution in the web of the beam above the cope under 100 kN loading for the specimen CB-10B [67].

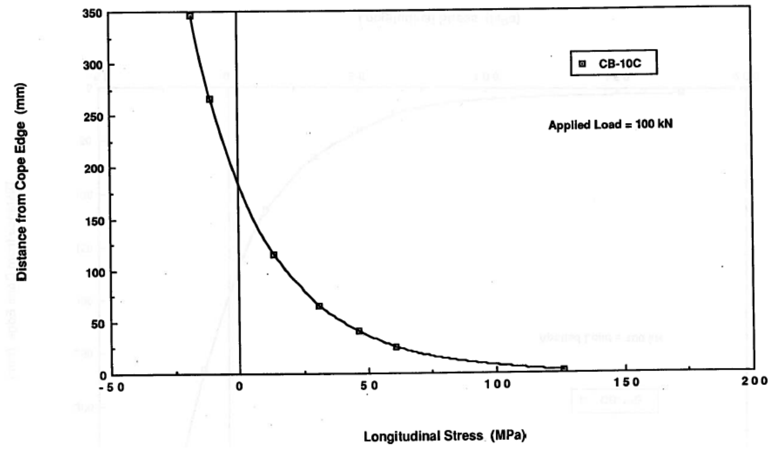

Figure A.3: Stress distribution in the web of the beam above the cope under 100 kN loading for the specimen CB-10C [67].

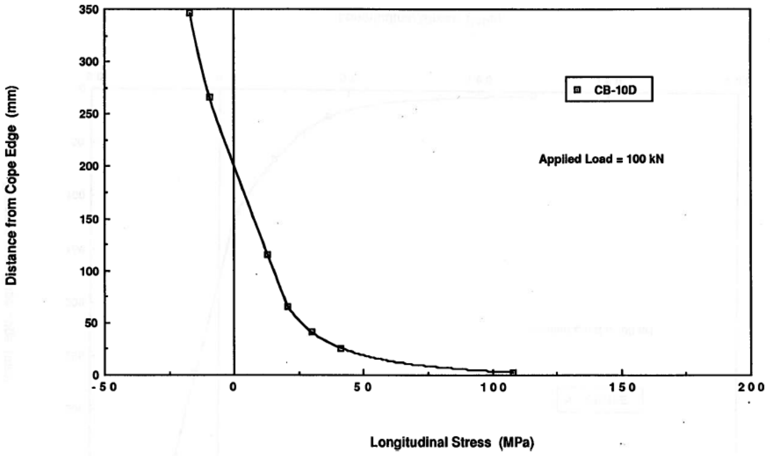

Figure A.4: Stress distribution in the web of the beam above the cope under 100 kN loading for the specimen CB-10D [67].

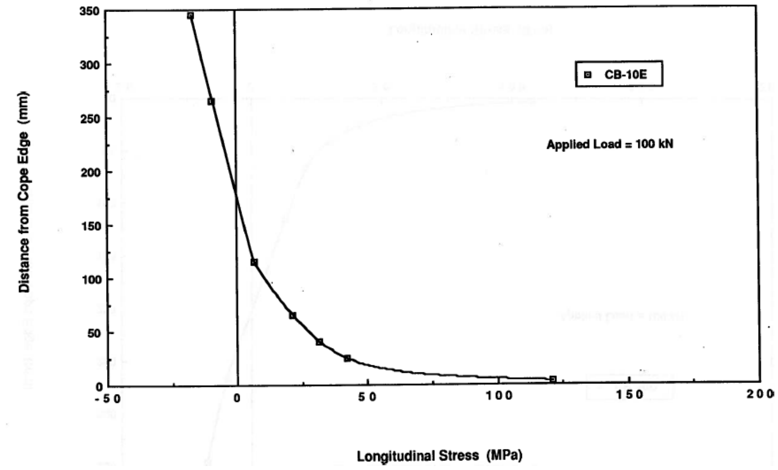

Figure A.5: Stress distribution in the web of the beam above the cope under 100 kN loading for the specimen CB-10E [67].

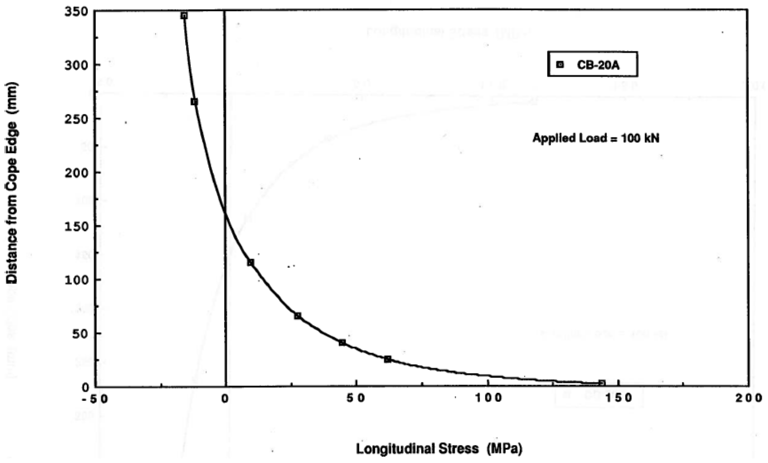

Figure A.6: Stress distribution in the web of the beam above the cope under 100 kN loading for the specimen CB-20A [67].

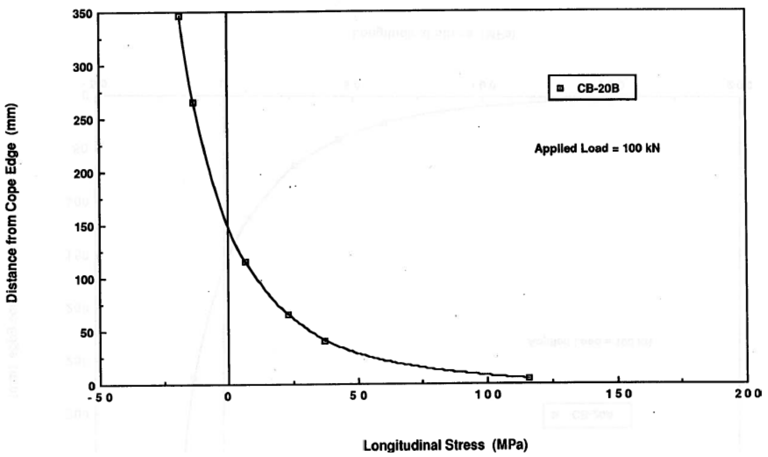

Figure A.7: Stress distribution in the web of the beam above the cope under 100 kN loading for the specimen CB-20B [67].

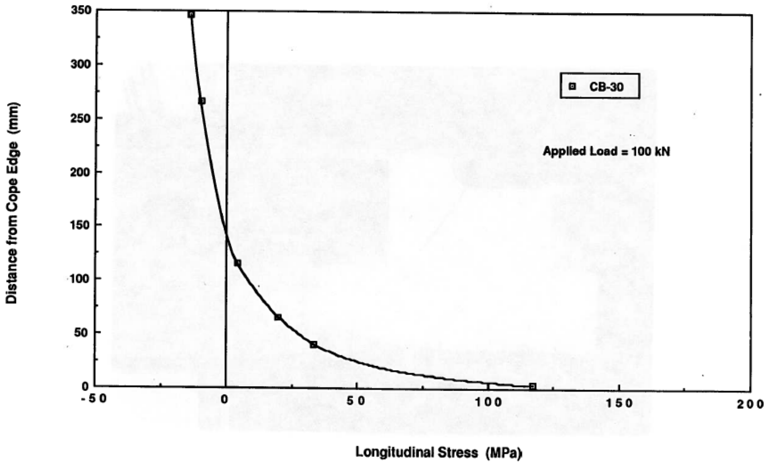

Figure A.8: Stress distribution in the web of the beam above the cope under 100 kN loading for the specimen CB-30 [67].

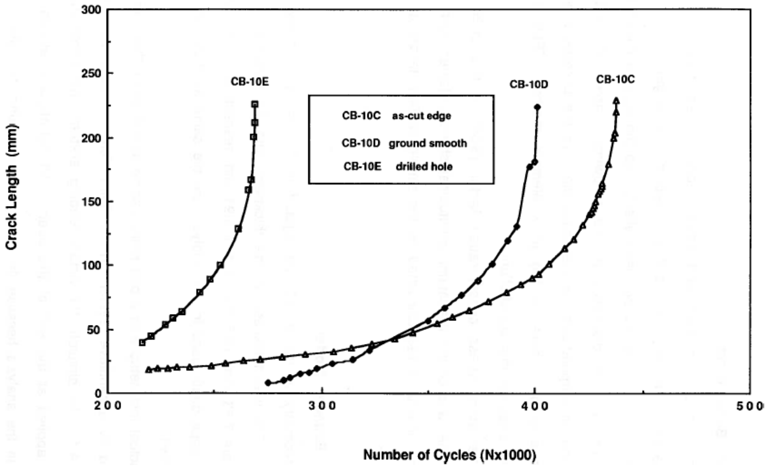

Figure A.9: Crack length dependency of the number of the load cycles for different cope cutting methods [67].

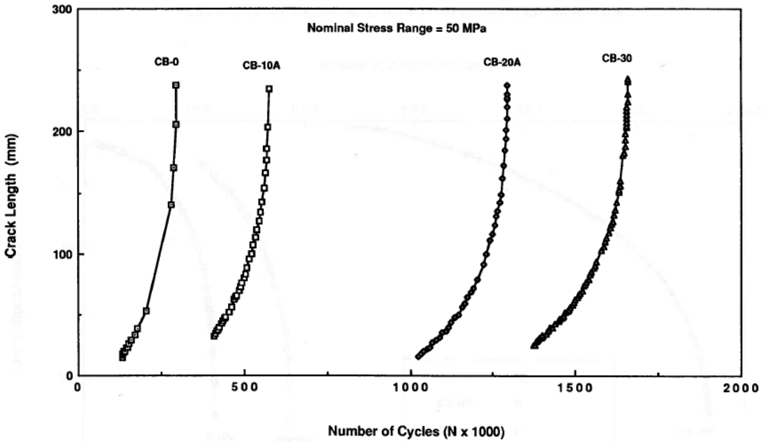

Figure A.10: Crack length dependency of the number of the load cycles for different cope radius of the cope [67].

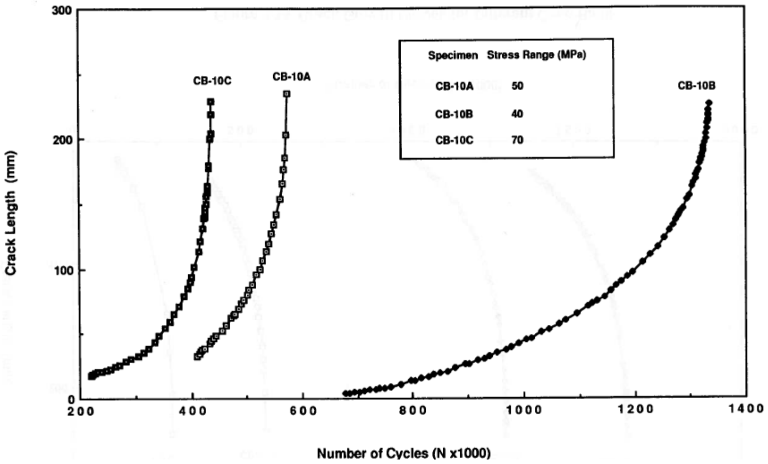

Figure A.11: Crack length dependency of the number of the load cycles for different stress ranges [67].